NASA Technical Memorandum 4055

A Two-Dimensional Numerical Simulation of a Supersonic, Chemically Reacting Mixing Layer
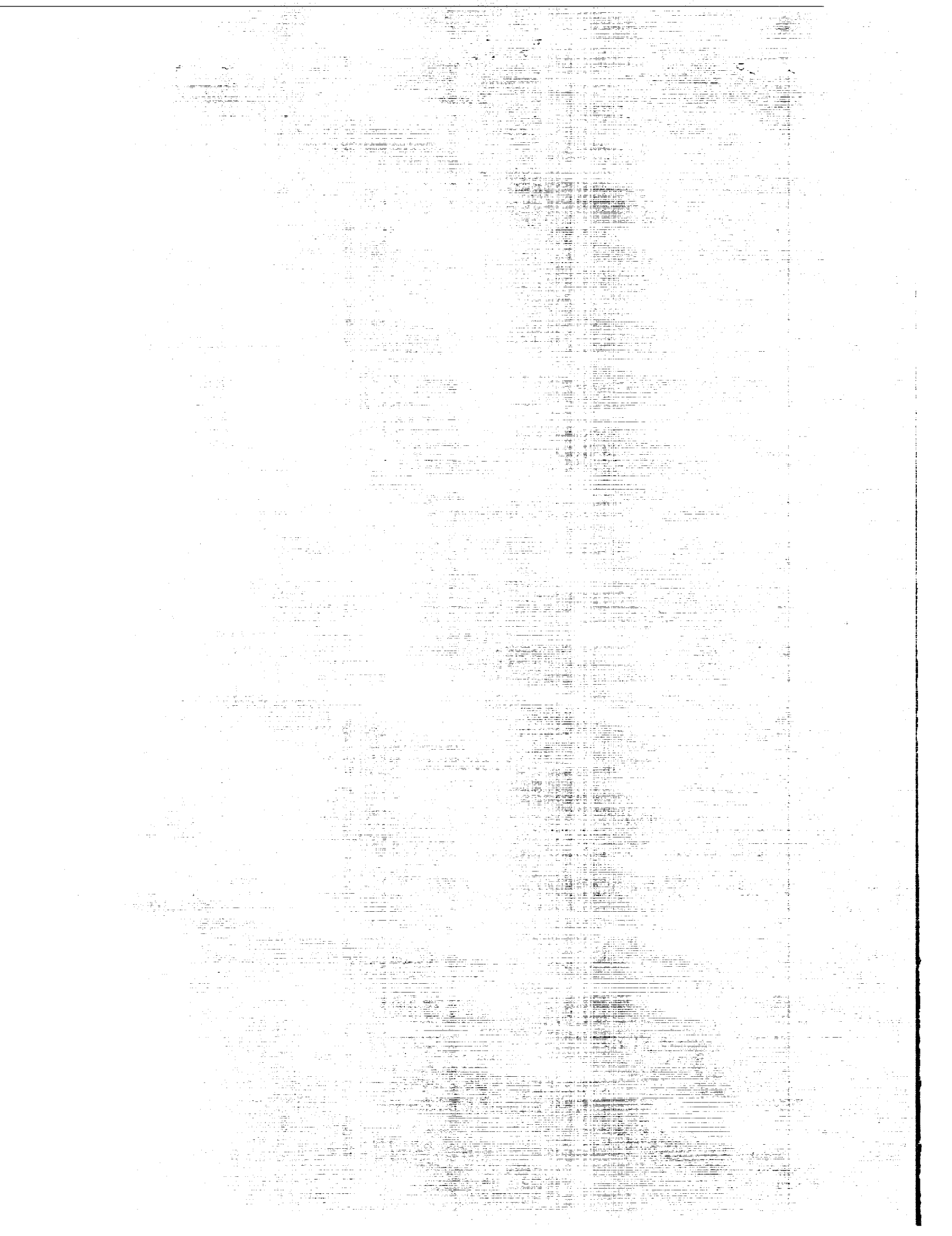
J. Philip Drummond

DECEMBER 1988

A Two-Dimensional Numerical Simulation of a Supersonic, Chemically Reacting Mixing Layer

J. Philip Drummond
Langley Research Center
Hampton, Virginia

Contents

Symbols

Symbols in parentheses are for computer-generated figures.

A	cross-sectional area, m^2
A_i	constant in Arrhenius law for reaction i
b_{ix}	body force of species i in x coordinate direction, N/kg
b_{iy}	body force of species i in y coordinate direction, N/kg
C_i	concentration of species i, kg-mole/m^3
c	speed of sound, m/s
c_p	specific heat at constant pressure, J/kg-K
D_{ij}	binary diffusion coefficient, m^2/s
D_T	thermal diffusion coefficient, m^2/s
E	activation energy, cal/g-mole; total internal energy, J/kg
$\mathbf{F}$	flux vector
$\widehat{F}_n, \widehat{F}_n^{(1)}$	expansion coefficients in Chebyshev series
f_i	mass fraction of species i
G_R	Gibbs energy of reaction, J/kg-mole
g_i	Gibbs energy of species i, J/kg-mole
$\mathbf{H}$	source vector
h_i	enthalpy of species i, J/kg
h_o	total enthalpy, J/kg
h_i^o	reference enthalpy at standard conditions, J/kg
$[I]$	identity matrix
J	Jacobian

K		equilibrium constant, source Jacobian
k		thermal conductivity, J/m-s-K
k_b		reverse reaction rate
k_f		forward reaction rate
$\mathbf{M}$		third body
M		molecular weight, kg/kg-mole; Mach number
N		number of nodes
N_i		constant in Arrhenius law for reaction i
N_R		number of reactions
N_s		number of species
n_i		moles of species i
p		static pressure, Pa
p_o		total pressure, Pa
q		heat flux, J/m^2-s
R		steady-state residual; gas constant, J/kg-K
R^o		universal gas constant, J/kg-mole-K
$R^{o\prime}$		universal gas constant, cm^3-atm/g-mole-K
T		static temperature, K
T_ϵ		effective temperature, K
T_n		Chebyshev polynomial
T_o		total temperature, K
t		time, s
Δt		time step, s
$\mathbf{U}$		dependent variable vector
u	(U)	streamwise velocity, m/s
$\widetilde{u}_i$		streamwise diffusion velocity of species i, m/s
$\widetilde{\mathbf{V}}_i$		diffusion velocity of species i, m/s
v		transverse velocity, m/s
$\widetilde{v}_i$		transverse diffusion velocity of species i, m/s
$\dot{w}_i$		species production rate of species i, kg/m^3-s

X_i		mole fraction of species i	τ		shear stress, N/m^2
x		streamwise spatial variable, m	ϕ		equivalence ratio
Δx		spatial step size, m	Ω_D		diffusion collision integral
y	(Y)	transverse spatial variable, m	∇		Laplacian operator

Subscripts:

Δy	transverse spatial step size, m	
γ	stoichiometric coefficient, ratio of specific heats	c based on chemistry
δ	Kronecker delta function; central spatial difference operator	f based on fluids
η	computational transverse coordinate	i,j species indices
λ	eigenvalue; second coefficient of viscosity, kg/m-s	m mixture
μ	laminar viscosity, kg/m-s	R reactions, reference value
ξ	computational streamwise coordinate	s species
ρ	density, kg/m^3	sp evaluated spectrally
σ	normal stress, N/m^2; effective collision diameter	x in x coordinate direction
σ_{ij}	effective collision diameter, Å	y in y coordinate direction

Symbol	Definition
X_i	mole fraction of species i
x	streamwise spatial variable, m
Δx	spatial step size, m
y $\quad(Y)$	transverse spatial variable, m
Δy	transverse spatial step size, m
γ	stoichiometric coefficient, ratio of specific heats
δ	Kronecker delta function; central spatial difference operator
η	computational transverse coordinate
λ	eigenvalue; second coefficient of viscosity, kg/m-s
μ	laminar viscosity, kg/m-s
ξ	computational streamwise coordinate
ρ	density, kg/m^3
σ	normal stress, N/m^2; effective collision diameter
σ_{ij}	effective collision diameter, Å

Right column:

Symbol	Definition
τ	shear stress, N/m^2
ϕ	equivalence ratio
Ω_D	diffusion collision integral
∇	Laplacian operator

Subscripts:

Symbol	Definition
c	based on chemistry
f	based on fluids
i,j	species indices
m	mixture
R	reactions, reference value
s	species
sp	evaluated spectrally
x	in x coordinate direction
y	in y coordinate direction

Superscripts:

Symbol	Definition
n	time level
$-$	mass-weighted value
$'$	derivative, fluctuating quantity, reactants
$''$	products

Summary

Research has been undertaken to achieve an improved understanding of physical phenomena present when a supersonic flow undergoes chemical reaction. A detailed understanding of supersonic reacting flows is necessary to successfully develop advanced propulsion systems now planned for use late in this century and beyond. In order to explore such flows, a study was begun to create appropriate physical models for describing supersonic combustion and to develop accurate and efficient numerical techniques for solving the governing equations that result from these models. From this work, two computer programs were written to study reacting flows. Both programs were constructed to consider the multicomponent diffusion and convection of important chemical species, the finite-rate reaction of these species, and the resulting interaction of the fluid mechanics and the chemistry. The first program employed a finite-difference scheme for integrating the governing equations, whereas the second used a hybrid Chebyshev pseudospectral technique for improved accuracy. Both programs were used to study a spatially developing and reacting mixing layer, and the results were analyzed to draw conclusions regarding the structure of the evolving layer.

1. Introduction

Research is currently underway, both in the United States and abroad, to develop advanced aerospace propulsion systems now planned for use late in this century and beyond. One such program is being carried out at the NASA Langley Research Center to develop a hydrogen-fueled supersonic combustion ramjet engine, also known as a scramjet, capable of propelling a vehicle at hypersonic speeds in the atmosphere. One phase of this research has been directed toward gaining a detailed understanding of the complex flow field present in the engine over a range of flow conditions. Numerical modeling of various regions of the engine flow field has been shown to be a valuable tool for gaining insight into the nature of these flows. This approach has been used in conjunction with an ongoing experimental program to develop an effective analysis capability (ref. 1).

The flow field in a scramjet engine is governed by the Navier-Stokes equations coupled to a system of equations describing each of the species present initially and produced by chemical reaction. The governing equations were solved in prior analyses using either explicit or implicit finite-difference techniques, with the chemical reaction process modeled by an ideal (mixing controlled) reaction model. Using these approaches, analyses of various ramjet and scramjet configurations have been carried out, and trends that were established by experiments have been predicted (refs. 2 and 3).

Chemical reaction is not mixing controlled throughout a scramjet combustor, however. Although chemical reaction may equilibrate in the rearward region of a well-designed combustor, chemistry in the forward portions of the combustor is certainly kinetically controlled. Finite-rate kinetics is, in fact, a critical issue in the design of flameholders in the engine, and this phenomenon must be considered along with the effects of molecular and turbulent fuel-air mixing to develop an accurate engine flow model. It is for this reason that attention has turned in the present work to a more basic and detailed analysis of chemically reacting flow fields. The long-term purpose of the present research is to develop detailed models for fuel-air mixing and reaction in an engine flow field and to develop accurate and efficient numerical methods for solving the equations governing reacting flow that result from these models.

Because of computer resource limitations, however, detailed modeling of the complete engine problem cannot be considered at the present time. A more tractable problem that relaxes only the complexities introduced by engine geometry is posed by the spatially developing, primarily supersonic, chemically reacting two-dimensional mixing layer. A major portion of the chemical reaction taking place in a supersonic combustor occurs in mixing layers. All the difficulties introduced by the fluid mechanics, combustion chemistry, and interactions between these phenomena are retained by the reacting mixing layer, making it an ideal problem for the detailed study of supersonic reacting flow.

Prior studies on supersonic reacting mixing layers have been quite limited. A fair amount of work has been carried out, however, on nonreacting mixing layers, both supersonic and subsonic. Even without combustion, the results of these studies provided a significant amount of useful information for understanding reacting layers. Carpenter (ref. 4) studied the development of a laminar, free-shear layer behind steps and blunt bodies over a Mach number range of 0 to 10. He concluded that the development of the layer could best be understood in terms of vorticity transfer. The effect of compressibility was to increase the diffusion process in the layer, leading to more rapid development toward asymptotic conditions with increasing Mach number. Brown and Roshko (ref. 5) studied the subsonic mixing layer that developed between nitrogen and helium streams and found that the layer was dominated by large-scale coherent vortical structures. They found that these structures tended to convect at a nearly

constant speed and that the size of the structures and the space between them changed discontinuously with movement downstream by the joining of those structures with their neighbors. Results of their experiment "suggested that turbulent mixing and entrainment was a process of entanglement on the scale of the large structures." They also found that very large changes in the density ratio (up to 49) measured transversely across the mixing layer had only a small effect on spreading of the layer. The authors concluded, therefore, that the significant reduction in supersonic mixing layer growth rate with increasing Mach number was due primarily to compressibility effects, rather than density effects as had been thought in the past.

The role of coherent structures in turbulent processes in mixing layers was studied further by Roshko (ref. 6). He found that the size of the coherent structures and the spacing between them increased with increasing downstream distance. The vortices were found to travel at a constant speed of $(u_1 + u_2)/2$, where u_1 and u_2 are the free-stream velocities of the two streams making up the layer. Each vortex also had a finite life span that began and ended abruptly. Coincident with two or more of these endings, a new lifespan began, with two or more vortices coalescing to form a new larger vortex. As noted above, each of these vortices was observed to move at a nearly constant speed, resulting in a fairly constant spacing between a vortex and its neighbor as they moved downstream during their lifetime. Developed mixing layers are self-similar, however, requiring that the spacing between vortices should increase linearly in the mean with increasing downstream distance. Roshko resolved this contradiction by reasoning that changes in the layer must occur discontinuously and irregularly along the layer such that the scale of the structure grew smoothly and linearly in the mean. Roshko further found that in the transition region of the layer, there was only one spacing distance between neighboring vortices, and this spacing represented the most stable wavelength selected by the laminar portion of the layer. In this region the scales had not yet become dispersed, as they did further downstream in the turbulent regime. Also, three-dimensional effects had not come into play in the transition region. Finally, Roshko noted that mixing layer growth likely occurred not just due to vortex pairing, but also through an entrainment process by each vortex that occurred near or during the pairing event. Entrainment brought together "pieces" of fluid from either side of the layer, also enhancing the mixing process. Between each of these pairing/entrainment events, the vortices appeared to convect in an apparently passive fashion.

Ferziger and McMillan (ref. 7) in studies of the structure in turbulent shear flows also noted the presence of coherent structures and pairing in a developing mixing layer. They went on to discuss the importance of a tearing mechanism where vortices tended to be torn apart by shearing and then redistributed in parts to their neighboring vortices. They also pointed out the importance of three-dimensional effects in destabilizing the layer. The coherent structures present in the mixing layer tended to be unstable to three-dimensional perturbations that destroyed the spanwise coherence of the structures. Finally, the authors also noted that three-dimensional effects could also be introduced by streamwise vorticity produced by the stretching of vortical structures.

There has been additional work in the literature describing important structures present in developing mixing layers, but the authors have gone on to seek specific mechanisms leading to the production of the structures and their effect on the flow. Several of these authors have dealt particularly with mechanisms associated with retardation of mixing in the supersonic development of layers. Oh (ref. 8) hypothesized that when the local mean Mach number exceeded 1, some fraction of the turbulence energy in the flow was generated by shocks that formed about the eddies (eddy shocks). These shocks were quite weak, differing little from Mach waves, but having finite strength. Some of the eddies in the flow were decelerated by passing through these shocks, and the resulting disturbances produced pressure fluctuations. These fluctuations appeared to correlate well with velocity and density fluctuations in the flow. Favorable correlations in fluctuations of pressure and velocity gradient gave rise to values of the pressure dilation term $p'\partial u'_j/\partial x_j$ that acted as a source or sink of turbulent kinetic energy in the flow. This term vanished in incompressible flows and in low-speed mixing flows where there was a large density variation. The term took on larger values, however, in high Mach number free-mixing layers and acted as a turbulent kinetic energy sink when gradients of mean Mach number and density had the same sign. Therefore, Oh reasoned that the pressure dilation term could act to reduce the turbulent shear level in high Mach number mixing layers, thereby slowing the growth of the layer relative to the incompressible case. This effect agreed with the results cited earlier in this paper. Oh then carried out calculations by using these ideas that appeared to validate his hypothesis. Papamoschou and Roshko (ref. 9) also observed that the spreading rate of compressible mixing layers was significantly reduced over that of incompressible layers, and they attributed that difference to compressibility effects. They deduced from their

2

studies of large-scale structures in the layer that it was appropriate to define a natural coordinate system that moved with these structures. With this system, an alternative Mach number, termed the convective Mach number M_c was defined as $M_c = (u - u_c)/a$, where u is the free-stream velocity, u_c is the convection velocity of the large-scale structures, and a is the local speed of sound. The reduction in mixing layer spreading rate (by approximately a factor of 3 or 4) was shown to correlate well with increasing convective Mach number beginning with $M_c \approx 0.5$ and leveling off for $M_c > 1.0$. Reduced spreading therefore seemed to the authors to be due to a stabilizing effect of the convective Mach number.

Hussaini, Collier, and Bushnell (ref. 10) offered a possible explanation for the correlation of mixing-layer spreading rate with convective Mach number. Their explanation was tied to the formation of the eddy shocklets that were described earlier. The authors studied numerically the behavior of an eddy convecting subsonically, relative to a locally supersonic flow, with a convective Mach number greater than one. Such flows could therefore support transient shock structures associated with the eddies. As the eddy accelerated in the supersonic flow, an eddy shocklet formed which tended to distort the eddy. As this process continued, an eddy bifurcation occurred, resulting in the formation of a vortex of opposite circulation. Additionally, the length scale of the original vortex was reduced. Therefore, it was seen that eddy shocklets could reduce turbulent mixing through both the production of counter fluctuating vorticity and the reduction of turbulence scale. The authors stated that the mechanism for these effects resulted from the instantaneous inviscid pressure field induced about the front of the eddy. The authors further noted that the induced pressure field would always counter the initial vortex circulation over a portion of its contour, and for long enough times and weak enough eddies, the formation of counter vorticity and consequent eddy splitting would occur, resulting in a significant alteration of the mixing-layer structure.

Many, if not all, of the important features described above for nonreacting subsonic and supersonic mixing layers also occurred in reacting layers. A majority of the studies on reacting mixing layers were carried out at subsonic rather than supersonic speeds, however. Yule, Chigier, and Thompson (ref. 11) found that, consistent with non-reacting flow, many combusting flows contained coherent burning structures that interacted as they were convected downstream. They termed the burning region associated and moving with an eddy a "flamelet" and found that the flamelet formed in only part of an eddy. They found a range of eddy types existed in a diffusion flame (that occurred in a nonpremixed reacting mixing layer). Initially there existed unstable laminar flow that contained an unstable laminar diffusion flame. That region was followed by one containing sheets of vortex rings with smooth tongues of flame at the interfaces between the vortices and unburned reactants. This region was followed by a zone of other orderly vortex structures, including helical vortices, which also produced relatively smooth tongues of flame. This zone contained the characteristics of transition observed in nonreacting flow. Here, viscous forces have a stabilizing influence on the flow. As the viscous forces became less important and inertial forces predominated further downstream, the authors found that the orderliness of the eddies decreased and the flow became increasingly unstable and three-dimensional. With the introduction of three-dimensional effects, randomly moving cell-like flamelets also appeared. Even further downstream, this process evolved into a fully turbulent flow with eddies containing coherent ragged regions of burning, forming islands that were completely separated from the main flame. Yule et al. (ref. 11) also examined the structure of a single eddy containing a flamelet in a simple gas diffusion flame. The basic structure of a transitional eddy before it interacted with other eddies is given in figure 1, which was taken from reference 11. The eddy contained separate regions of fuel and air that rolled up into the vortex, as well as a viscous core containing a mixture of fuel, oxidants, and products. A flame existed along the interface region where large transverse gradients of temperature and species concentration occurred. The local thickness of this region depended on the residence time and strength of the vortex, the local diffusion coefficients, and chemical kinetics. The molecular mixing required before fuel and air react was enhanced in the eddy by stretching of the fuel/air interface due to the vorticity that the eddy contained. Preheating of fuel and air then took place primarily along the interface zone where mixing was taking place on a molecular scale. Combustion then occurred in the interface at or near stoichiometric conditions. During these processes, the vortex continued to convect downstream, and the induced velocity within the eddy due to its vorticity continued to produce valleys and an increase in vortex dimensions. This eddy growth resulted in further entrainment of fuel and air, producing flame and mixing layer growth.

Yule et al. (ref. 11) then went on to discuss the evolution of turbulent eddies from transitional eddies. The structure is pictured in figure 2, again taken from reference 11. The eddy has now taken

on a three-dimensional structure, and it has begun to lose the circumferential coherence about its associated flamelet. Additionally, there now existed an irregular vorticity distribution within the eddy, which was interpreted to be due to the presence of smaller eddy scales now existing within the main eddy. Mixing down to molecular levels was still produced by vortical stretching, and the process appeared, in fact, to be more pronounced in the turbulent eddy. In addition, the irregularity of the structure also produced a range of flamelet structures, resulting in a "ragged" flame front trailing the eddy. The authors concluded their study of large coherent structures in reacting flow by noting that such structures could lead to overall reduced combustion efficiency because of unmixedness. Unmixedness occurred when fuel and air could not effectively mix because each gas was bound up in vortical structures during its passage through a combustion region. They did suggest that large eddies could be broken up by increasing the shear stresses in the flow in regions of steep velocity gradient or by the imposition of swirl into the flow.

Masutani and Bowman (ref. 12) also studied the structure of a chemically reacting plane mixing layer. They examined the reaction in the mixing layer between a stream of dilute nitrous oxide and a stream of dilute ozone and observed similar behavior to that seen by the previous authors. They found that the mixing layer had three streamwise states. First, there existed fingers of unmixed free-stream fluid that sometimes reached entirely across the layer. Next, there appeared a region of mixed fluid in a finite-thickness interfacial diffusion zone that bordered parcels of unmixed fluid. Finally, the layer consisted of regions of mixed fluid of nearly homogeneous composition in a global sense.

Keller and Daily (ref. 13) conducted an experimental study of a gaseous, two-stream, reacting mixing layer flow fueled by propane, with one stream made of hot combustion products and the other stream containing cold unburnt reactants. They found that the mixing layer structure was qualitatively unaffected by heat release for the range of conditions that they studied. Mungal, Dimotakis, and Hermanson (ref. 14) experimentally studied the reacting mixing layer created between a dilute hydrogen stream and a dilute fluorine stream over a wide range of conditions. They also observed the presence of large hot coherent structures in the layer that strongly influenced the mixing and entrainment of fuel and oxidant and the overall structure of the flow field.

Hermanson, Mungal, and Dimotakis (ref. 15) extended the work described in reference 14, but with significantly higher heat release. They found that at the higher temperature resulting in this case, the flow still appeared to be dominated by large-scale structures that were separated by cold tongues of fluid that extended well into the layer. Thus, the structure did not appear to be altered by heat release and continued to be predominantly two-dimensional. They also found that with significant heating and the resulting large density changes, the shear layer thickness did not increase, and in fact showed a slight decrease. This reduction in layer thickness with increasing heat release was further confirmed by the resulting velocity profiles that showed noticeably higher values of transverse velocity gradient with increased heating. The authors then went further to note that since the layer width did not increase with temperature, and since the density of the layer was substantially reduced by heating, the volumetric entrainment rate of free-stream fluid into the layer must also be greatly reduced by heat release. Pitz and Daily (ref. 16) carried out an experiment to study a turbulent propane-air mixing layer downstream of a rearward facing step. They also found that large-scale structures dominated the flow and that the growth of these eddies influenced the reaction zone. Reaction took place mainly in the eddies, although the eddies were not confined to the velocity gradient region of the layer. Therefore, the resulting flame spread faster into the premixed reactants than did the mixing layer defined by the mean velocity. Thus, the region of the mixing layer defined by the velocity gradient did not coincide with the region of high chemical reaction and heat transfer. Broadwell and Dimotakis (ref. 17) surveyed a number of recent papers describing experiments on reacting mixing layers. Based on these papers and their experience, they then discussed the implications for modeling such flows. Their three principal conclusions were that molecular transport retained a significant role in turbulent mixing phenomena, even when the flow was fully developed; large-scale structures controlled entrainment, which then provided conditions for the subsequent mixing processes; and mixing layers remained unsteady at the largest temporal and spatial scales.

Reacting mixing layer studies using analytical or numerical approaches have also been carried out. Carrier, Fendell, and Marble (ref. 18) used a singular perturbation technique to modify their Burke-Schumann thin flame solution for a more realistic finite-thickness reaction zone in a mixing layer. They studied the effect of fluid strain on the flame; their strain increased the interfacial exposure of fuel and oxidant, and convected additional reactant into the flame. Riley and Metcalfe (ref. 19) directly simulated a subsonic, temporally developing and

reacting mixing layer by using a pseudospectral numerical method and a binary single-step irreversible reaction with no heat release. Using this approach, they were able to consider the effect of the turbulence field on chemical reaction. Their results were shown to be consistent with similarity theory and in approximate agreement with experimental data. McMurtry, Jou, Riley, and Metcalfe (ref. 20) extended the preceding work to consider the effect of chemical heat release on a subsonic, temporally developing mixing layer. They solved both the compressible form of the governing equations as well as a more computationally efficient form of the equations valid for low Mach numbers. Reaction was again modeled with a binary, single-step, irreversible reaction. The authors found with their simulations that the thickness of the mixing layer and the amount of mass entrained into the layer decreased when the heat release rate due to exothermic reaction was increased. Likewise, the resulting product formation also decreased as the heat release rate increased.

Menon, Anderson, and Pai (ref. 21) studied the stability of a laminar, premixed, spatially developing, supersonic mixing layer undergoing chemical reaction. They introduced an infinitesimal disturbance into the layer and examined its spatial stability for both reacting and nonreacting flows. Chemical reaction was shown to have a significant effect on flow stability. The authors found that with reaction, the disturbance amplification rate was higher and the wave speed lower as compared with nonreactive cases. Also, the free-stream Mach number was shown to have little effect on stability when the flow was reacting.

In this study, a numerical model has been developed for describing general two-dimensional, high subsonic or supersonic, chemically reacting flows. This model was then adapted to a supersonic, chemically reacting mixing layer. Reaction in many practical devices takes place in mixing layers, so that the problem chosen, while being geometrically simple, still retained the fluid mechanical and chemical complexities that were under consideration. Computer programs have been developed that numerically solve the governing equations resulting from the model. The programs used either a modified MacCormack technique or a hybrid Chebyshev pseudospectral technique to solve the Navier-Stokes and species continuity equations that describe multiple species undergoing chemical reaction. Momentum, heat, and mass diffusion were described by laws based on kinetic theory; chemistry was defined with a multicomponent finite-rate scheme; and a real gas thermodynamics model was employed.

Using the computer programs developed in this work, detailed studies of the supersonic, spatially developing and reacting mixing layer were undertaken. The accuracy of the finite-difference and spectral programs was compared for a simple test case. No attempt was made at this point, however, to choose the preferred approach. Several phenomena observed only for subsonic reacting mixing layer flows were then sought in the supersonic layer by using both methods. The studies were undertaken, first, to verify the existence of the phenomena, and second, to explore the effect of the phenomena upon the development of a supersonic layer relative to that observed in the subsonic layer.

Because of their importance in subsonic layers, consideration was given first to the existence of vortical structures in a supersonic reacting mixing layer. The effects of such structures on the development of the layer were then explored and compared with the literature cited earlier. Particular emphasis was given in this study to the mixing of fuel and oxidant in the layer, the resulting chemical reaction, the effect of chemical heat release on mixing, and the existence of supersonic unmixedness. The stability of a supersonic reacting mixing layer was also explored in this work. The existence of a transition zone in a particular mixing layer configuration was first considered, and then mechanisms necessary to produce transition of the layer were examined. Emphasis was also given to the effects of transition on fuel-oxidant mixing and chemical reaction in the zone, and the effects of chemical heat release were again considered in this region.

The development of the numerical methods employed in this study is given in section 2 along with appropriate calculations to check the methods. Section 3 describes extensions of the methods developed in section 2 to two dimensions. The detailed physical models used to describe the complex reacting flows to be studied are also described in this section. Finally, section 4 describes studies of several supersonic reacting mixing layer cases using the finite-difference and spectral computer codes that were developed. Conclusions resulting from the mixing layer studies of section 4 are given in section 5. Based on these conclusions, directions for further research in supersonic chemically reacting flows are then discussed.

2. Development of Numerical Methods

The numerical methods to be employed for studying chemically reacting flows are developed in this section. Two classes of algorithms are developed, the first based on established finite-difference techniques and the second based on spectral techniques. Spectral schemes are high-order methods and offer

the high level of accuracy required for combustion studies. These methods have been used quite successfully in studies of transition of flows from laminar to turbulent states, problems not unlike those to be considered in this work.

To solve the equations governing chemically reacting flows, the spatial derivatives must first be discretized, and then an appropriate temporal discretization must be chosen in order to advance the equations ahead in time. The temporal scheme must be chosen carefully because the system of partial differential equations describing chemically reacting flows can be stiff because of the highly disparate time scales that exist among the equations. Certain chemical reactions in a combustion kinetics system can take place on an extremely short scale of the order of 10^{-9} seconds, whereas the fluid dynamics may require from 10^{-3} to 10 seconds for a typical case to reach steady-state conditions. (Time scales as small as 10^{-12} seconds were observed in these studies, but these scales were later found to arise from nonphysical behavior of certain global chemistry models at early integration times.) There are, of course, several intermediate scales lying between these two extremes. Mathematically, stiffness is often defined by examining the eigenvalues of the Jacobian of the governing equation system and noting that the ratio of the real part of the largest to real part of the smallest eigenvalue is a large number. The former physical definition is perhaps the more useful test of stiffness; it is felt directly in the numerical integration of stiff systems through the required proper choice of the integration time step. This requirement will be dealt with now, and then a discussion will follow concerning integration of the spatial part of the problem.

Stiffness in the system of equations governing chemically reacting flows typically arises from the source terms in the equations describing production and loss of the chemical species that are present. Large values for these source terms produce rapid changes in the dependent variables being sought and result in the very short time scales discussed in the previous paragraph. To explore the problem of mixed (short and long) time scales, consider the ordinary differential equation (ODE) system (ref. 22)

$$\frac{d\mathbf{f}}{dt} = [A]\mathbf{f} \tag{1}$$

where $\mathbf{f} = [f_1, f_2]^T$, $\mathbf{f}(0) = [2, 1]^T$, and

$$A = \begin{bmatrix} -500.5 & 499.5 \\ 499.5 & -500.5 \end{bmatrix}$$

The eigenvalues of $[A]$ are $\lambda_1 = -1000.0$ and $\lambda_2 = -1.0$, and the solution to equation (1) follows as

$$\left. \begin{aligned} f_1(t) &= 1.5e^{-t} + 0.5e^{-1000t} \\ f_2(t) &= 1.5e^{-t} - 0.5e^{-1000t} \end{aligned} \right\} \tag{2}$$

Note that the solutions f_1 and f_2 have a rapidly decaying component corresponding to λ_1 and a much more slowly decaying component corresponding to λ_2. If this problem were solved numerically, accuracy would require that the solution be advanced from the initial conditions by using very small time steps. However, once the solution dominated by λ_1 decays, it is preferable to advance the solution by using larger time steps that would still maintain an acceptable level of accuracy. Care must be taken in picking a numerical algorithm that will allow this choice of time step. Otherwise, the numerical stability of the solution continues to be dictated by λ_1 even though its component has decayed, and very small time steps are still required to maintain stability. In response to this difficulty, several authors, including Bussing and Murman (ref. 23); Stalnaker et al. (ref. 24); Widhopf and Victoria (ref. 25); and Smoot, Hecker, and Williams (ref. 26) recognized that the stiff source terms in the system of equations governing chemically reacting flow should be evaluated implicitly. Therefore, for these studies, algorithms are developed with the source terms written implicitly at the new time level in the integration step. Other terms in the governing equations that do not lead to stiffness can still be evaluated explicitly (refs. 23–26).

Next, the computation of spatial derivatives in the governing equations is considered. The importance of accurately modeling spatial derivatives cannot be overemphasized. Chemical reaction does not take place until fuel and oxidant are brought together and macroscopically mixed by convective transport and then mixed down to the microscopic (molecular) level by diffusive processes. To model these processes, spatial derivatives must be accurately computed. Because of computer storage limitations, higher order numerical methods were indicated.

Higher order finite-difference schemes offered one option for computing the spatial derivatives. Another option was apparent from earlier studies where methods were developed for computing highly accurate solutions of the Euler equations. In one study, Hussaini et al. (refs. 27 and 28) used a spectral collocation method to compute the required spatial derivatives in the governing equations. With this approach, several problems governed by the Euler equations were successfully solved and accurate solutions were obtained on relatively coarse grids as compared

with finite-difference solutions of the same problems. Spectral methods are based on the representation of the solution to a problem f by a finite series of global functions X of the form

$$f(x) = \sum_{n=0}^{N} \widehat{a}_n X_n(x) \qquad (3)$$

where $\widehat{a}_n$ are the expansion coefficients of the series (ref. 29) and X_n should be a complete orthogonal set. Spatial derivatives of f are then approximated by taking derivatives of the corresponding series (eq. (3)). If properly applied, the high order approximation given by equation (3) yields a very accurate numerical representation for derivatives of f. Spectral methods therefore satisfy the requirements for approximating spatial derivatives in the equations governing a chemically reacting flow field.

Two second-order finite-difference discretizations of the spatial derivatives are also developed, both to demonstrate the advantages offered by the higher order scheme and to provide benchmark results with more conventional approaches. In the first approach, second-order central finite differences are used to discretize the spatial derivatives. In the second approach, first-order forward and backward finite differences are used in combination with a predictor-corrector temporal discretization to yield a second-order method in space.

With the approaches described above for temporally and spatially discretizing the governing equations, three numerical algorithms, one using spectral methods and two using finite-difference schemes, are developed for solving the equations governing a chemically reacting flow. The spectral algorithm (ref. 30) employs a two-stage partial implicit Runge-Kutta scheme for integrating the equations in time (ref. 23) and a Chebyshev spectral collocation method for computing spatial derivatives in the equations. The first finite-difference algorithm uses a partial implicit Adams-Moulton scheme to integrate the equations in time and central finite differences to integrate the equations in space. The second finite-difference scheme employs a partial implicit MacCormack predictor-corrector scheme to integrate the governing equations in time and space (refs. 23, 24, and 31). Computer programs have been written to apply these algorithms to the solution of reacting flow problems (ref. 30). The codes are limited in this section to quasi-one-dimensional inviscid flows with hydrogen-air reaction, which is appropriate for the development and evaluation of the algorithms. Chemical reaction is represented in the

programs with a finite-rate chemistry model, and a real gas thermodynamic model is employed.

2.1 Governing Equations

The quasi-one-dimensional Euler equations in conservation law form with multiple species undergoing chemical reaction are (ref. 32)

$$\frac{\partial \mathbf{U}}{\partial t} + \frac{\partial \mathbf{F}}{\partial x} + \mathbf{H} = 0 \qquad (4)$$

where for $i = 1, 2, \ldots, N_s - 1$,

$$\mathbf{U} = \{\rho A, \rho u A, \rho e_o A, \rho f_i A\}^T \qquad (i = 1, 2, \ldots, N_s - 1) \quad (5)$$

$$\mathbf{F} = \left\{\rho u A, \rho u^2 A + p A, \rho u h_o A, \rho u f_i A\right\}^T \qquad (6)$$

$$\mathbf{H} = \left\{O, -p\frac{dA(x)}{dx}, O, -\dot{w}_i A\right\}^T \qquad (7)$$

and

$$h_o = \int_{T_R}^{T} \bar{c}_p \, dT + \frac{u^2}{2} + \sum_{i=1}^{N_s} \left(H_T^o\right)_i f_i \qquad (8)$$

$$e_o = h_o - \left(\frac{R^o}{\overline{M}}\right) T \qquad (9)$$

where $(H_T^o)_i$ is the reference enthalpy of species i at the reference temperature $T_R = 0$ K (ref. 33). If there are N_s chemical species, then $i = 1, 2, \ldots, (N_s - 1)$ and $(N_s - 1)$ equations must be solved for the species f_i. The final species mass fraction f_{N_s} can then be found by conservation of mass since

$$\sum_{i=1}^{N_s} f_i = 1$$

2.2 Chemistry Model

The chemical reaction of hydrogen and oxygen is modeled here with the global finite-rate hydrogen-air chemistry model of Rogers and Chinitz (ref. 34). This model adequately represents the chemical reaction taking place in the problems to be considered in this chapter, and it also produces an extremely large disparity in the time scales in the problems. This phenomenon allows the ability of the numerical algorithm to deal with resulting stiffness to be demonstrated.

The Rogers-Chinitz model assumes that the overall reaction of hydrogen and oxygen takes place

through two reactions, the first resulting in the formation of the hydroxyl radical, and the second combining the hydroxyl radical with hydrogen to form water. (More general models are needed, however, to properly represent the ignition stage of hydrogen-air reaction. These models are used in the more physically detailed work described in section 3.) The reactions are given by

$$(1) \qquad H_2 + O_2 \underset{k_{b1}}{\overset{k_{f1}}{\rightleftharpoons}} 2OH$$

$$(2) \qquad 2OH + H_2 \underset{k_{b2}}{\overset{k_{f2}}{\rightleftharpoons}} 2H_2O$$
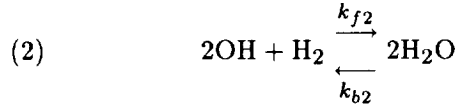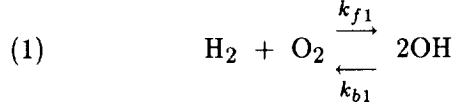
where k_f is the forward reaction rate and k_b is the reverse reaction rate. The reverse rate can be found given the forward rate and equilibrium constant K for each reaction, as

$$k_b = k_f/K \qquad (10)$$

The forward reaction rates are computed from the modified Arrhenius law,

$$k_{f_i} = A_i T^{N_i} e^{-E_i/R^\circ T} \qquad (11)$$

for each reaction i. For the Rogers-Chinitz model, the rates are given by (ref. 34)

$$k_{f1} = A_1 T^{-10} e^{-4865/R^\circ T}, \qquad \frac{cm^3}{mole\text{-}sec} \qquad (12)$$

$$k_{f2} = A_2 T^{-13} e^{-42500/R^\circ T}, \qquad \frac{cm^6}{mole^2\text{-}sec} \qquad (13)$$

where

$$A_1 = \left(8.917\phi + \frac{31.433}{\phi} - 28.95 \right) 10^{47}$$

$$A_2 = \left(2.0 + \frac{1.333}{\phi} - 0.833\phi \right) 10^{64}$$

and

$$K_1 = 26.164 \, e^{-8992/T}$$

$$K_2 = 2.682 \times 10^{-6} T \, e^{69415/T}$$

Knowing the reaction rates for the reactions defined by (1) and (2), the production of the four species

present in the model can be found from the law of mass action. For a general reaction

$$\sum_{j=1}^{N_s} \gamma'_{ij} C_j \underset{k_{b_i}}{\overset{k_{f_i}}{\rightleftharpoons}} \sum_{j=1}^{N_s} \gamma''_{ij} C_j \qquad (i = 1, 2, \dots, N_R)$$

the law of mass action states that the rate of change of concentration of species j by reaction i is given by (ref. 35)

$$\left(\dot{C}_j \right)_i = \left(\gamma''_{ij} - \gamma'_{ij} \right) \left(k_{fi} \prod_{j=1}^{N_s} C_j^{\gamma'_{ij}} - k_{bi} \prod_{j=1}^{N_s} C_j^{\gamma''_{ij}} \right) \qquad (14)$$

The rate change in concentration of species j by all N_R reactions is then found by summing the contributions from each reaction,

$$\dot{C}_j = \sum_{i=1}^{N_R} \left(\dot{C}_j \right)_i \qquad (15)$$

Finally, the production rate of species j is found from

$$\dot{w}_j = \dot{C}_j M_j \qquad (16)$$

Applying the law of mass action to the global model, reactions (1) and (2), gives (ref. 34)

$$\dot{C}_{O_2} = -k_{f1} C_{H_2} C_{O_2} + k_{b1} C_{OH}^2 \qquad (17)$$

$$\dot{C}_{H_2O} = 2 \left(k_{f2} C_{OH}^2 C_{H_2} - k_{b2} C_{H_2O}^2 \right) \qquad (18)$$

$$\dot{C}_{H_2} = \dot{C}_{O_2} - \frac{1}{2} \dot{C}_{H_2O} \qquad (19)$$

$$\dot{C}_{OH} = - \left(2 \dot{C}_{O_2} + \dot{C}_{H_2O} \right) \qquad (20)$$

The source terms for the last i equations in equation (4) can now be determined, as a function of the dependent variables, by application of equation (16).

2.3 Thermodynamics Model

The specific heat at constant pressure, c_p, is nearly a linear function of temperature for each species present in the flow field (H_2, O_2, OH, H_2O, N_2) over the range of temperature being considered in this section. To simplify the analysis, c_p versus temperature data (ref. 33) for each species i is therefore fit with

$$c_{p_i}(T) = a_i T + b_i \qquad (21)$$

8

where a and b are constants. A mixture specific heat, $\bar{c}_p$, can then be defined by weighting over the species i as

$$\bar{c}_p = \sum_{i=1}^{N_s} c_{p_i} f_i \qquad (22)$$

The total enthalpy of the mixture, made up of the five species, is given by

$$H = \sum_{i=1}^{N_s} f_i \left(\int_{T_R}^{T} c_{p_i} \, dT + (H_T^o)_i \right) + \frac{u^2}{2} \qquad (23)$$

Putting equation (22) into (23) and integrating gives

$$H = \sum_{i=1}^{N_s} f_i \left(\frac{a_i T^2}{2} + b_i T + (H_T^o)_i \right) + \frac{u^2}{2} \qquad (24)$$

Finally, the mixture gas constant $\bar{R}$ is found by weighting the individual gas constants over the species i as

$$\bar{R} = \sum_{i=1}^{N_s} R_i f_i \qquad (25)$$

Equations (22), (24), and (25) can then be used to define all other required thermodynamic variables.

2.4 Chebyshev Spectral Method

2.4.1 Spatial discretization. The Chebyshev spectral collocation method (ref. 28) is used to define the derivatives $\partial F/\partial x$ in equation (4). To define $\partial F/\partial x$, F is expanded in terms of the Chebyshev polynomials

$$T_n(x) = \cos(n \cos^{-1} x) \qquad (26)$$

in the truncated Chebyshev series

$$\mathbf{F}(x) = \sum_{n=0}^{N} \widehat{\mathbf{F}}_n T_n(x) \qquad (27)$$

where $\widehat{\mathbf{F}}_n$ represents the expansion coefficients of the series. To form a range on x, the change of variables

$$x = \cos \theta \qquad (0 \le \theta \le \pi) \qquad (28)$$

is introduced. Putting equation (28) into (26) and introducing the resulting expression into (27) gives

$$\mathbf{F}(x) = \sum_{n=0}^{N} \widehat{\mathbf{F}}_n \cos(n\theta) \qquad (29)$$

a Fourier cosine series. To discretize equation (29), a set of collocation points x_j is defined by

$$x_j = \cos\left(\frac{\pi j}{N}\right) \qquad (j = 0, 1, 2, \ldots, N) \qquad (30)$$

and the discrete form of equation (29) becomes

$$\mathbf{F}_j = \mathbf{F}(x_j) = \sum_{n=0}^{N} \widehat{\mathbf{F}}_n \cos\left(\frac{n\pi j}{N}\right) \qquad (31)$$

The inverse of equation (31) gives $\widehat{\mathbf{F}}_n$ and can be found as follows. First, multiply equation (27) on both sides by $T_m(x)$ and weight $(1 - x^2)^{-1/2}$, and then integrate over the interval [-1,1]. This gives

$$\int_{-1}^{1} \mathbf{F}(x) \left(1 - x^2\right)^{-1/2} T_m(x) \, dx$$

$$= \sum_{n=0}^{N} \widehat{\mathbf{F}}_n \int_{-1}^{1} \left(1 - x^2\right)^{-1/2} T_n(x) T_m(x) \, dx$$

Making the transformation $x = \cos\theta$ yields

$$\int_{-1}^{1} \left(1 - x^2\right)^{-1/2} T_n(x) T_m(x) \, dx$$

$$= -\int_{\pi}^{0} \cos(n\theta) \cos(m\theta) \, d\theta$$

$$= \frac{\pi}{2} \bar{c}_n \delta_{nm}$$

where

$$\bar{c}_n = \begin{cases} 2 & n = 0 \text{ or } n = N \\ 1 & 1 \le n \le (N-1) \end{cases}$$

Therefore

$$\widehat{\mathbf{F}}_n = \frac{2}{\pi \bar{c}_n} \int_{-1}^{1} \left(1 - x^2\right)^{-1/2} \mathbf{F}(x) \, T_n(x) \, dx$$

Again let $x = \cos\theta$ and

$$\widehat{\mathbf{F}}_n = \frac{2}{\pi \bar{c}_n n} \int_{0}^{n\pi} \mathbf{F}(\theta) \, \cos(n\theta) \, d(n\theta)$$

To generate a discrete set of Chebyshev coefficients, the trapezoidal rule of integration

$$I = \sum_{n=0}^{N} I_n = \frac{h}{2} \sum_{n=0}^{N} (g_n + g_{n+1})$$

9

is employed, where I is the value of the integral, h is the integration step size, and g is the integrand. The expression for discrete values of $\widehat{\mathbf{F}}_n$ then becomes

$$\widehat{\mathbf{F}}_n = \frac{2}{\pi \bar{c}_n n} \frac{n\pi}{2N} \sum_{j=0}^{N-1} \left[\mathbf{F}_j T_n \left(x_j \right) + \mathbf{F}_{j+1} T_n \left(x_{j+1} \right) \right]$$

$$= \frac{1}{\bar{c}_n N} \left[\sum_{j=0}^{N-1} \mathbf{F}_j T_n \left(x_j \right) + \sum_{j=1}^{N} \mathbf{F}_j T_n \left(x_j \right) \right]$$

$$= \frac{1}{\bar{c}_n N} \frac{2\mathbf{F}_o T_n(x_o)}{2} + 2 \sum_{j=1}^{N-1} \mathbf{F}_j T_n(x_j) + \frac{2\mathbf{F}_N T_n(x_N)}{2}$$

$$= \frac{2}{\bar{c}_n N} \sum_{j=0}^{N} \bar{c}_j^{-1} \mathbf{F}_j T_n(x_j)$$

Returning for consistency to the trigonometric form gives the discrete Chebyshev coefficients as

$$\widehat{\mathbf{F}}_n = \frac{2}{N\bar{c}_n} \sum_{j=0}^{N} \bar{c}_j^{-1} \mathbf{F}_j \cos\left(\frac{n\pi j}{N} \right) \qquad (32)$$

Examination of equations (31) and (32) shows that $\widehat{\mathbf{F}}_n$ can be efficiently evaluated using the fast Fourier transform (ref. 36).

Next, $\mathbf{F}$ is differentiated in equation (31) with respect to x, giving

$$\mathbf{F}'(x) = \sum_{n=1}^{N} \widehat{\mathbf{F}}_n T_n'(x) \qquad (33)$$

A form of equation (33) without derivatives of the Chebyshev polynomials is preferred, so equation (33) is rewritten in terms of another series

$$\mathbf{F}'(x) = \sum_{n=0}^{N} \widehat{\mathbf{F}}_n^{(1)} T_n(x) \qquad (34)$$

and then the coefficients of the two series are compared. The following recursion relation exists between the Chebyshev polynomials and their derivatives (ref. 28)

$$\frac{T_{n+1}'}{n+1} - \frac{T_{n-1}'}{n-1} = \frac{2}{C_n} T_n \qquad (35)$$

where

$$C_n = \begin{cases} 2 & n = 0 \\ 1 & n \geq 1 \end{cases}$$

Putting equation (35) into (34) and algebraically manipulating the resulting expression gives

$$\mathbf{F}'(x) = \sum_{n=1}^{N} \frac{C_{n-1} \widehat{\mathbf{F}}_{n-1}^{(1)}}{2n} T_n' - \sum_{n=1}^{N} \frac{\widehat{\mathbf{F}}_{n+1}^{(1)}}{2n} T_n' \qquad (36)$$

Introducing equation (33) into (36) and simplifying then results in

$$2n\widehat{\mathbf{F}}_n = C_{n-1} \widehat{\mathbf{F}}_{n-1}^{(1)} - \widehat{\mathbf{F}}_{n+1}^{(1)} \qquad (37)$$

an expression for $\widehat{\mathbf{F}}_n^{(1)}$ given $\widehat{\mathbf{F}}_n$. The procedure for finding $\widehat{\mathbf{F}}_n^{(1)}$ is initialized by setting

$$\widehat{\mathbf{F}}_{N+1}^{(1)} = 0$$

$$\widehat{\mathbf{F}}_N^{(1)} = 0$$

and then solving for $\widehat{\mathbf{F}}_{N-1}^{(1)}$ through $\widehat{\mathbf{F}}_0^{(1)}$ by back substitution (ref. 28). Then, knowing all $\widehat{\mathbf{F}}_n^{(1)}$, the required spatial derivatives of $\mathbf{F}$ can be calculated from equation (34). This procedure can again be done efficiently with the fast Fourier transform (FFT).

When the number of computational grid points to be used in a calculation is less than 60, it becomes more efficient to abandon the use of FFT's and formulate an alternative method for spectrally computing derivatives of $\mathbf{F}$. The derivative is first written discretely as

$$\mathbf{F}'(x_k) = \sum_{j=0}^{N} D_{kj} \mathbf{F}(x_j) \qquad (38)$$

where D_{kj} is a matrix (termed the Chebyshev matrix) that must be found. An interpolant of $\mathbf{F}(x)$ at any point x must then be constructed. Following reference 37, the following polynomials are chosen

$$g_j(x) = \frac{\left(1 - x^2\right) T_N'(x)(-1)^{j+1}}{\bar{c}_j N^2 (x - x_j)}$$

where $\bar{c}_j$ is defined the same as $\bar{c}_n$ on page 9. The Nth degree interpolation of $\mathbf{F}(x)$ is then given by

$$\mathbf{F}(x) = \sum_{j=0}^{N} g_j(x) \mathbf{F}(x_j)$$

To find $\mathbf{F}'(x)$, the above expression is differentiated

to give

$$\mathbf{F}'(x) = \sum_{j=0}^{N} \frac{dg_j(x)}{dx} \mathbf{F}(x_j)$$

and from equation (38)

$$D_{kj} = \frac{dg_j(x)}{dx}$$

Differentiating $g_j(x)$ results in the following relations for the Chebyshev matrix (ref. 37):

$$\left.\begin{array}{ll} D_{kj} = \dfrac{\bar{c}_k}{\bar{c}_j} \dfrac{(-1)^{j+k}}{x_k - x_j} & (j \neq k) \\[2ex] D_{jj} = -\dfrac{x_j}{2\left(1 - x_j^2\right)} & (j = k \neq 0, N) \\[2ex] D_{00} = \dfrac{2N^2 + 1}{6} = -D_{NN} \end{array}\right\} \quad (39)$$

The required derivatives of $\mathbf{F}$ can now be found by using relations (39) in equation (40). Because of the form of equation (38), this approach for computing $\mathbf{F}'$ is often termed the direct matrix method.

2.4.2 Temporal integration. Once values for $\partial \mathbf{F}/\partial x$ and $\mathbf{H}$ are determined as described above, there remains a system of ordinary differential equations in time that must be solved for the dependent variable vector $\mathbf{U}$. The equations are integrated in time using a two-stage Runge-Kutta technique. The algorithm is developed as follows.

Equation (4) is first discretized in time as noted above, giving

$$\mathbf{U}_i^{n+1} = \mathbf{U}_i^n - \Delta t \left[\left(\frac{\partial \mathbf{F}}{\partial x}\right)_{i_{sp}}^n + \mathbf{H}_i^{n+1}\right] + O(\Delta t)^2 \tag{40}$$

where n is the old time level, $n + 1$ is the new time level, and sp indicates that the spatial derivatives are computed spectrally. Note that the source term is written implicitly as previously discussed to counter the potential effects of stiffness that may be encountered in the governing equation system. The vector $\mathbf{H}^{n+1}$ is then expanded in a Taylor series in time.

$$\mathbf{H}_i^{n+1} = \mathbf{H}_i^n + \Delta t \left(\frac{\partial \mathbf{H}}{\partial t}\right)_i^n + O(\Delta t)^2$$

or

$$\mathbf{H}_i^{n+1} = \mathbf{H}_i^n + K_i^n \left(\mathbf{U}_i^{n+1} - \mathbf{U}_i^n\right) + O(\Delta t)^2 \tag{41}$$

where K_i^n is the Jacobian of $\mathbf{H}_i$, $\partial \mathbf{H}/\partial \mathbf{U}$. Putting equation (41) into (40), simplifying the resulting equation, and then rewriting in delta form gives

$$[I + \Delta t\, K_i^n]\, \Delta \mathbf{U}_i^{n+1} = -\Delta t \left[\left(\frac{\partial \mathbf{F}}{\partial x}\right)_{i_{sp}}^n + \mathbf{H}_i^n\right] \tag{42}$$

where $[I]$ is the identity matrix and $\Delta \mathbf{U}_i^{n+1} = \mathbf{U}_i^{n+1} - \mathbf{U}_i^n$. Examination of equation (42) shows that the bracketed term on the left-hand side is a block-diagonal matrix, the blocks being n by n submatrices with n the number of equations in equation (4). Since the matrix in equation (42) is diagonal, equation (42) is the most easily solved for $\Delta \mathbf{U}$ by inverting the blocks, i.e.,

$$\Delta \mathbf{U}_i^{n+1} = -\Delta t\, [I + \Delta t\, K_i^n]^{-1}\, \mathbf{R}_i^n \tag{43}$$

where $[\ ]^{-1}$ represents a block invert, and

$$\mathbf{R}_i^n = \left(\frac{\partial \mathbf{F}}{\partial x}\right)_{i_{sp}}^n + \mathbf{H}_i^n$$

is the steady-state residual vector. The two-stage Runge-Kutta technique is then applied to equation (42), yielding the following predictor-corrector formulas:

Predictor:

$$\left.\begin{array}{l} \Delta \mathbf{U}_i^{\overline{n+1}} = -\Delta t\, [I + \Delta t\, K_i^n]^{-1}\, \mathbf{R}_i^n \\[2ex] \mathbf{U}_i^{\overline{n+1}} = \mathbf{U}_i^n + \Delta \mathbf{U}_i^{\overline{n+1}} \end{array}\right\} \quad (44a)$$

Corrector:

$$\left.\begin{array}{l} \Delta \mathbf{U}_i^{n+1} = -\Delta t\, [I + \Delta t\, K_i^n]^{-1}\, \mathbf{R}_i^{\overline{n+1}} \\[2ex] \mathbf{U}_i^{n+1} = \mathbf{U}_i^n + \dfrac{1}{2}\left(\Delta \mathbf{U}_i^{\overline{n+1}} + \Delta \mathbf{U}_i^{n+1}\right) \end{array}\right\} \quad (44b)$$

Starting with initial conditions for $\mathbf{U}$, equations (44) are used to advance the solution from time level n to time level $n + 1$. The process is continued until steady-state conditions, defined as a reduction of 10 orders of magnitude in the steady-state residuals, are reached.

The magnitude of the time step in equations (44) is chosen based on the physical time scales present at any given time in the solution. The fluid-dynamic

time step Δt_f can be shown numerically to be limited by the Courant condition,

$$\Delta t_f = \frac{\Delta x}{|u| + c} \tag{45}$$

The chemical relaxation time for a species i is given by (ref. 38)

$$t_c = \frac{\rho f_i}{\dot{w}_i} \tag{46}$$

Changes in this relaxation time are then given by

$$\Delta t_c = \frac{\Delta(\rho f_i)}{\dot{w}_i} \tag{47}$$

since $\dot{w}_i$ remains nearly constant over a time step. For accuracy, it is required that the chemical time step be chosen such that no change in specific mass fraction (ρf_i) greater than 0.0001 occurs over that time step. The computational time step Δt is then chosen to be the minimum over all grid points of the fluid and chemical time step, i.e.,

$$\Delta t = \min\left(\Delta t_f, \ \Delta t_c\right) \tag{48}$$

2.5 Adams-Moulton Finite-Difference Scheme

2.5.1 Spatial discretization.
Central finite differences are chosen to define the spatial derivatives $\partial \mathbf{F}/\partial x$ in equation (4) for use with the Adams-Moulton time-stepping scheme. The spatial discretization of $\mathbf{F}$ then becomes

$$\left(\frac{\partial \mathbf{F}}{\partial x}\right)_i^n = \frac{\mathbf{F}_{i+1}^n - \mathbf{F}_{i-1}^n}{2\Delta x} + O(\Delta x)^2 \tag{49}$$

Note that the finite-difference representation of spatial derivatives is local in nature, whereas the spectral method of section 2.4 represents these derivatives globally.

2.5.2 Temporal integration.
Again knowing values for $\partial \mathbf{F}/\partial x$ and $\mathbf{H}$, the resulting system of ordinary differential equations must be integrated in time. Equation (4) is discretized in time by using the Adams-Moulton scheme (ref. 39) to yield

$$\mathbf{U}^{n+1} = \mathbf{U}^n - \Delta t \left\{ (1 - \alpha) \left[\left(\frac{\partial \mathbf{F}}{\partial x}\right)^n + \mathbf{H}^n\right] \right.$$
$$\left. + \alpha \left[\left(\frac{\partial \mathbf{F}}{\partial x}\right)^{n+1} + \mathbf{H}^{n+1}\right] \right\} + O(\Delta t)^2 \tag{50}$$

where α is the degree of implicitness. Proceeding as was done in section 2.4.2, $\mathbf{F}^{n+1}$ and $\mathbf{H}^{n+1}$ are expanded in a Taylor series in time to give

$$\mathbf{F}^{n+1} = \mathbf{F}^n + J^n \left(\mathbf{U}^{n+1} - \mathbf{U}^n\right) + O(\Delta t)^2 \tag{51}$$

$$\mathbf{H}^{n+1} = \mathbf{H}^n + K^n \left(\mathbf{U}^{n+1} - \mathbf{U}^n\right) + O(\Delta t)^2 \tag{52}$$

where J^n is the Jacobian of $\mathbf{F}$, $\partial \mathbf{F}/\partial \mathbf{U}$. Putting equations (51) and (52) into (50), simplifying the resulting equation, and rewriting in delta form then gives

$$\left[I + \alpha \, \Delta t \left(\frac{\partial J^n}{\partial x} + K^n\right)\right] \Delta \mathbf{U}^{n+1}$$
$$= -\Delta t \left[\left(\frac{\partial \mathbf{F}}{\partial x}\right)_{fd}^n + \mathbf{H}^n\right] \tag{53}$$

where again $\Delta \mathbf{U}^{n+1} = \mathbf{U}^{n+1} - \mathbf{U}^n$ and fd indicates that the spatial derivatives are computed using central finite differences. In discrete form, equation (53) becomes

$$\left[I + \alpha \, \Delta t \left(\frac{\delta J^n}{\delta x} + K^n\right)\right] \Delta \mathbf{U}_i^{n+1} = -\Delta t \, \tilde{\mathbf{R}}_i^n \tag{54}$$

where δ is a spatial central difference operator operating on J and $\Delta \mathbf{U}$, and $\tilde{\mathbf{R}}$ is the steady-state residual given by

$$\tilde{\mathbf{R}}_i^n = \frac{\mathbf{F}_{i+1}^n - \mathbf{F}_{i-1}^n}{2\,\Delta x} + \mathbf{H}_i^n \tag{55}$$

The bracketed term on the left-hand side of equation (54) is a block tridiagonal matrix. This system can be solved using the Thomas algorithm (ref. 40). To apply that algorithm, equation (54) is rewritten as

$$A_i^n \, \Delta \mathbf{U}_{i-1}^{n+1} + B_i^n \, \Delta \mathbf{U}_i^{n+1} + C_i^n \, \Delta \mathbf{U}_{i+1}^{n+1} = \mathbf{D}_i^n \tag{56}$$

where

$$A_i^n = -\frac{\alpha \, \Delta t}{2 \, \Delta x} J_{i-1}^n$$

$$B_i^n = (I + \alpha K_i^n \, \Delta t)$$

$$C_i^n = \frac{\alpha \, \Delta t}{2 \, \Delta x} J_{i+1}^n$$

$$\mathbf{D}_i^n = -\Delta t \, \mathbf{R}_i^n$$

It is then assumed that equation (56) can be written in upper triangular form as

$$\Delta \mathbf{U}_i^{n+1} = E_i^n + \mathbf{F}_i^n \, \Delta \mathbf{U}_{i-1}^{n+1} \tag{57}$$

Putting equation (57) evaluated for $\Delta \mathbf{U}_{i+1}^n$ into (56) and manipulating then gives

$$\Delta \mathbf{U}_i^{n+1} = \left(B_i^n + C_i^n F_{i+1}^n\right)^{-1} \left(\mathbf{D}_i^n - C_i^n E_{i+1}^n\right)$$
$$- \left(B_i^n + C_i^n F_{i+1}^n\right)^{-1} A_i^n \; \Delta \mathbf{U}_{i-1}^{n+1} \quad (58)$$

Comparing equation (57) with (58) then yields

$$E_i^n = \left(B_i^n + C_i^n F_{i+1}^n\right)^{-1} \left(\mathbf{D}_i^n - C_i^n E_{i+1}^n\right) \quad (59)$$

$$F_i^n = -\left(B_i^n + C_i^n F_{i+1}^n\right)^{-1} A_i^n \quad (60)$$

Once boundary conditions have been established (section 2.7), values for E_i^n and F_i^n can be found by back substitution. Then, knowing these values, $\Delta \mathbf{U}_i^{n+1}$ can be found by forward substitution from known values of $\Delta \mathbf{U}_{i-1}^{n+1}$. Starting with initial conditions for U, equation (57) is used to advance the solution from time level n to $n + 1$. The process is continued until steady-state conditions are reached.

The magnitude of the time step used to evaluate the coefficients in equation (57) is again chosen as in the spectral algorithm based on the physical time scales present in the problem. This choice is necessary to preserve the real-time accuracy of the solution. With the Adams-Moulton method, however, the time step chosen can be significantly larger than the time step based on physical time scales, since the method can be made fully implicit with proper choice of the implicitness factor α. The Adams-Moulton method is still attractive for real-time studies because of its effective damping of high-frequency components present in the solution at early times.

2.6 MacCormack Finite-Difference Scheme

2.6.1 Spatial discretization. The MacCormack finite-difference method (ref. 31) is a predictor-corrector scheme of the Lax-Wendroff type. First-order forward differences

$$\left(\frac{\partial \mathbf{F}}{\partial x}\right)_i^n = \frac{F_{i+1}^n - F_i^n}{\Delta x} \quad (61)$$

are used in the predictor step of the algorithm, and first-order backward differences

$$\left(\frac{\partial \mathbf{F}}{\partial x}\right)_i^n = \frac{F_i^n - F_{i-1}^n}{\Delta x} \quad (62)$$

are used in the corrector step. When these differences are summed in a predictor-corrector pass,

the method becomes second-order accurate in space (ref. 31). It should be noted that the method can be made nearly symmetric by alternating the spatial differencing in the predictor and corrector steps with each succeeding time step, i.e., forward differences in the predictor and backward differences in the corrector on the first time step and backward differences in the predictor and forward differences in the corrector on the second time step, etc. The symmetric algorithm is applied in this work.

2.6.2 Temporal integration. With a redefinition of the steady-state residual, the temporal integrator in the MacCormack scheme is identical to that employed with the spectral spatial discretization, equations (43) and (44), in Section 2.4.2. For the first time step, the predictor step residual is given by

$$\mathbf{R}_i^n = \frac{\mathbf{F}_{i+1}^n - \mathbf{F}_i^n}{\Delta x} + \mathbf{H}_i^n \quad (63)$$

and the corrector step residual is given by

$$\mathbf{R}_i^n = \frac{\mathbf{F}_i^n - \mathbf{F}_{i-1}^n}{\Delta x} + \mathbf{H}_i^n \quad (64)$$

For the second time step, the residual definitions are alternated, and the process is continued until steady-state conditions are achieved.

2.7 Initial and Boundary Conditions

Governing equation (4) is hyperbolic and requires initial conditions at each point to start the calculation and boundary conditions at the inflow boundary. Initial conditions are computed by first specifying an inflow Mach number and estimating an outflow Mach number. The interior Mach number distribution is then assumed to have a spatial variation that is linear. The total pressure and total temperature are assumed to be constant throughout the domain. Finally, the initial flow is assumed to be isentropic, so that isentropic relations can be used to compute the static pressure and temperature; these conditions are found from

$$\frac{T_o}{T} = 1 + \frac{\gamma - 1}{2} M^2 \quad (65)$$

$$\frac{p_o}{p} = \left(\frac{T_o}{T}\right)^{\frac{\gamma}{\gamma-1}} \quad (66)$$

Knowing the static temperature, static pressure, and Mach number, the velocity distribution can be computed, and the density distribution can be found from the equation of state. Since the inflow boundary flow remains supersonic, boundary conditions are

specified there by holding conditions fixed at their initial values.

The Adams-Moulton and MacCormack finite-difference schemes also require numerical boundary conditions at the outflow boundary. The spectral algorithm requires no such outflow boundary conditions since spatial derivatives can be defined at the outflow boundary in the same manner as is done at interior points. Outflow boundary conditions are defined for the finite-difference codes by using a second-order extrapolation formula. This formula is derived by writing a Taylor expansion to second order of the conserved variable vector $\mathbf{U}$ at the outflow boundary:

$$\mathbf{U}_N = \mathbf{U}_{N-1} + \left(\frac{\partial \mathbf{U}}{\partial x} \right)_{N-1} \Delta x_{N-1} + O(\Delta x)^2$$

In a spatially discrete form, this becomes

$$\mathbf{U}_N = \mathbf{U}_{N-1} + \frac{\mathbf{U}_{N-1} - \mathbf{U}_{N-2}}{\Delta x_{N-2}} \Delta x_{N-1} + O(\Delta x)^2$$

or

$$\mathbf{U}_N = 2\mathbf{U}_{N-1} - \mathbf{U}_{N-2} \tag{67}$$

since

$$\Delta x_{N-1} = \Delta x_{N-2}$$

Equation (67) is used directly in the MacCormack algorithm to define explicitly the numerical outflow boundary conditions. Boundary conditions are defined implicitly in the Adams-Moulton algorithm, however. To satisfy equation (67), equation (57) must be rewritten at the outflow node N to include the $N - 2$ node. This is done by introducing a new coefficient G_N^n such that

$$\Delta \mathbf{U}_N^{n+1} = E_N^n + F_N^n \, \Delta \mathbf{U}_{N-1}^{n+1} + G_N^n \, \Delta \mathbf{U}_{N-2}^{n+1} \tag{68}$$

and requiring that $E_N^n = 0$, $F_N^n = 2$, and $G_N^n = -1$. This completes the definition of all required physical and numerical boundary conditions for the algorithms.

2.8 Results

Three numerical algorithms have now been developed for solving the equations governing an inviscid chemically reacting flow; these algorithms were used to calculate the reacting flow in a rapid expansion supersonic diffuser. A rapid expansion diffuser was chosen such that high concentration gradients existed near the inflow boundary, providing a rigorous test of the methods. The comparison also allowed a demonstration of performance of the high order accurate spectral method on grids that were quite coarse compared with the grids required for equivalent accuracy using the 2 finite-difference methods. The two finite-difference codes were also compared with each other to determine their relative accuracies and efficiencies when used to compute the test problem.

The rapid expansion diffuser is shown in figure 3. The diffuser is 2 units long, has an initial cross-sectional area of 0.79 and a final cross-sectional area of 3.14. The diffuser wall is defined, as noted, by a shifted sinusoid. Flow is introduced to the diffuser at a Mach number of 1.4, a velocity of 1230 m/s, a temperature of 1900 K, and a pressure of 0.081 MPa. The chemical composition of the inflow is defined to be a three-tenths stoichiometric mixture of hydrogen fuel and air.

Starting from the initial state described above, the governing equations are solved, using the three algorithms in a time consistent manner, until steady-state conditions are reached. A comparison of the spectral and finite-difference methods, as shown by the history of the chemical species, is given in figures 4 through 6 for H_2, O_2, OH, and H_2O, respectively. Results are presented at the first grid point interior to the inflow boundary, where the flow field and species gradients are a maximum. Agreement between the Runge-Kutta spectral code and the two finite-difference calculations is excellent in all cases.

Next, spatial results from the methods are compared once steady-state conditions have been reached. The finite-difference solutions required 101 grid points before a grid independent solution, defined as a graphically imperceptible difference in the steady-state result between the present grid and next coarser grid, was attained. Calculations using the Runge-Kutta spectral code were carried out on 17- and 9-point grids. Steady-state results for the methods are given in figures 7 through 12. Figure 7 shows the axial velocity distributions in the diffuser. The 17-point spectral solution and the 101-point finite-difference solutions agree quite well throughout the diffuser. The 9-point spectral solution slightly overpredicts the velocity near the inflow boundary, but agrees well throughout the remainder of the diffuser. The overprediction is likely to be due to the failure of the coarsest spectral grid to predict adequately the high gradients that exist at the beginning of the diffuser. Temperature distributions, given in figure 8, follow similar trends, with the 17-point spectral solution agreeing well with the difference calculations, and the 9-point solution also agreeing well, except near the inflow boundary. Identical trends also occur when axial pressure distributions are compared in figure 9.

14

Axial species distributions computed by the methods are given in figures 10 through 12. Prediction of the H_2 mass fraction by the spectral method with 17 grid points agrees well with the finite-difference solution throughout the diffuser, as can be seen by examining figure 10. The 9-point spectral solution underpredicts the H_2 mass fraction near the inflow boundary, again due to the high spatial gradient in f_{H_2} there, but agreement again becomes good away from the inflow boundary. The spatial distribution of O_2 mass fraction is given in figure 11. The gradients are not as large for this species since O_2 is in excess, and both 17- and 9-point grids agree well with the finite-difference solution. The steady-state species distributions for OH and H_2O are given in figure 12. The spatial gradients are again high for both species near the inflow boundary, and trends similar to those for H_2 are repeated here. Agreement is again quite good when comparing the 17-point spectral and finite-difference results. The 9-point spectral solution still underpredicts gradients near the inflow boundary, however.

A final comparison of methods can be made in figure 13, which shows the rate of reduction of steady-state residual with iteration count for each algorithm at the first interior grid point. Since the 17-point Runge-Kutta spectral and the 101-point finite-difference calculations yield comparable accuracy and have the same minimum spatial step size, it is reasonable to assess the relative efficiency of the methods by using the results given in this figure. Note that the residual reduction rate by the spectral code is significantly greater than that provided by the finite-difference codes. The maximum residual (at any grid point) is reduced with the spectral code by 10 orders of magnitude in only 2400 iterations. The Adams-Moulton finite-difference code requires 4000 iterations to achieve the same level of residual reduction. The MacCormack finite-difference code is only able to achieve a 2- to 3-order-of-magnitude reduction in steady-state residual because of its inconsistent residual definition between predictor and correction steps. (Recall that forward spatial differences are used in the predictor, and they are alternated with backward differences in the corrector.) Even with this deficiency, however, the MacCormack method is able to achieve an acceptable level of accuracy in comparison with the Adams-Moulton and spectral schemes, as can be seen from the previous results.

To achieve a fair comparison of the three algorithms, the convergence history discussed above must be combined with the computational grid needed to achieve the required accuracy and the computational time required per time step for each scheme. The

Runge-Kutta spectral code on the 17-point grid required 644 CPU seconds to meet the established convergence requirement. The Adams-Moulton code on the 101-point grid required 1706 CPU seconds to also meet the convergence requirement. As noted before, the MacCormack code did not meet the convergence criteria, but it did achieve an acceptable level of accuracy for a steady-state solution on the 101-point grid after 4000 iterations. The code required 876 CPU seconds to reach steady-state conditions.

Based on the above results, algorithms to be extended to two-dimensional flows were chosen. The Runge-Kutta spectral method was an obvious choice because of both its high accuracy and its excellent computational efficiency. The MacCormack method was computationally more efficient than the Adams-Moulton scheme, but it was unable to achieve as high a degree of steady-state residual reduction. One other fact, not apparent in the previous calculations, must be considered in this comparison, however. The Adams-Moulton scheme resulted in a system of equations that contained block tridiagonal structure. The MacCormack scheme resulted in a system of equations that contained only block diagonal structure if the system was stiff, and no left-hand-side matrix at all if the system was not stiff. The work required to solve a block tridiagonal system varied with $3N^3$, where N is the number of equations. The work necessary to solve a block diagonal system increased with N^3, and the work to solve the system without a left-hand-side matrix increased with N. It was found in section 3 that when detailed (as opposed to global) chemistry systems were used to model supersonic reacting flows, the resulting system of equations was not temporally stiff. When the points described above were considered in this light, the MacCormack algorithm became the preferred finite-difference algorithm of those considered for extension to two-dimensional flows.

3. Multidimensional Chemically Reacting Flows

In the previous chapter, three algorithms were developed for the study of inviscid quasi-one-dimensional, supersonic, chemically reacting flow. From those algorithms, two were chosen for extension to two-dimensional, viscous, supersonic, chemically reacting flow. Those extensions are carried out in this section. Additionally, considerably more detailed chemistry and thermodynamics models are developed here for the programs. Finally, to include the effects of diffusion of momentum, energy, and mass, kinetic-theory-based diffusive transport models are developed and incorporated into the programs. Details of these models are given in the following

section. They are discussed following a statement of the general system of equations governing two-dimensional, viscous, chemically reacting flows.

3.1 Governing Equations

The two-dimensional, Navier-Stokes, energy, and species continuity equations governing multiple species undergoing chemical reaction are given by (ref. 35)

$$
\left.
\begin{aligned}
&\frac{\partial \mathbf{U}}{\partial t} + \frac{\partial \mathbf{F}(U)}{\partial x} + \frac{\partial \mathbf{G}(U)}{\partial y} = \mathbf{H} \\[10pt]
&\mathbf{U} = \left\{ \begin{array}{c} \rho \\ \rho u \\ \rho v \\ \rho E \\ \rho f_i \end{array} \right\}, \quad
\mathbf{F} = \left\{ \begin{array}{c} \rho u \\ \rho u u - \sigma_x \\ \rho u v - \tau_{yx} \\ (\rho E - \sigma_x)\, u - \tau_{xy} v + q_x \\ \rho u f_i + \rho \tilde{u}_i f_i \end{array} \right\} \\[10pt]
&\mathbf{G} = \left\{ \begin{array}{c} \rho v \\ \rho u v - \tau_{xy} \\ \rho v v - \sigma_y \\ (\rho E - \sigma_y)\, v - \tau_{yx} u + q_y \\ \rho v f_i + \rho \tilde{v}_i f_i \end{array} \right\} \\[10pt]
&\mathbf{H} = \left\{ \begin{array}{c} 0 \\ \rho \sum_i f_i b_{ix} \\ \rho \sum_i f_i b_{iy} \\ \rho \sum_i f_i \mathbf{b}_i \left(\mathbf{V} + \tilde{\mathbf{V}}_i \right) \\ \dot{w}_i \end{array} \right\}
\end{aligned}
\right\} \quad (69)
$$

$$
\sigma_x = -p + \lambda \left(\frac{\partial u}{\partial x} + \frac{\partial v}{\partial y} \right) + 2\mu \frac{\partial u}{\partial x}
$$

$$
\sigma_y = -p + \lambda \left(\frac{\partial u}{\partial x} + \frac{\partial v}{\partial y} \right) + 2\mu \frac{\partial v}{\partial y}
$$

$$
\tau_{xy} = \tau_{yx} = \mu \left(\frac{\partial u}{\partial y} + \frac{\partial v}{\partial x} \right)
$$

$$
q_x = -k \frac{\partial T}{\partial x} + \rho \sum_{i=1}^{N_s} h_i f_i \tilde{u}_i
$$

$$
+ R^o T \sum_{i=1}^{N_s} \sum_{j=1}^{N_s} \left(\frac{X_j D_{Ti}}{M_i D_{ij}} \right) (\tilde{u}_i - \tilde{u}_j)
$$

$$
q_y = -k \frac{\partial T}{\partial y} + \rho \sum_{i=1}^{N_s} h_i f_i \tilde{v}_i
$$

$$
+ R^o T \sum_{i=1}^{N_s} \sum_{j=1}^{N_s} \left(\frac{X_j D_{Ti}}{M_i D_{ij}} \right) (\tilde{v}_i - \tilde{v}_j)
$$

$$
E = \sum_{i=1}^{N_s} h_i f_i - \frac{p}{\rho} + \frac{u^2 + v^2}{2} \qquad (70)
$$

$$
h_i = h_i^o + \int_{T_R}^{T} c_{p_i}\, dT \qquad (71)
$$

$$
p = \rho R^o T \sum_{i=1}^{N_s} f_i / M_i \qquad (72)
$$

The diffusion velocities are found by solving (ref. 35)

$$
\nabla X_i = \sum_{j=1}^{N_s} \left(\frac{X_i X_j}{D_{ij}} \right) \left(\tilde{\mathbf{V}}_j - \tilde{\mathbf{V}}_i \right) + (f_i - X_i) \left(\frac{\nabla p}{p} \right)
$$

$$
+ \left(\frac{\rho}{p} \right) \sum_{j=1}^{N_s} f_i f_j \left(\mathbf{b}_i - \mathbf{b}_j \right)
$$

$$
+ \sum_{j=1}^{N_s} \left(\frac{X_i X_j}{\rho D_{ij}} \right) \left(\frac{D_{Tj}}{f_j} - \frac{D_{Ti}}{f_i} \right) \left(\frac{\nabla T}{T} \right) \qquad (73)
$$

Note that if there are N_s chemical species, then $i = 1, 2, \ldots, (N_s - 1)$ and $(N_s - 1)$ equations must be solved for the species f_i. The final species mass fraction f_{N_s} can then be found by conservation of mass since

$$
\sum_{i=1}^{N_s} f_i = 1
$$

3.2 Thermodynamics Model

To calculate the required thermodynamic quantities, the specific heat for each species is first defined by a fourth-order polynomial in temperature:

$$
\frac{c_{p_i}}{R} = A_i + B_i T + C_i T^2 + D_i T^3 + E_i T^4 \qquad (74)
$$

The coefficients are found by a curve fit of the data tabulated in reference 33. Knowing the specific heat of each species, the enthalpy of each species can then be found from equation (71), and the total internal energy is computed from equation (70).

To determine the equilibrium constant (required in section 3.3) for each chemical reaction being considered, the Gibbs energy of each species must first be found. For a constant pressure process, c_p / R_T from equation (74) is first integrated over temperature to define the entropy of the species, and the resulting expression is integrated again over temperature to obtain the following fifth-order polynomial

in temperature for the Gibbs energy of each species:

$$\frac{g_i}{R} = A_i(T - T\ln T) - \frac{B_i}{2}T^2 - \frac{C_i}{6}T^3 - \frac{D_i}{12}T^4 - \frac{E_i}{20}T^5 + F_i - G_i T \tag{75}$$

Coefficients F_i and G_i are again defined in reference 33. The Gibbs energy of reaction can then be calculated as the difference between the Gibbs energy of product species and reactant species.

$$\Delta G_R = \sum_{i=\text{products}} n_i \,\Delta g_i - \sum_{i=\text{reactants}} n_i \,\Delta g_i \tag{76}$$

The equilibrium constant for each reaction is then found from (ref. 41)

$$K = \left(\frac{1}{R^{o'}T}\right)^{\Delta n} \exp\left(-\frac{\Delta G_R}{R^o T}\right) \tag{77}$$

where Δn is the change in the number of moles when going from reactants to products.

3.3 Chemistry Model

In the present work, the finite-rate chemical reaction of gaseous hydrogen fuel and air is of concern. That reaction is modeled by a 9-species, 18-reaction model described in table I (ref. 42). Eight of the chemical species (H_2, O_2, H_2O, OH, H, O, HO_2, H_2O_2) are active, and the ninth (N_2) is assumed inert. The forward rate of each reaction j is given by the modified Arrhenius law

$$k_{f_j} = A_j T_j^N \exp\left(-\frac{E_j}{R^o T}\right) \tag{78}$$

Values for A, N, and E are also given in table I. Knowing the forward rate, and using the equilibrium constant determined in the previous section, the backward rate can be defined by

$$k_{b_j} = k_{f_j}/K_j \tag{79}$$

Once the forward and reverse reaction rates have been determined, the production rates of the eight species can be found from the law of mass action. For the general chemical reaction
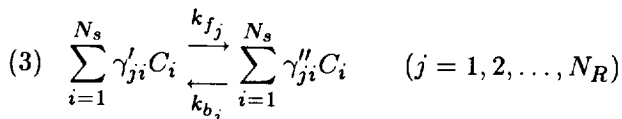
$$(3) \quad \sum_{i=1}^{N_s} \gamma'_{ji} C_i \underset{k_{b_j}}{\overset{k_{f_j}}{\rightleftarrows}} \sum_{i=1}^{N_s} \gamma''_{ji} C_i \qquad (j = 1, 2, \ldots, N_R)$$

the law of mass action states that the rate of change of concentration of species i by reaction j is given by (ref. 35)

$$\left(\dot{C}_i\right)_j = \left(\gamma''_{ji} - \gamma'_{ji}\right)\left(k_{f_j}\prod_{i=1}^{N_s} C_i^{\gamma'_{ji}} - k_{b_j}\prod_{i=1}^{N_s} C_i^{\gamma''_{ji}}\right) \tag{80}$$

All third-body efficiencies are assumed to be equal to 1.0. The net rate of change in concentration of species i by reaction j is then found by summing the contributions from each reaction,

$$\dot{C}_i = \sum_{j=1}^{N_R} \left(\dot{C}_i\right)_j \tag{81}$$

Finally, the production of species i can be found from

$$\dot{w}_i = \dot{C}_i M_i \tag{82}$$

The source terms for the last i equations in (69) are now determined as a function of the dependent variables.

3.4 Diffusion Models

Models for the coefficients governing the diffusion of momentum, energy, and mass are now determined. The individual species viscosities are computed from Sutherland's law,

$$\frac{\mu}{\mu_o} = \left(\frac{T}{T_o}\right)^{3/2} \frac{T_o + S}{T + S} \tag{83}$$

where μ_o and T_o are reference values and S is the Sutherland constant. All three values are tabulated for the species in references 43 and 44. Once the viscosity of each species has been determined, the mixture viscosity is determined from Wilke's law (ref. 45),

$$\mu_m = \sum_{i=1}^{N_s} \frac{\mu_i}{1 + \frac{1}{X_i}\sum_{\substack{j=1 \\ j\neq i}}^{N_s} X_j \phi_{ij}} \tag{84}$$

where

$$\phi_{ij} = \frac{\left\{1 + \left[(\mu_i/\mu_j)\,(\rho_j/\rho_i)\right]^{1/2}\,(M_i/M_j)^{1/4}\right\}^2}{\left(\frac{4}{\sqrt{2}}\right)\left[1 + (M_i/M_j)\right]^{1/2}} \tag{85}$$

The species thermal conductivities are also computed from Sutherland's law,

$$\frac{k}{k_o} = \left(\frac{T}{T_o'}\right)^{3/2} \frac{T_o' + S'}{T + S'} \qquad (86)$$

but with different values of the reference values k_o and T_o', and the Sutherland's constant S'. These values are also taken from references 43 and 44. The mixture thermal conductivity is computed by using conductivity values for the individual species and Wassiljewa's formula (ref. 46),

$$k_m = \sum_{i=1}^{N_s} \frac{k_i}{1 + \frac{1}{X_i} \sum_{\substack{j=1 \\ j \neq i}}^{N_s} X_j \phi_{ij}'} \qquad (87)$$

where $\phi_{ij}' = 1.065\phi_{ij}$, and ϕ_{ij} is taken from equation (85).

For dilute gases, Chapman and Cowling used kinetic theory to derive the following expression for the binary diffusion coefficient D_{ij} between species i and j (ref. 43):

$$D_{ij} = \frac{0.001858 T^{3/2} \left[(M_i + M_j)/M_i M_j\right]^{1/2}}{p\sigma_{ij}^2 \Omega_D} \qquad (88)$$

Here, the diffusion collision integral Ω_D is approximated by

$$\Omega_D = T^{*-0.145} + (T^* + 0.5)^{-2} \qquad (89)$$

where

$$T^* = T/T_{\epsilon_{ij}}$$

Values of the effective temperature T_ϵ and effective collision diameter σ are taken to be averages of the separate molecular properties of each species, giving (ref. 43)

$$\sigma_{ij} = \frac{1}{2}(\sigma_i + \sigma_j) \qquad (90)$$

and

$$T_{\epsilon_{ij}} = \left(T_{\epsilon_i} T_{\epsilon_j}\right)^{1/2} \qquad (91)$$

Once the binary diffusion coefficients for all species combinations are known, the diffusion velocities of each species can be computed from equation (73). The diffusion velocity of each species is the species velocity due to all diffusion processes algebraically added to the convection velocity. When computing the diffusion velocities, it is assumed as

suggested in reference 35, that the thermal diffusion coefficient D_T is negligible compared with the binary diffusion coefficient. The solution of equation (73) requires solving a simultaneous equation system, with the number of equations equivalent to the number of species present for each component of the diffusion velocity. It should be noted that for i species, however, the system of i equations defined by equation (5) is not linearly independent. One of the equations must be replaced by the constraint

$$\sum_{i=1}^{N_s} \rho f_i \widetilde{\mathbf{V}}_i = 0 \qquad (92)$$

to make the system linearly independent. The resulting system of equations is solved for the diffusion velocities by using the Householder method (refs. 47 and 48).

3.5 Solution of the Governing Equations

Once the thermodynamic properties, diffusion coefficients, and chemical production rates have been defined, the governing equations can be solved numerically. The finite-difference solution procedure is discussed in the next section, 3.5.1, and this discussion is followed by the development of the spectral solution scheme, described in section 3.5.2.

3.5.1 Finite-difference solution method.

To solve the governing equations (69) with the finite-difference scheme, the equations must first be transformed from the physical domain (x, y) in which they are written to an appropriate computational domain (ξ, η). The equations are solved on a coordinate grid that is highly compressed in both x and y in the physical domain near regions where high gradients exist. The grid is required to be uniform, however, in the computational domain to most readily maintain a required order of accuracy.

To transform the governing equations from the physical to the computational domain, fluxes $\mathbf{F}$ and $\mathbf{G}$ are first written in functional form and differentiated with respect to the computational coordinates. Therefore, given $\mathbf{F} = \mathbf{F}(x, y)$ and $\mathbf{G} = \mathbf{G}(x, y)$, and proceeding first with $\mathbf{F}$,

$$\mathbf{F}_\xi = \mathbf{F}_x x_\xi + \mathbf{F}_y y_\xi \qquad (93)$$

$$\mathbf{F}_\eta = \mathbf{F}_x x_\eta + \mathbf{F}_y y_\eta \qquad (94)$$

Then, substituting $\mathbf{F}_y$ from equation (94) into equation (93) and simplifying gives

$$\mathbf{F}_x = \frac{\mathbf{F}_\xi y_\eta - \mathbf{F}_\eta y_\xi}{J} \qquad (95)$$

where

$$J = x_\xi y_\eta - y_\xi x_\eta \tag{96}$$

is the Jacobian of the transformation. Proceeding in like manner for G gives

$$\mathbf{G}_y = \frac{\mathbf{G}_\eta x_\xi - \mathbf{G}_\xi x_\eta}{J} \tag{97}$$

Finally, substituting equations (95) and (97) into equations (69) gives the governing equations in the computational domain

$$\frac{\partial \widehat{\mathbf{U}}}{\partial t} + \frac{\partial \widehat{\mathbf{F}}}{\partial \xi} + \frac{\partial \widehat{\mathbf{G}}}{\partial \eta} = \widehat{\mathbf{H}} \tag{98}$$

where

$$\widehat{\mathbf{U}} = J\mathbf{U}, \qquad \widehat{\mathbf{H}} = J\mathbf{H}$$

$$\widehat{\mathbf{F}} = y_\eta \mathbf{F} - x_\eta \mathbf{G}$$

$$\widehat{\mathbf{G}} = x_\xi \mathbf{G} - y_\xi \mathbf{F}$$

Here $(x_\xi, x_\eta, y_\xi, y_\eta)$ are the transformation metrics that form the inverse Jacobian matrix, and J is the Jacobian of the transformation. The metrics can be computed numerically once the physical coordinate grid has been prescribed.

To resolve large flow field and concentration gradients, the physical coordinate grid must be chosen sufficiently fine in those regions. For the mixing layer problems to be studied in this work, the grid must be highly refined in a direction transversely across the layer. Large streamwise gradients may also occur with movement along the layer, and grid refinement must also be allowed at those locations. The compression function of Thomas et al. (ref. 49) can be used to satisfy the refinement requirements in both the transverse direction and the streamwise direction. The compression function in the transverse direction is given by

$$\bar{\eta} = \eta_o \left[\frac{\sinh\left(\beta_y \eta - A_\eta\right)}{\sinh A_\eta} + 1 \right] \tag{99}$$

$$0 \le \eta \le 1$$

$$0 \le \bar{\eta} \le 1$$

where

$$A_\eta = \frac{1}{2}\ln \left[\frac{1 + \left(e^{\beta_y} - 1\right)\eta_o}{1 + \left(e^{-\beta_y} - 1\right)\eta_o} \right]$$

The degree of transverse compression is determined by β_y, and η_o is the value of η at which maximum compression occurs, i.e., the center of the mixing layer. The compression function in the streamwise direction is given by

$$\bar{\xi} = \xi_o \left[\frac{\sinh\left(\beta_x \xi - A_\xi\right)}{\sinh A_\xi} + 1 \right] \tag{100}$$

$$0 \le \xi \le 1$$

$$0 \le \bar{\xi} \le 1$$

where

$$A_\xi = \frac{1}{2}\ln \left[\frac{1 + \left(e^{\beta_x} - 1\right)\xi_o}{1 + \left(e^{-\beta_x} - 1\right)\xi_o} \right]$$

The degree of streamwise compression is determined by β_x, and ξ_o is the value of ξ at which maximum compression occurs.

Having now determined the nondimensional physical domain $(\bar{\xi}, \bar{\eta})$ from the computational domain (ξ, η) by using equations (99) and (100), $(\bar{\xi}, \bar{\eta})$ is then mapped onto the physical domain (x, y) by using the algebraic-numerical coordinate transformation of Smith and Weigel (ref. 50). This transformation is given by

$$x = X_2(\bar{\xi})\bar{\eta}(\eta) + X_1(\bar{\xi})[1 - \bar{\eta}(\eta)] \tag{101}$$

$$y = Y_2(\bar{\xi})\bar{\eta}(\eta) + Y_1(\bar{\xi})[1 - \bar{\eta}(\eta)] \tag{102}$$

where (X_1, Y_1) are the boundary points at $y = 0$, and (X_2, Y_2) are the boundary points at $y = y_{\max}$. The generality afforded by equation (101) that allows transverse coordinate lines to be skewed is not needed in this work. Therefore, X_1 is chosen equal to X_2 and equation (101) simplifies to

$$x = \bar{\xi} x_{\max} \tag{103}$$

where $\bar{\xi}$ is found from equation (100). The transformation metrics $(x_\xi, x_\eta, y_\xi, y_\eta)$ are then found by directly differentiating equations (102) and (103). Inverse metrics $(\xi_x, \xi_y, \eta_x, \eta_y)$ required for differentiating terms within the flux vectors are then found by inverting the inverse Jacobian matrix, i.e.,

$$\begin{bmatrix} \xi_x & \eta_x \\ \xi_y & \eta_y \end{bmatrix} = \begin{bmatrix} x_\xi & y_\xi \\ x_\eta & y_\eta \end{bmatrix}^{-1} = \frac{\begin{bmatrix} y_\eta & -y_\xi \\ -x_\eta & x_\xi \end{bmatrix}}{J} \tag{104}$$

to form the Jacobian matrix of the transformation.

It is sometimes advantageous to allow refinement of the physical grid in a point-by-point fashion. That option can be quite valuable for defining the streamwise grid in the present work, and so such an option is provided by way of a simple modification of equations (102) and (103). Rather than defining X_1 and

X_2 with equation (100), the boundary points are defined manually in point-by-point fashion. Care must be taken that changes between successive points, Δx, are not too great or discretization errors can be introduced. Having defined the distribution of X_1 and X_2, the corresponding values of Y_1 and Y_2, and $\bar{\eta}$ from equation (99), the required transformation metrics can be found by numerically differentiating equations (102) and (103) with respect to ξ and η. Once the choice for streamwise grid definition is made, all quantities required to describe the physical and computational domains are defined by equations (99) through (104).

As noted in section 2, the governing equation system (69) can be stiff because of the kinetic source terms contained in the vector **H** and because of diffusive terms in the vectors **F** and **G**. Only the kinetic terms introduce stiffness in this work; spatial stiffness is controlled by the choice of grid. To deal with the stiff system, the approach used in references 23 through 26 is again followed, and the kinetic source terms are computed implicitly. In a temporally discrete form, equation (69) then becomes

$$\widehat{U}^{n+1} = \widehat{U}^n - \Delta t \left[\left(\frac{\partial \widehat{F}}{\partial \xi} \right)^n + \left(\frac{\partial \widehat{G}}{\partial \eta} \right)^n - \widehat{H}^{n+1} \right]$$
(105)

Following the approach used in section 2.4.2, **H** is linearized by expanding it in a Taylor series in time. Introducing this expression into equation (105), simplifying, and rewriting in delta form then gives

$$[I - \Delta t \, K^n] \, \Delta \widehat{U}^{n+1} = -\Delta t \, \widehat{R}^n$$
(106)

where

$$\widehat{R}^n = \left(\frac{\partial \widehat{F}}{\partial \xi} \right)^n + \left(\frac{\partial \widehat{G}}{\partial \eta} \right)^n - \widehat{H}^n$$
(107)

is the steady-state residual, I is the identity matrix, K^n is the Jacobian of **H** with respect to **U**, $(\partial H / \partial U)$, and $\Delta U^{n+1} = U^{n+1} - U^n$.

Once the temporal discretization used to construct equation (106) has been performed, the resulting system is spatially differenced by following the approach of section 2.6 and using the unsplit MacCormack predictor-corrector scheme (ref. 31). This results in a spatially and temporally discrete, simultaneous system of equations at each grid point (refs. 23 and 24). Each simultaneous system is solved with the earlier noted Householder technique in combination with the MacCormack technique, which is then used to advance the equations in time. The

modified MacCormack technique then becomes

$$[I - \Delta t \, K_{ij}^n] \, \Delta U_{ij}^{\overrightarrow{n+1}} = -\Delta t \, \overrightarrow{R}_{ij}^n$$
(108)

$$U_{ij}^{\overrightarrow{n+1}} = U_{ij}^n + \Delta U_{ij}^{\overrightarrow{n+1}}$$

$$\left[I - \Delta t \, K_{ij}^{\overleftarrow{n+1}} \right] \Delta U_{ij}^{n+1} = -\Delta t \, \overleftarrow{R}^{\overleftarrow{n+1}}$$
(109)

$$U_{ij}^{n+1} = U^n + 0.5 \left(\Delta U^{\overrightarrow{n+1}} + \Delta U^{n+1} \right)$$

where $\overrightarrow{R}$ represents a forward spatial difference of R and $\overleftarrow{R}$ a backward spatial difference. Stress terms are differenced in the conventional manner (ref. 31). Equations (108) and (109) are used to advance the solution from time n to time $n + 1$ and this process is continued until a desired integration time has been reached.

The magnitude of the time step in equations (108) and (109) is again chosen based on the physical time scales present at any given time in the solution. These scales are defined in section 2.4.2; they are repeated here for convenience. The fluid-dynamic time step Δt_f can be shown to be limited by the Courant or viscous stability limit of the governing equation (ref. 31). The chemical relaxation time for a species i is given by (ref. 38)

$$t_c = \frac{\rho f_i}{\dot{w}_i}$$

Changes in this relaxation time are then given by

$$\Delta t_c = \frac{\Delta(\rho f_i)}{\dot{w}_i}$$

since $\dot{w}_i$ remains nearly constant over a time step. For accuracy, it is required that the chemical time step be chosen such that no change in mass fraction greater than 0.01 occurs over that time step. The computational time step Δt is then chosen to be the minimum over all grid points of the fluid and chemical time steps.

3.5.2 Hybrid Chebyshev spectral solution method.
A hybrid Chebyshev spectral method has also been used to solve the governing equations (69) in this work. The spectral method, as discussed in section 2, is attractive for studies of reacting mixing layers because it yields high numerical accuracy on relatively coarse grids. A highly accurate method is necessary for proper resolution of the large transverse gradients that exist across the mixing layer. Gradients are not as large, however, in the streamwise direction of the mixing layer. A lower order method appeared

adequate in that direction. With these requirements in mind, it was decided that transverse derivatives across the mixing layer should be computed spectrally, whereas finite differences were deemed appropriate in the streamwise direction.

Spatial derivatives in the transverse direction were computed spectrally by using the direct Chebyshev matrix method developed in section 2.4.1. Required derivatives of the flux vector $\widehat{\mathbf{G}}'_k$ were computed at each grid point, given the distribution of the function $\widehat{\mathbf{G}}_j$ along the complete column of points which included point k, i.e.,

$$\widehat{\mathbf{G}}'_k(y_j) = \sum_{j=0}^{N} D_{kj}\widehat{\mathbf{G}}(y_j) \qquad (110)$$

where

$$D_{kj} = \frac{\bar{c}_k}{\bar{c}_j}\frac{(-1)^{j+k}}{y_k - y_j} \qquad (j \neq k)$$

$$D_{jj} = -\frac{y_j}{2(1 - y_j^2)} \qquad (j = k \neq 0,\ N)$$

$$D_{00} = \frac{2N^2 + 1}{6} = -D_{NN}$$

Streamwise spatial derivatives were again computed with the MacCormack finite-difference technique as applied in the previous section, 3.5.1.

The governing equations must again be transformed from the physical (x, y) to the computational (ξ, η) domain, and the procedure described in equations (93) through (98) is again employed. The streamwise compression function, equation (100), and the streamwise transformation, equation (103), are still equally valid, and they are retained. The streamwise grid can optionally be obtained in point-by-point fashion as before. The transformation in the transverse (spectral) direction must still be capable of refining the grid at the center of the mixing layer. A different transformation is used, however, to preserve spectral accuracy when forming the transverse derivatives. Boyd (ref. 51) found that exponential mappings, such as the mapping employed in equation (99), gave poor performance. Calculations with alternate mapping functions indicated that, in general, the mapping function should decay more slowly than a function best describing the solution being sought. Recognizing the general form of the resulting mixing layer solution, an algebraic mapping function suggested by Boyd (ref. 51) was chosen and

employed. That function is given by

$$y = \frac{\beta_y \eta}{1 - \eta^2} \qquad (111)$$

which maps the Chebyshev computational domain [-1,1] onto the physical domain $[-\infty, \infty]$. Maximum grid refinement occurs at $y = 0$, and the grid is chosen so that the mixing layer lies near this coordinate location. The function β_y determines the degree of grid refinement. Equations (103) and (111) therefore complete the transformation from the computational to the physical domain. Elements of the inverse Jacobian matrix are again determined by directly differentiating equations (103) and (111), and the Jacobian matrix is found by using equation (104).

Having now defined the transformation required for the spectral method, the spatial derivatives are discretized as described earlier in this section. Once the spatial terms are differenced, there again remains a system of ordinary differential equations at each grid point to be integrated in time. Once the steady-state residual $\widehat{\mathbf{R}}_i^n$ is redefined to reflect the change to spectral transverse derivatives, the procedure for temporally integrating the equations is identical to that carried out in equations (105) through (109). Introducing the new residual definition into equations (108) and (109), the hybrid spectral algorithm is given by

$$\left[I - \Delta t\, K_{ij}^n\right]\Delta\widehat{\mathbf{U}}_{ij}^{\overline{n+1}} = -\Delta t\left[\left(\frac{\partial\widehat{\mathbf{F}}}{\partial\xi}\right)_{ij}^n \left.\right.\right.$$
$$\left. + \left(\frac{\partial\widehat{\mathbf{G}}}{\partial\eta}\right)_{ij_{sp}}^n - \widehat{\mathbf{H}}_{ij}^n\right]$$
$$\widehat{\mathbf{U}}_{ij}^{\overline{n+1}} = \widehat{\mathbf{U}}_{ij}^n + \Delta\widehat{\mathbf{U}}_{ij}^{\overline{n+1}} \qquad (112)$$

$$\left[I - \Delta t\, K_{ij}^{\overline{n+1}}\right]\Delta\widehat{\mathbf{U}}_{ij}^{n+1} = -\Delta t\left[\left(\frac{\partial\widehat{\mathbf{F}}}{\partial\xi}\right)_{ij}^{\overline{n+1}} \left.\right.\right.$$
$$\left. + \left(\frac{\partial\widehat{\mathbf{G}}}{\partial\eta}\right)_{ij_{sp}}^{\overline{n+1}} - \widehat{\mathbf{H}}_{ij}^{\overline{n+1}}\right]$$
$$\widehat{\mathbf{U}}_{ij}^{n+1} = \widehat{\mathbf{U}}_{ij}^n + 0.5\left[\Delta\widehat{\mathbf{U}}_{ij}^{\overline{n+1}} + \Delta\widehat{\mathbf{U}}_{ij}^{n+1}\right]$$
$$(113)$$

where sp indicates that the derivative is to be evaluated spectrally. The time step Δt is again chosen by following the procedure described in section 3.5.1.

3.5.3 Boundary and initial conditions. The governing equations (69) require boundary conditions along

21

all four boundaries. For the problems to be considered, the inflow boundary is always supersonic, so the velocities, static temperature and pressure, and species are specified and fixed there. The upper and lower boundaries always lie in the free stream, and therefore either the normal gradient of the preceding variables is required to vanish or the free-stream conditions are enforced along those boundaries. The gradient conditions not only satisfy the free-stream conditions, but also provide nonreflective conditions that pass disturbances through the boundary rather than reflect them back to the domain. The outflow boundary is also supersonic, and values of the velocities, static temperature and pressure, and species are determined by extrapolation from upstream values. Finally, no slip boundary conditions ($u = 0$, $v = 0$) are used to specify velocity components along solid surfaces that occur in the physical domain. Additionally, along these solid boundaries, adiabatic conditions ($\partial T/\partial y = 0$) are assumed, the boundary-layer assumption on pressure ($\partial p/\partial y = 0$) is chosen, and the walls are assumed to be noncatalytic ($\partial f_i/\partial y = 0$).

The governing equations (69) also require a set of initial conditions. The equations are initialized by setting values of the velocities, static temperature and pressure, and species throughout the domain to the values chosen initially for boundary conditions at the inflow boundary. Having specified all required initial and boundary data, the equation is marched in time from the initial time to some final specified integration time.

A general model for chemically reacting flow has now been developed, and the resulting governing equations have been defined in this section. Further, two numerical methods for solving these governing equations have been developed. In the following section, the governing equations are solved for several supersonic chemically reacting mixing layer cases, and the results are then discussed in light of the observations given in section 1 for such flows.

4. Simulations of Reacting Mixing Layers

By using the theory and solution procedure developed in section 3, the chemically reacting flow field in a non-premixed laminar, supersonic, spatially developing mixing layer is numerically simulated in this section. Two basic mixing layer cases are considered. The first of those cases involves a hydrogen-air mixing layer with fuel and oxidant initially separated by a finite-thickness splitter plate. The second case considers a hydrogen-air mixing layer that has just begun to develop downstream of a splitter plate. The

plate is not included in this calculation; the effects of the plate on the flow are retained, however. The first case is computed with only the finite-difference algorithm, and the results from that analysis are discussed in the following section. The second case is computed with the hybrid spectral algorithm. Results from that analysis are discussed in section 4.2.

4.1 Simulations Using the Finite-Difference Algorithm

The finite-difference algorithm has been applied to a non-premixed, spatially developing, laminar, supersonic, chemically reacting mixing layer. The configuration that is considered is described schematically in figure 14. The overall domain is 5 cm high and 5 cm long. The height chosen places the boundaries well into the free stream, and the length allows initial development of the mixing layer. Initially, hydrogen fuel and air are separated by a 0.5-cm-long splitter plate that is 0.02 cm thick and centered at $y = 2.5$ cm. Downstream of the plate, the fuel and air mix and ignition occurs at some further distance downstream of the plate base. From that point, chemical reaction between the fuel and air takes place. For the problem being considered, cold gaseous hydrogen is introduced above the plate at Mach 1.5, a Reynolds number of 3700 based on plate thickness, a temperature of 293 K, and a pressure of 0.101 MPa (1 atm). Hot air is introduced below the plate at Mach 1.5, a Reynolds number of 731, a temperature of 2000 K, and a pressure of 0.101 MPa. These conditions result in an initial hydrogen velocity of 1953 m/s and an air velocity of 1297 m/s; this yields a hydrogen-to-air velocity ratio of 1.5.

By using the configuration and conditions described above, the mixing-layer flow field is marched in time from the specified initial conditions to the conditions existing at 0.1 ms. The solution is obtained on a spatial grid with 219 nodes in the streamwise direction and 51 nodes in the transverse direction. The grid is compressed in x near the trailing edge of the plate and highly compressed in y in the region of the mixing layer. The resulting flow field is described in figures 15 through 35, which give pictures of the flow at an instant in time. Figure 15 shows a velocity vector field plot of the flow close to and on either side of the splitter plate and the developing mixing layer downstream of the base of the splitter plate. (Velocity vectors are shown for only every four streamwise and transverse grid points in this region.) Expansions of both streams through Prandtl-Meyer fans can be observed at the trailing edge of the plate. The higher velocity hydrogen stream and the lower velocity airstream are apparent as is the wake flow downstream of the plate. The

development of the mixing layer with streamwise distance can also be seen. Two regions of instability are also apparent in figure 15. The first region lies just downstream of the splitter plate approximately 1.0 cm beyond the initial station. The second region lies well downstream at approximately 4.0 cm from inflow. The flow is relatively quiescent between these two regions.

These instabilities can also be observed in figure 16(a), which shows a plot of streamwise velocity versus streamwise coordinate at several constant transverse stations that are well within the mixing layer. The oscillations are present along all three lines of constant y and are quite close in phase and magnitude, indicating that the instability is present in similar fashion across the layer. The oscillatory behavior of the layer is quite typical of that seen numerically and experimentally in nonreacting layers and, at least in part, appears to be produced by a Kelvin-Helmholtz instability. To determine whether the instabilities and their locations were functions of time, several other times in the evolution of the layer are examined. These results are given in figures 16(b), 16(c), and 16(d) for times of 0.09, 0.06, and 0.02 ms, respectively, beyond initiation of the flow. The instability near the splitter plate is present at all times that are given in the figures. The size of the region and the amplitude of the instability do not change with time. The location of the waves does change with time, however. At the latest time plotted the waves propagate downstream with increasing time, amplifying between $x = 0.6$ and 1.2 cm and damping beyond that streamwise station. The disturbance has essentially dissipated at 0.1 ms beyond 2.1 cm. At earlier times, however, the upstream instability propagates further downstream, reaching as can be seen in figure 16(d) the initiation of the second instability. With increasing time, though, the initial disturbance damps, and the central region of the flow between $x = 2.1$ and 2.8 cm becomes relatively quiescent.

The initial velocity increase at $x = 0.5$ cm is also present at all times and is due to the expansion of hydrogen and air off the trailing edge of the splitter plate. The velocity decrease that follows results from each gas being compressed by a recompression shock that turns the fluids to a nearly streamwise direction. In this region, in the wake of the plate just downstream of the splitter plate, the flow also separates. A recirculation bubble then forms and remains throughout the calculation. (The presence of the recirculating region can be seen in fig. 17; that is discussed later.) This separation is not stable with time; rather, it changes shape and position slightly with increasing time and acts as a destabilizing mechanism for the flow in the wake downstream of the sep-

aration. Changes in the position of the separation also cause the recompression shock to change position with time. The oscillatory motion with time of both the separation bubble and the recompression shock thus appears to be the genesis of the first instability. It should be noted, however, that although the separation and recompression shocks appear to be the tripping mechanism for the first instability, the numerical method being employed suffers to some degree from Gibbs oscillations in the immediate neighborhood of the shock. These numerical oscillations may also contribute to the initiation of the instability.

The second instability is also present at all times shown in figures 16(a) through (d). Initially (fig. 16(d)), this region is influenced by the upstream disturbance. With increasing time, however, the region preceding this instability becomes stable as can be seen by viewing figures 16(c), (b), and (a). It appears that the second region of instability represents the onset of transition in the mixing layer. The amplitude of the disturbance grows with increasing distance downstream from the 2.8-cm station. There is also some growth in amplitude with time at any given streamwise station within the region of the instability.

To examine the contribution to instability from heat release due to chemical reaction, the identical flow field is computed without reaction. Those results are given for two times, 0.1 ms and 0.02 ms, in figures 16(e) and (f), respectively. By comparing figures 16(e) and (f) with 16(a) and (d), it can be seen that both instabilities still remain without heat release. The upstream disturbance, in fact, appears essentially unaffected by reaction. The effect of heat release on the downstream disturbance also appears quite mild at early times (figs. 16(d) and (f)), but there is a marked effect at 0.1 ms, as can be seen by comparing figures 16(a) and (e). The amplitude of the disturbance is consistently greater without chemical reaction. This result is consistent with the findings of references 15 and 20 for subsonic flow, which showed mixing is retarded by heat addition.

Another view of the streamwise development of the velocity field is given in figure 17, which shows u profiles as a function of the y coordinate at four ($x = 0.51$, 1.0, 3.0, and 5.0 cm) streamwise stations. The initial profile shows that there is a recirculation region with negative streamwise velocities near the trailing edge of the splitter plate. A velocity defect in the wake continues to exist downstream at the 1.0- and 3.0-cm stations. A developed mixing layer profile is apparent once the 5.0-cm station is reached. An overall view of the streamwise velocity is given by using a contour plot in figure 18. The regions

of instability and the development of the mixing layer are consistent with figures 16 and 17, but they can be viewed in a more realistic sense when shown in two dimensions. The velocity contours are compared with two-dimensional contours of other primitive variables later in this discussion.

A plot of static temperature versus streamwise coordinate for several constant transverse stations is given in figure 19. The y coordinates are identical to those given in figure 16. The instabilities present in the velocity plots of figure 16 are consistent in location with those of the temperature field. The amplitudes of the oscillations in temperature are greater, however, because of a significantly greater temperature difference between hydrogen fuel (293 K) and air (2000 K) as compared with the velocity difference between the fuel stream and airstream. The first disturbance is significantly more pronounced along the $y = 2.5$ cm coordinate line where cold fuel and hot air are initially in contact as compared with the $y = 2.46$ cm and $y = 2.54$ cm lines where no mixing occurs. The second disturbance is markedly more pronounced along the $y = 2.46$ cm and $y = 2.5$ cm coordinate lines as compared with the $y = 2.54$ cm line, indicating that thermal mixing is occurring mainly below the location of the splitter plate at $y = 2.5$ cm.

A plot of temperature profiles versus the transverse coordinate at four streamwise stations ($x = 0.51, 1.0, 3.0,$ and 5.0 cm) is given in figure 20. These stations are the same as those used in figure 17. The development of the temperature profile with increasing streamwise distance can be seen in the figure. Initially ($x = 0.51$ cm) there is some cooling in the base region beyond the plate because of expansion of the fuel and air off the plate and because of the endothermic reactions associated with ignition early in the development of the layer. Well downstream at $x = 5.0$ cm, the temperature profile is well developed, and there are temperature increases on either edge of the layer associated with the exothermic reactions that are taking place.

By comparing figures 20 and 17, it can be seen that the temperature profiles at each x-station are consistently broader than the streamwise velocity profiles. This is also apparent by comparing the plot of temperature contours in figure 21 with the velocity contours given in figure 18. This result is consistent with the discussion and experimental observations described earlier from references 1 through 20, and in particular reference 16. Vortical structures are present in the mixing layer, and the existence and growth of these vortices influence the growth and reaction in the mixing layer. The vortical character can be seen in figure 22, which gives the vorticity distribution in the mixing layer. Chemi-

cal reaction takes place not only in the interior of the mixing layer, but also in the eddies on the edges of the layer. These eddies lie outside the high velocity gradient region of the layer as can be seen by comparing figure 18 with figure 22. Therefore, the resulting flame spreads transversely faster into the unreacted species than did the mixing layer defined by the high velocity gradient zone. Thus, the region of the mixing layer defined by the velocity gradient is not as transversely wide as the flame zone defined by temperature gradient in the mixing layer, in agreement with reference 16.

Figures 23 through 29 show plots at seven streamwise stations ($x = 0.51, 0.58, 1.0, 2.0, 3.0, 4.0,$ and 5.0 cm) of the major chemical species (H_2, O_2, and H_2O) and minor chemical species (OH, H, O, HO_2, and H_2O_2). Contour plots giving the two-dimensional distribution of the species are given in figures 30 through 35. Initially, at $x = 0.51$ cm (fig. 23(b)), fuel and air have just begun to mix, and no significant amount of water has yet formed. A very narrow band of hydrogen peroxide (H_2O_2) is present just above the splitter plate center, and a very small amount of hydroperoxyl (HO_2) lies just below that spike. At $x = 0.58$ cm (fig. 24), the hydrogen and oxygen profiles begin to broaden, but no water has yet appeared in the layer. The hydrogen peroxide spike is still the most predominant, and, while the profile has not broadened, the peak has increased. (Note the ordinate in fig. 24(b) has been rescaled.) A small amount of hydroperoxyl still lies below the hydrogen peroxide peak, and small amounts of atomic hydrogen (H) and atomic oxygen (O) have appeared there. At $x = 1.0$ cm, as described in figure 25, the hydrogen and oxygen profiles have developed, and a small amount of water (8 percent by mass) has been produced in a narrow profile below the splitter plate centerline. The H_2 and O_2 profiles are appropriately depressed in the region of the water peak. Noticeably increased profiles of H, O, and OH also appear at this station just below the splitter plate centerline ($y = 2.5$ cm). The O and OH profiles lie slightly below the water peak, and the H profile lies just above the water peak; this is consistent with the spatial distribution of reactant species. Small amounts of HO_2 and H_2O_2 still remain at and just above the plate centerline.

Figure 26 diagrams the species profiles at $x = 2.0$ cm. The H_2, O_2, and H_2O profiles have broadened significantly more at this station, and the water peak has risen to approximately 23 percent by mass. The minor species profiles have also broadened significantly, with atomic oxygen peaking at 3.0 percent, hydroxyl peaking at 2.0 percent, and atomic hydrogen peaking at 0.8 percent, all by mass.

Small amounts of hydroperoxyl and hydrogen peroxide are still present just above the splitter plate centerline. With further movement downstream at $x = 3.0$ and 4.0 cm (figs. 27 and 28), the major and minor species profiles continue to develop, increasing both in width and in peak values. There are distinct distortions in the H_2 profiles in both figures because of eddies being located on the upper edge of the mixing layer. There is also a general migration of each profile to lower values of y with increasing streamwise coordinate. The increase in product species along the lower edge of the mixing layer is a direct result of preferential burning in this region of the layer. The mixing layer is most nearly stoichiometric there, and the temperature reaches values that favor rapid ignition and combustion. At the last streamwise station given in figure 29, $x = 5.0$ cm, the major and minor species profiles broaden considerably further and shift to even smaller values of y. The noticeable increase in the rate of spread of the species profiles is associated with the second instability that is present in the mixing layer in this region and is consistent with transitioning to a turbulent state.

Two-dimensional contour plots of the species are given in figures 30 through 35. The resulting structure as the mixing layer develops, described previously in figures 15 through 29, can be clearly seen in these figures. The first and second regions of instability are apparent for each species that is shown. The more rapid transverse spread of each species in the latter third of the layer can also be seen. A quiescent region between the two instabilities also occurs for each species, as expected. Additionally, there is a general downward migration of each of the product species with increasing streamwise coordinate. The structure of the product species, typified by water, in the downstream region of the layer is also interesting. The vortical nature of the flow, seen earlier in figure 22, results in regions of unreacted hydrogen gas being captured by regions (or "folds") of product water. Once captured, the regions of hydrogen have difficulty mixing with oxygen so that they can ultimately react. This phenomenon, often termed "unmixedness," reduces the overall level of reaction that can be achieved, and contributes to a reduction in the efficiency of combustion.

This completes the analysis of the spatially evolving, supersonic, reacting mixing layer case using the finite-difference method. All the calculations described above were carried out on the Control Data Corporation VPS-32 computer (an expanded-memory CYBER 205) at the NASA Langley Research Center. The case required 5.1 CPU hours to reach the integration time of 0.1 m/s and used a core memory of 8 million 64-bit words.

4.2 Simulations Using the Hybrid Spectral Algorithm

The hybrid spectral algorithm has also been applied to a spatially developing, laminar, supersonic, chemically reacting mixing layer. As noted earlier, no splitter plate dividing fuel and air is included in this case. Rather, initial profiles of flow variables are prescribed that approximate the flow some small distance downstream of a splitter plate. Except for this modification, the configuration is identical to that considered in section 4.1. That configuration is described schematically in figure 36. Fuel is again introduced at 293 K, and air is introduced at 2000 K. Both fuel and air have an initial free-stream Mach number of 2.0, which ensures that no subsonic zone will occur in the mixing layer because of chemical heat addition or overall losses within the flow. The conditions result in hydrogen and air velocities of 2604 m/s and 1729 m/s, and Reynolds numbers of 4924 and 974, respectively. The previous study discussed in section 4.1 did contain a small subsonic zone in the immediate neighborhood of the splitter plate because of flow separation and a somewhat larger subsonic zone produced by heat addition in the later wake of the layer. It is advantageous to consider flows with the spectral method that are either fully supersonic or fully subsonic, as crossing a sonic line with the method requires special treatment.

The overall domain considered in figure 36 is again 5 cm long, which allows sufficient length for initial development of the mixing layer. The domain is mapped in the transverse direction to $\pm\infty$ with equation (111) of section 3.5.2. This ensures that the transverse boundaries lie well into the free stream so that the boundary conditions discussed in section 3.5.3 are properly posed. Initial and inflow boundary conditions are also chosen to be consistent with section 3.5.3, but in this case they are distributed according to a hyperbolic tangent function that closely approximates the profiles of velocity, static temperature, and species that exit some small distance downstream of a splitter plate. These profiles are also diagramed schematically in figure 36.

By using the configuration and conditions described above, the resulting reacting mixing layer flow field was computed. Before detailed calculations were begun, the hybrid spectral code was first checked against the earlier finite-difference code for this case. The calculations were carried out on a somewhat more coarse 51- by 51-point *grid*, and a simple one-step hydrogen-air chemistry model ($2H_2 + O_2 \rightleftharpoons 2H_2O$) was used in both codes to reduce computation requirements. The detailed 18-equation chemistry scheme was common to both

programs, and therefore it did not require checkout in the spectral code. Results of the comparison at 0.02 ms are given in figures 37 through 40. Agreement between the two programs is excellent in each plot, for both the fluid variables and species mass fractions.

After the compatibility of the spectral and finite-difference codes was verified, the spectral code was then used to carry out more detailed calculations of the mixing layer flow of figure 36. Those calculations were performed on a grid of 201 points in the streamwise (finite-difference) direction and 51 points in the transverse (spectral) direction. The grid was uniform in x and highly compressed in y in the region of the mixing layer. In fact, the spectral grid was chosen to be identical with the grid used for the finite-difference calculation in section 4.1 except for the streamwise compression employed about the splitter plate that was not included in the spectral calculation. The resulting flow field at 0.02 ms is described in figures 41 through 53.

Figure 41 shows a plot of streamwise velocity profiles at four streamwise stations located at $x = 0$, 1.0, 3.0, and 5.0 cm. Without the splitter plate to initiate disturbances and destablize the flow, there is only a small change in the profiles from the initial to the final streamwise station. Careful examination of figure 41 reveals the appearance of two-point oscillations of small amplitude superimposed upon the velocity profiles. These are Gibbs oscillations that occur when a spectral method is used to resolve the large gradients that occur in this study. Gibbs oscillations also occur when other numerical methods are employed, but the spectral method does not have sufficient numerical dissipation to damp the oscillations. In this case, the numerical oscillations grow quite slowly with time, and a standard Laplacian filter applied as a postprocessor following completion of the calculation is sufficient to remove them. Each dependent variable is therefore filtered by applying

$$\varsigma_{i,j} \leftarrow \varsigma_{i,j} + \frac{(\Delta y_j)^2}{4} \nabla^2 \varsigma_{i,j} \qquad (114)$$

where ς represents ρ, u, v, E, and f_i. When the coefficient leading the Laplacian is sufficiently small ($\Delta y^2/4 = 6 \times 10^{-10}$ in this case) the filter dissipates only the two-point oscillations and leaves the values about their mean unaffected. Results from figure 41 following filtering are given in figure 42. There are no structural changes in figure 42 relative to figure 41 and the two-point oscillations apparent in figure 41 have been removed in figure 42.

Figure 43 shows a plot of streamwise velocity versus streamwise coordinate at the three transverse sta-

tions chosen in the finite-difference study. Note that the upstream and downstream instabilities that were present before do not occur in this case. The lack of the upstream instability is expected since the separation just downstream of the splitter plate initiated the instability in the finite-difference study. The lack of the downstream instability in this study seems to be due to the loss of a triggering mechanism for transition by the upstream disturbance. To resolve this issue, the identical problem considered here was computed with the finite-difference code of section 4.1. Results from that analysis, again at 0.02 ms, are shown in figure 44. The results demonstrate the same behavior as those given in figure 43. Therefore, it appears that the downstream disturbance and transition of the mixing layer is dependent on an initial triggering by the upstream instability. Significantly longer calculations in time using the finite-difference program, in the absence of a splitter plate, never yielded transition within the 5-cm length of the physical domain of this problem.

Figure 45 gives a plot of temperature versus streamwise coordinate at the three transverse stations chosen in figure 43. Again, there is no evidence of the upstream and downstream instabilities present in the study with the splitter plate. Figure 46 describes temperature profiles in the mixing layer at the four streamwise stations chosen in figure 42. As the flow evolves in x, there is a noticeable increase in temperature just below the center of the layer because of the exothermic chemical reactions taking place there. The results of chemical reaction can be seen more directly in figures 47 through 53, which show the spatial evolution of the major (H_2, O_2, and H_2O) and minor (H, O, OH, HO_2, and H_2O_2) chemical species at seven streamwise stations located at 0, 0.4, 1.0, 2.0, 3.0, 4.0, and 5.0 cm.

Figure 47 diagrams the initial distribution of reactant species at $x = 0$ cm. No product species have formed at this station. Figure 48(a) shows the major species distribution a short distance downstream from the initial station at $x = 0.4$ cm. Initial reaction has begun at this location and a small narrow profile of water (about 5 percent by mass) has formed. There are local depressions in the hydrogen and oxygen mass fraction profiles in the region of water production. Comparison of figure 48(a) with 46 also shows that this region correctly corresponds to that of the peak temperature in the flow. As in the earlier finite-difference calculations of section 4.1, the zone of water production represents the region nearest stoichiometric conditions and at the required elevated temperature for chemical reaction, so it is reasonable that water initially forms here. The minor species distributions at $x = 0.4$ cm are given

in figure 48(b). Atomic hydrogen lies in the immediate neighborhood of the water profile and peaks at 0.2 percent by mass, whereas the hydroxyl and atomic oxygen profiles extend well below the water and peak at 0.8 and 0.96 percent, respectively. Small amounts of hydroxyl (0.002 percent) and hydrogen peroxide ($< 10^{-4}$ percent) also exist and lie just above the water peak. These distributions are again in agreement with the finite-difference results, with OH and O lying at or below the water where stoichiometry favors their higher population and H lying at or above the water for a like reason.

Figure 49 shows major and minor species profiles at 1.0 cm downstream from the initial station. All product species attain significantly higher peak values at this location, and the profiles have broadened considerably. Water peaks at 22 percent by mass, and hydroxyl, atomic hydrogen, and atomic oxygen peak at 2.4, 1.1, and 2.8 percent, respectively. The OH and O profiles shift to lower values of y, whereas the H profile moves to a larger value. The hydroperoxyl profile shifts to a somewhat higher value of y but retains nearly the same peak value, whereas the hydrogen peroxide profile remains at nearly the same location and reaches a slightly higher peak (0.0007 percent). Species profiles continue to broaden at $x = 2.0$ cm as shown in figure 50. There are slight increases in the peak values of water (23 percent) and atomic hydrogen (1.2 percent), and a slight decrease in atomic oxygen (2.6 percent). The remaining species remain essentially unchanged. There are very slight shifts in the transverse coordinate of the peak species values, but these shifts do not appear to be significant.

There is no significant change in species profiles beyond the $x = 2.0$ cm station, and the chemistry appears to have reached a local equilibrium with the flow. Comparison of figure 50 at $x = 2.0$ cm with figures 51, 52, and 53 at $x = 3.0$, 4.0, and 5.0 cm, respectively, confirms this observation. This downstream evolution of the chemistry differs considerably from the finite-difference study of section 4.1. This difference in evolution again appears to be linked to the absence of flow instabilities spawned by the presence of the splitter plate included in the finite-difference analysis. The effects of the splitter plate on flow instabilities were discussed in section 3 and in section 4.1. Without the presence of the first instability, early mixing is reduced and transition does not occur in the layer within the limits of the domain that is considered. In the absence of downstream transition, downstream mixing is significantly retarded.

To study the effects of the inflow perturbations imposed on the flow by the splitter plate, the finite-difference calculation of section 4.1 was reconsidered.

It was found from analyzing computed results as a function of time at the first station downstream of the splitter plate trailing edge that perturbations imposed on the flow variables could be correlated quite well by using a single perturbation function. That function was given by

$$\Phi' = e^{-(ay)^2} A \sin{(\omega t)} \qquad (115)$$

where

$$a = 1000$$

$$A = 0.064$$

$$\omega = 12\,271\,061 \text{ rad/s}$$

The exponential term damps the effects of the perturbation with transverse movement away from the plate. The trigonometric function describes the periodic nature of the disturbance, and A is the amplitude of the disturbance, normalized by the free-stream velocity.

The flow perturbation described by equation (115) is now applied to the present analysis by using the spectral program. Recalling the discussion in section 1, it was noted in reference 21 that for reacting flows, the eigenvalues that determine flow stability are only weakly dependent on Mach number. Therefore, it appears reasonable to apply the perturbation data from the finite-difference analysis to this problem. Each primitive fluid variable was then perturbed at the inflow boundary as described by equation (115). The initial streamwise velocity, for example, is then given by

$$u = U_\infty(1 + \phi') \qquad (116)$$

A similar procedure is also used to describe the inflow density and pressure. All other required fluid inflow data can then be computed as usual. The transverse velocity component remains fixed at zero as in the previous analysis, roughly representing the flow just downstream of the recompression shock in the finite-difference study. The spectral technique cannot capture strong shocks in supersonic flow that would occur with the imposition of the transverse velocity, and, therefore, that problem could not be dealt with here.

Results from the spectral study, again at 0.02 ms, using the inflow perturbation described above are given in figures 54 through 70. Figure 54 shows a plot of streamwise velocity versus streamwise coordinate at the same three transverse stations pictured in figure 43 for the unperturbed study. Note that the instability introduced at the inflow boundary now

persists through the solution domain. The disturbance does not appear to be amplified significantly, however. There are three regions of instability in the streamwise direction, each separated by a zone where the oscillations are damped. These damped zones occur at approximately 0.7 and 3.0 cm. These results are similar in certain respects to those seen in the finite-difference analysis at 0.02 ms as given in figure 16(d). There are three regions of instability in figure 16(d), but the second damped zone occurs further upstream. Also, the downstream region of instability is larger, of greater amplitude, and of increasing wavelength. From this comparison, it appears likely that the mechanism initiating the instabilities in the finite-difference study is more complex than that assumed in the present study. The assumed form of the perturbation does, however, allow study of the effects of such an instability on the development of the mixing layer and the resulting chemical reactions. These effects are assessed by comparing results from perturbed and unperturbed spectral studies.

Figure 55 gives a plot of streamwise velocity versus transverse coordinate at four streamwise stations. The unperturbed results at the same four stations are given in figure 42. Note that now there is a marked shift in the overall magnitude of each velocity profile because of the temporal perturbation, but the profile development is not significantly affected.

Figure 56 shows a plot of streamwise velocity contours in the mixing layer. The structure described by figure 54 is shown to persist throughout the layer, and there is no marked growth of the mixing layer thickness as defined by the velocity gradient. Similar results are yielded by the plot of vorticity contours given in figure 57. There again is no significant growth of the layer, but the perturbation does produce vortical structure, albeit of lesser scale than that observed in the calculation including the splitter plate.

Figure 58 describes the temperature field with increasing streamwise coordinate at the three transverse locations used in the unperturbed solution of figure 45. The streamwise structure is again apparent in this plot. Comparison of figure 58 with figure 19, which gives the streamwise temperature development in the flow with the splitter plate, shows similar behavior of the profiles near, just above, and below the plate. The profiles are quite different well downstream of the plate, however, because of the absence of transition without the plate. Figure 59 describes transverse temperature profiles with streamwise distance in the perturbed layer. The results are quite similar to those of the unperturbed flow given in figure 46, although slightly higher peak temperatures are achieved in the perturbed solution.

Profiles and contours of the chemical species present in the perturbed reacting mixing layer are given in figures 60 through 70. Figure 60 shows profiles of the major species (H_2, O_2, and H_2O) at the initial station of the calculation. No water has been formed at this station. Since the chemical species are unperturbed at the inflow boundary, figure 60 is identical to the results for the nonperturbed case given in figure 47. Figure 61 describes the species distribution at $x = 0.4$ cm downstream of the inflow boundary. The water profile is somewhat more broad but has a slightly lower peak than the unperturbed solution in figure 48(a). The minor species also peak about 0.1 percent lower than the unperturbed solution given in figure 48(b). The small differences in the two solutions appear to be due to a somewhat higher rate of mixing due to the perturbation, which would increase the transverse spread of the profile and reduce its peak. The trends in profile spread established at $x = 0.4$ cm continue at the $x = 1.0$-cm station given in figure 62. By comparing figure 62 with 50, it can be seen that the profile peaks are identical, but the perturbed profiles are slightly broader. With each succeeding downstream station beyond $x = 1.0$ cm, the species profiles of the perturbed problem continue to become transversely more broad than the unperturbed study because of the improved mixing afforded by the perturbation. The mixing process remains laminar, however, since the induced instability is never sufficient to trigger transition in the latter portion of the mixing layer. This behavior can be seen even more clearly in the product species contour plots of the perturbed mixing layer, given in figures 67 through 70. The perturbation on the fluid variables induces an instability in these species that is initially quite strong. The instability decays with downstream movement, however, and it has essentially dissipated by the time the outflow boundary is reached. Therefore, the species distributions indicate, as did the fluid variable results, that the mechanism that triggers transition in the mixing layer flow is more complex than the function that was assumed. These issues of reacting flow stability are further addressed in the conclusions discussed in section 5.

The calculations described above were carried out on the VPS-32 computer at the NASA Langley Research Center. The case required 7.0 CPU hours to reach the integration time 0.02 ms and used a core memory of 7.2 million 64-bit words on a 201 by 51 grid.

5. Conclusions

Research has been undertaken in this study to achieve an improved understanding of important

physical phenomena present when a supersonic flow undergoes chemical reaction. To explore the behavior of such flows, detailed physical models of convective and diffusive mixing and finite-rate chemical reaction in supersonic flow were developed. Two numerical algorithms were then constructed to solve the equations governing supersonic chemically reacting flow that resulted from these models. The first algorithm was developed around an established finite-difference technique modified to consider multicomponent reacting flow. The second algorithm employed a hybrid pseudospectral technique in one spatial direction for improved resolution of the reacting flow field. The previous scheme was retained in the other spatial direction. Computer programs were written using both algorithms, and each program was used to study a spatially developing and reacting supersonic mixing layer. The results obtained from these studies were then analyzed, and conclusions were drawn concerning the structure of the reacting mixing layer. Those conclusions, which were discussed in section 4, are now summarized.

Supersonic reacting flows exhibited many of the same features observed for subsonic reacting and nonreacting flows. In particular, the vortical structure of the flow, noted in much of the subsonic nonreacting flow literature, was shown for the first time to be quite predominant in supersonic reacting flow as well. In agreement with the earlier reacting subsonic literature, the vortical structure had a marked effect on chemical reaction in supersonic flow. Significant burning took place in the eddies on the edges of the mixing layer, broadening the reaction zone relative to the layer thickness defined by the velocity gradient. In addition, the vortical flow resulted in the roll up of unburned reactants inside a layer of partially or fully burned products. This phenomenon, often termed "unmixedness" in subsonic flows, prohibited the reaction of captured reactants and reduced the overall efficiency of the combustion process. Unmixedness was thus shown for the first time to be a potential problem in reducing the efficiency of supersonic combustion as well as subsonic combustion, and techniques will likely be needed to reduce its effects.

Calculations with the present model also showed that at supersonic speeds the reacting mixing layer remained laminar for the region studied if no external disturbance to trigger transition to turbulence was introduced. When a splitter plate was used to initially separate fuel and air, however, it provided the required disturbance. The unstable recirculating flow that formed at the base of the splitter plate, following the Prandtl-Meyer expansion off the plate and the unstable recompression shock a short distance down-

stream, provided that disturbance. The resulting oscillatory flow then propagated downstream triggering transition-like phenomena in the latter fourth of the domain being studied. Mixing of fuel and air then improved dramatically in this region, markedly increasing chemical reaction as evidenced by the spread of product profiles. To study the effect of heat release in this region, calculations were also carried out without chemical reaction. Results showed that the unstable region near the splitter plate was unaffected when reaction was removed. There was no reaction in the early part of this region, and reaction was mainly endothermic further downstream, so little effect was expected. Well downstream in the transition-like region, the reaction was highly exothermic, however, and removing chemical reaction (and therefore, chemical heat release) caused the amplitude of the disturbance there to increase significantly. This result was in agreement with earlier experimental and numerical literature for subsonic flow, where it was found that heat release retarded mixing. This effect was thus shown for the first time to occur in supersonic reacting flow as well.

This study also represented the first application of spectral methods to study supersonic reacting flows. The hybrid spectral method employed in this study was used to predict the spatial development of a supersonic, chemically reacting mixing layer. The first case studied considered the development of a mixing layer downstream of a splitter plate separating fuel and air. No plate was included in the calculation; rather the effects of the plate were modeled by using an appropriate initial profile. As in one of the finite-difference studies, the layer without the plate never developed a sufficient upstream disturbance to trigger transition in the downstream region of the problem that was studied. To initiate transition, data were taken from the upstream disturbance that caused transition in the finite-difference study and were correlated to form an initial perturbation function on the inflow field of the spectral study. The perturbation alone was not sufficient to trigger transition in the spectral study, although species mixing and chemical reaction were enhanced well downstream. It was therefore concluded that transition was initiated in the finite-difference study by a mechanism more complicated than that represented by the simple perturbation function used in the spectral study.

References

1. Drummond, J. Philip; Rogers, R. Clayton; and Evans, John S.: Combustor Modelling for Scramjet Engines. *Combustor Modelling*, AGARD-CP-275, Feb. 1980, pp. 10-1–10-30.

2. Drummond, J. Philip; and Weidner, Elizabeth H.: Numerical Study of a Scramjet Engine Flowfield. *AIAA J.*, vol. 20, no. 9., Sept. 1982, pp. 1182–1187.

3. Drummond, J. Philip: Numerical Study of a Ramjet Dump Combustor Flowfield. *AIAA J.*, vol. 23, no. 4, Apr. 1985, pp. 604–611.

4. Carpenter, Peter W.: A Numerical Investigation Into the Effects of Compressibility and Total Enthalpy Difference on the Development of a Laminar Free Shear Layer. *J. Fluid Mech.*, vol. 50, pt. 4, Dec. 29, 1971, pp. 785–799.

5. Brown, Garry L.; and Roshko, Anotol: On Density Effects and Large Structure in Turbulent Mixing Layers. *J. Fluid Mech.*, vol. 64, pt. 4, July 24, 1974, pp. 775–816.

6. Roshko, A.: Progress and Problems in Understanding Turbulent Shear Flows. *Turbulent Mixing in Nonreactive and Reactive Flows*, S. N. B. Murthy, ed., Plenum Press, c.1975, pp. 295–316.

7. Ferziger, Joel H.; and McMillan, O. J.: *Studies of Structure and Modeling in Turbulent Shear Flows*. NEAR TR 335 (Contract No. N00014-82-C-0672), Nielsen Engineering and Research, Inc., Dec. 1984. (Available from DTIC as AD A151 807.)

8. Oh, Y. H.: Analysis of Two-Dimensional Free Turbulent Mixing. AIAA Paper No. 74-594, June 1974.

9. Papamoschou, D.; and Roshko, A.: Observations of Supersonic Free Shear Layers. AIAA-86-0162, Jan. 1986.

10. Hussaini, M. Y.; Collier, F.; and Bushnell, D. M.: Turbulence Alteration Due to Shock Motion. *Turbulent Shear-Layer/Shock-Wave Interactions*, J. Délery, ed., Springer-Verlag, c.1986, pp. 371–381.

11. Yule, A. J.; Chigier, N. A.; and Thompson, D.: Coherent Structures in Combustion. *Symposium on Turbulent Shear Flows*, Pennsylvania State Univ., 1977, pp. 7.41–7.50.

12. Masutani, S. M.; and Bowman, C. T.: *The Structure of a Chemically Reacting Plane Mixing Layer.* Stanford Univ. paper presented at the Western States Section/Combustion Inst. 1984 Spring Meeting (Boulder, Colorado), Apr. 2–3, 1984.

13. Keller, Jay O.; and Daily, John W.: The Effects of Large Heat Release on a Two Dimensional Mixing Layer. AIAA-83-0472, Jan. 1983.

14. Mungal, M. G.; Dimotakis, P. E.; and Hermanson, J. C.: Reynolds Number Effects on Mixing and Combustion in a Reacting Shear Layer. AIAA-84-0371, Jan. 1984.

15. Hermanson, J. C.; Mungal, M. G.; and Dimotakis, P. E.: Heat Release Effects on Shear Layer Growth and Entrainment. AIAA-85-0142, Jan. 1985.

16. Pitz, Robert W.; and Daily, John W.: Combustion in a Turbulent Mixing Layer Formed at a Rearward-Facing Step. *AIAA J.*, vol. 21, no. 11, Nov. 1983, pp. 1565–1570.

17. Broadwell, James E.; and Dimotakis, Paul E.: Implications of Recent Experimental Results for Modeling Reactions in Turbulent Flows. AIAA-84-0545, Jan. 1984.

18. Carrier, G. F.; Fendell, F. E.; and Marble, F. E.: The Effect of Strain Rate on Diffusion Flames. *SIAM J. Appl. Math.*, vol. 28, no. 2, Mar. 1975, pp. 463–500.

19. Riley, James J.; and Metcalfe, Ralph W.: Direct Simulations of Chemically Reacting Turbulent Mixing Layers. AIAA-85-0321, Jan. 1985.

20. McMurtry, P. A.; Jou, W.-H.; Riley, J. J.; and Metcalfe, R. W.: Direct Numerical Simulations of a Reacting Mixing Layer With Chemical Heat Release. AIAA-85-0143, Jan. 1985.

21. Menon, S.; Anderson, J. D., Jr.; and Pai, S. I.: Stability of a Laminar Premixed Supersonic Free Shear Layer With Chemical Reactions. *Int. J. Eng. Sci.*, vol. 22, no. 4, 1984, pp. 361–374.

22. Seinfeld, John H.; Lapidus, Leon; and Myungkyu, Hwang: Review of Numerical Integration Techniques for Stiff Ordinary Differential Equations. *Ind. & Eng. Chem. Fundam.*, vol. 9, no. 2, May 1970, pp. 266–275.

23. Bussing, T. R. A.; and Murman, E. M.: A Finite Volume Method for the Calculation of Compressible Chemically Reacting Flow. AIAA-85-0331, Jan. 1985.

24. Stalnaker, J. F.; Robinson, M. A.; Spradley, L. W.; Kurzius, S. C.; and Thoenes, J.: *Development of the General Interpolants Method for the CYBER 200 Series of Supercomputers.* NASA CR-4183, 1988.

25. Widhopf, George F.; and Victoria, Keith J.: On the Solution of the Unsteady Navier-Stokes Equations Including Multicomponent Finite Rate Chemistry. *Comput. & Fluids*, vol. 1, no. 2, June 1973, pp. 159–184.

26. Smoot, L. Douglas; Hecker, William C.; and Williams, Gerald A.: Prediction of Propagating Methane-Air Flames. *Combust. & Flame*, vol. 26, no. 3, June 1976, pp. 323–342.

27. Hussaini, M. Y.; Kopriva, D. A.; Salas, M. D.; and Zang, T. A.: Spectral Methods for the Euler Equations: Part II - Chebyshev Methods and Shock Fitting. *AIAA J.*, vol. 23, no. 2, Feb. 1985, pp. 234–240.

28. Hussaini, M. Y.; Salas, M. D.; and Zang, T. A.: Spectral Methods for Inviscid, Compressible Flows. *Advances in Computational Transonics*, W. G. Habashi, ed., Pineridge Press (Swansea, U.K.), c.1985, pp. 875–912.

29. Gottlieb, David; and Orszag, Steven A.: *Numerical Analysis of Spectral Methods: Theory and Applications.* Soc. for Industrial and Applied Mathematics, c.1976.

30. Drummond, J. Philip; Hussaini, M. Yousuff; and Zang, Thomas A.: Spectral Methods for Modeling Supersonic Chemically Reacting Flowfields. *AIAA J.*, vol. 24, no. 9, Sept. 1986, pp. 1461–1467.

31. MacCormack, Robert W.: The Effect of Viscosity in Hypervelocity Impact Cratering. AIAA-69-354, Apr.–May 1969.

32. Dwyer, H. A.; and Sanders, B. R.: Modeling of Unsteady Combustion Phenomena. AIAA-77-136, Jan. 1977.

33. McBride, Bonnie J.; Heimel, Sheldon; Ehlers, Janet G.; and Gordon, Sanford: *Thermodynamic Properties to $6000°K$ for 210 Substances Involving the First 18 Elements*. NASA SP-3001, 1963.

34. Rogers, R. C.; and Chinitz, W.: Using a Global Hydrogen-Air Combustion Model in Turbulent Reacting Flow Calculations. *AIAA J.*, vol. 21, no. 4, Apr. 1983, pp. 586–592.

35. Williams, Forman A.: *Combustion Theory*. Addison-Wesley Publ. Co., Inc., c.1965.

36. Brigham, E. Oran: *The Fast Fourier Transform*. Prentice-Hall, Inc., c.1974.

37. Gottlieb, David; Hussaini, M. Yousuff; and Orszag, Steven A.: Theory and Applications of Spectral Methods. *Spectral Methods for Partial Differential Equations*, Robert G. Voigt, David Gottlieb, and M. Yousuff Hussaini, eds., Soc. for Industrial and Applied Mathematics, 1984, pp. 1–54.

38. Li, C. P.: Time-Dependent Solutions of Nonequilibrium Airflow Past a Blunt Body. AIAA-71-595, June 1971.

39. Vandergraft, James S.: *Introduction to Numerical Computations*, Second ed. Academic Press, Inc., 1983.

40. Anderson, Dale A.; Tannehill, John C.; and Pletcher, Richard H.: *Computational Fluid Mechanics and Heat Transfer*. Hemisphere Publ. Corp., c.1984.

41. Kanury, A. Murty: *Introduction to Combustion Phenomena*. Gordon and Breach Science Publ., Inc., c.1975.

42. Jachimowski, Casimir J.: *An Analytical Study of the Hydrogen-Air Reaction Mechanism With Application to Scramjet Combustion*. NASA TP-2791, 1988.

43. White, Frank M.: *Viscous Fluid Flow*. McGraw-Hill, Inc., c.1974.

44. Svehla, Roger A.: *Estimated Viscosities and Thermal Conductivities of Gases at High Temperatures*. NASA TR R-132, 1962.

45. Wilke, C. R.: A Viscosity Equation for Gas Mixtures. *Chem. Phys.*, vol. 18, no. 4, Apr. 1950, pp. 517–519.

46. Berman, Harry A.; Anderson, John D., Jr.; and Drummond, J. Philip: Supersonic Flow Over a Rearward Facing Step With Transverse Nonreacting Hydrogen Injection. *AIAA J.*, vol. 21, no. 12, Dec. 1983, pp. 1707–1713.

47. Wilkinson, J. H.: *The Algebraic Eigenvalue Problem*. Clarendon Press (Oxford), 1965.

48. Householder, Alston S.: *The Theory of Matrices in Numerical Analysis*. Dover Publ., Inc., c.1964.

49. Thomas, P. D.; Vinokur, M.; Bastianon, R. A.; and Conti, R. J.: Numerical Solution for Three-Dimensional Inviscid Supersonic Flow. *AIAA J.*, vol. 10, no. 7, July 1972, pp. 887–894.

50. Smith, Robert E.; and Weigel, Barbara L.: Analytic and Approximate Boundary-Fitted Coordinate Systems for Fluid Flow Simulation. AIAA-80-0192, Jan. 1980.

51. Boyd, John P.: The Optimization Convergence for Chebyshev Polynomial Methods in an Unbounded Domain. *J. Comput. Phys.*, vol. 45, no. 1, Jan. 1982, pp. 43–79.

Table I. Finite-Rate Chemistry Model and Rate Coefficients for Each Reaction

Reaction number	Reaction	Reaction rate variables		
		A_i	N_i	Activation energy, cal/g-mole
1	$H_2 + O_2 = OH + OH$	$.170 \times 10^{14}$	0	48 150
2	$H + O_2 = OH + O$	$.142 \times 10^{15}$	0	16 400
3	$OH + H_2 = H_2O + H$	$.316 \times 10^8$	1.80	3 030
4	$O + H_2 = OH + H$	$.207 \times 10^{15}$	0	13 750
5	$OH + OH = H_2O + O$	$.550 \times 10^{14}$	0	7 000
6	$H + OH = H_2O + M$	$.221 \times 10^{23}$	-2.00	0
7	$H + H = H_2 + M$	$.653 \times 10^{18}$	-1.00	0
8	$H + O_2 = HO_2 + M$	$.320 \times 10^{19}$	-1.00	0
9	$HO_2 + OH = H_2O + O_2$	$.500 \times 10^{14}$	0	1 000
10	$HO_2 + H = H_2 + O_2$	$.253 \times 10^{14}$	0	700
11	$HO_2 + H = OH + OH$	$.199 \times 10^{15}$	0	1 800
12	$HO_2 + O = OH + O_2$	$.500 \times 10^{14}$	0	1 000
13	$HO_2 + HO_2 = H_2O_2 + O_2$	$.199 \times 10^{13}$	0	0
14	$HO_2 + H_2 = H_2O_2 + H$	$.301 \times 10^{12}$	0	18 700
15	$H_2O_2 + OH = HO_2 + H_2O$	$.102 \times 10^{14}$	0	1 900
16	$H_2O_2 + H = OH + H_2O$	$.500 \times 10^{15}$	0	10 000
17	$H_2O_2 + O = OH + HO_2$	$.199 \times 10^{14}$	0	5 900
18	$M + H_2O_2 = OH + OH$	$.121 \times 10^{18}$	0	45 500
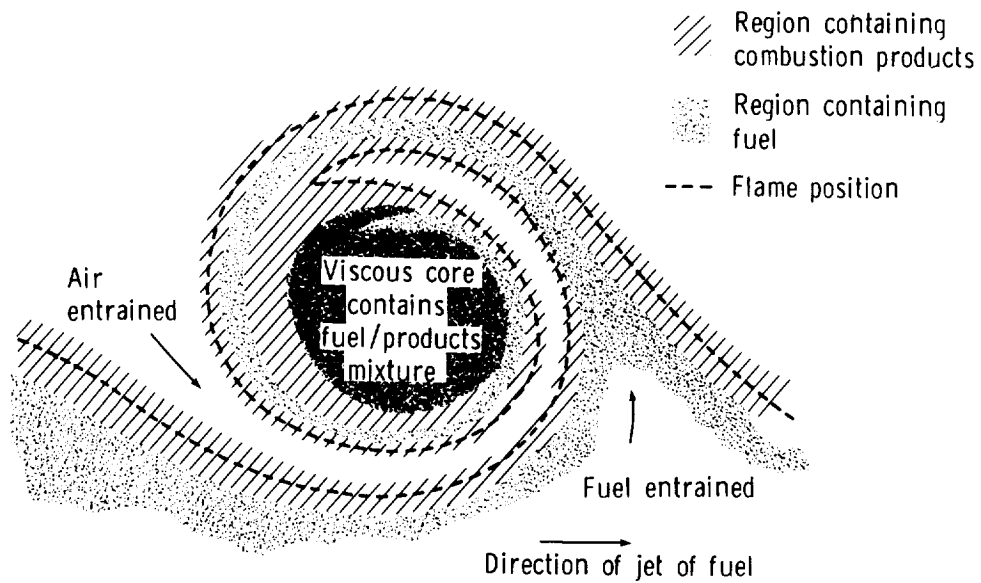
Figure 1. Cross section of transitional "vortex" eddy in gas diffusion flame (ref. 11).
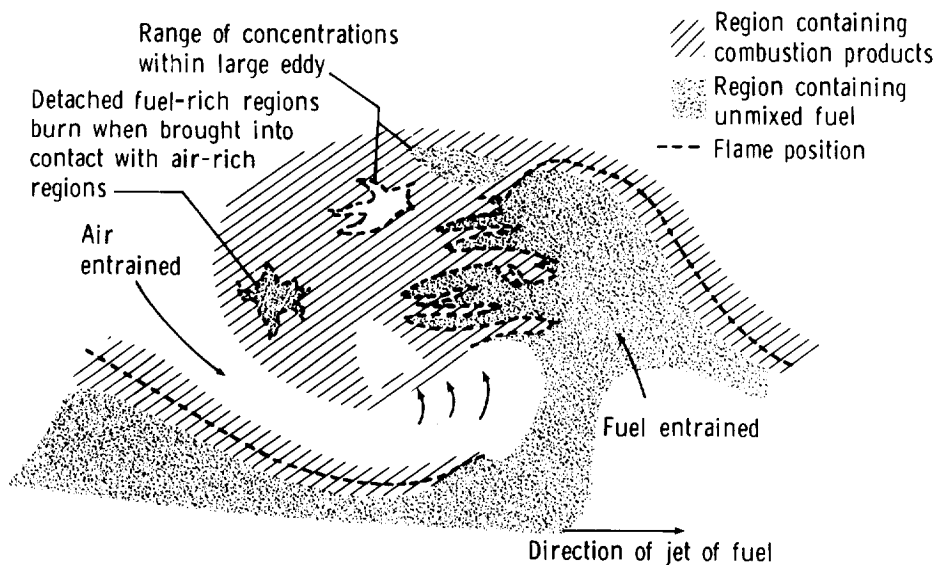
Figure 2. Cross section of large turbulent eddy in gas diffusion flame (ref. 11).
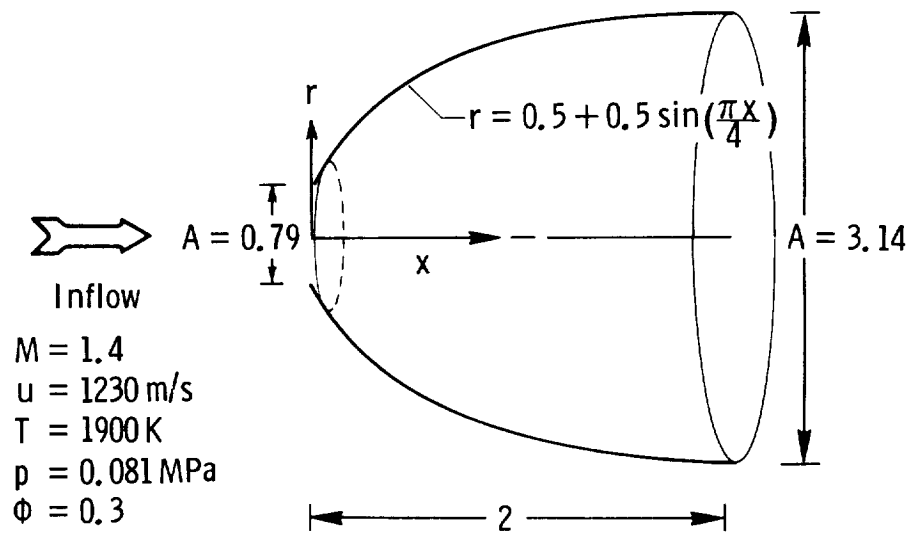
Figure 3. Rapid expansion supersonic diffuser test case.
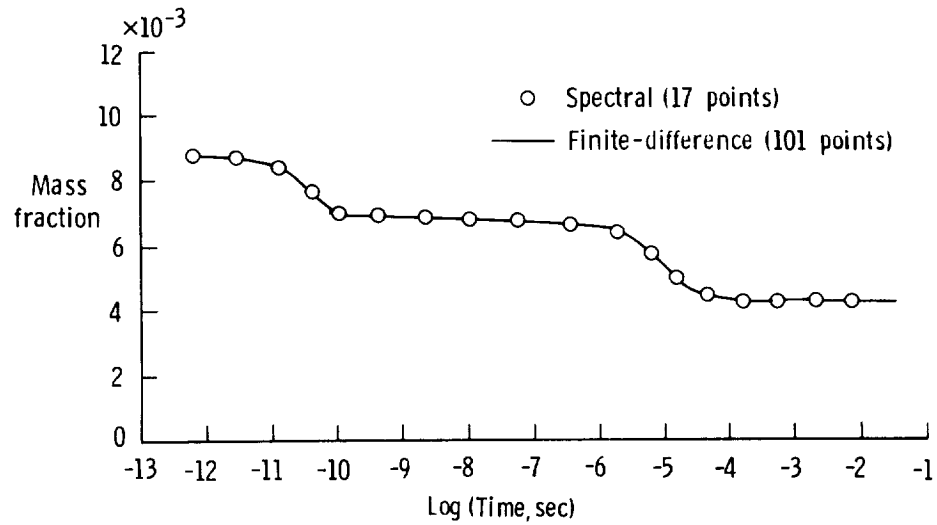
Figure 4. History of hydrogen mass fraction.
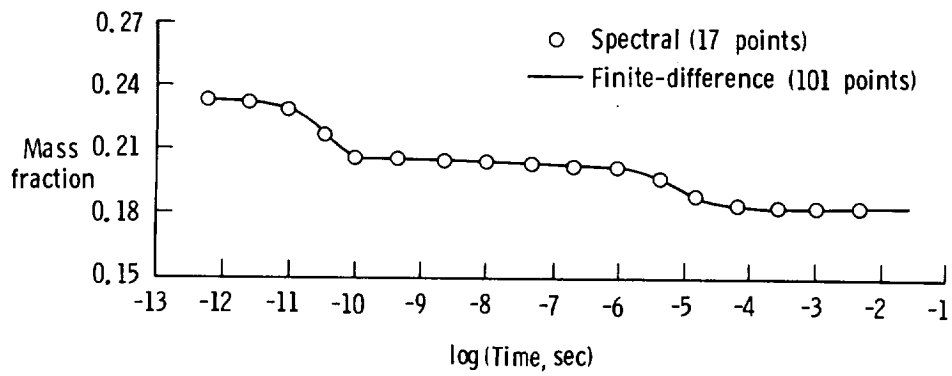
Figure 5. History of oxygen mass fraction.
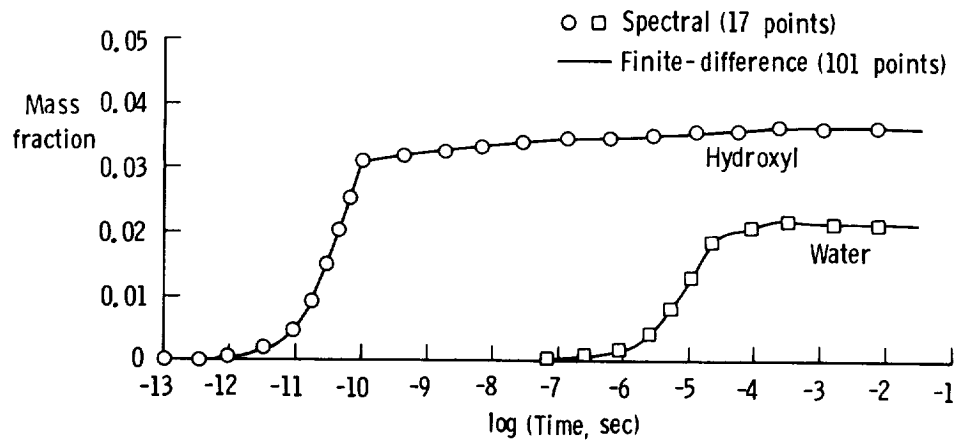
Figure 6. Histories of hydroxyl and water mass fractions.
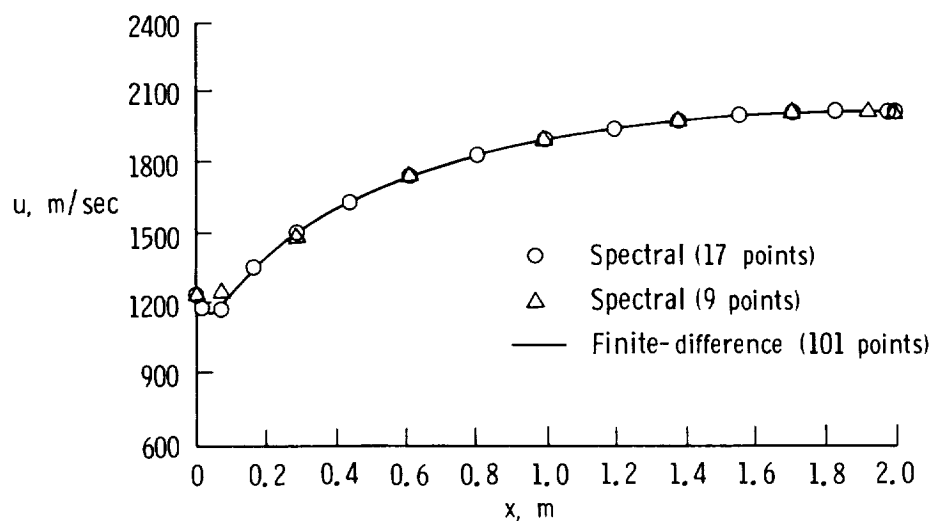
Figure 7. Axial velocity distributions.
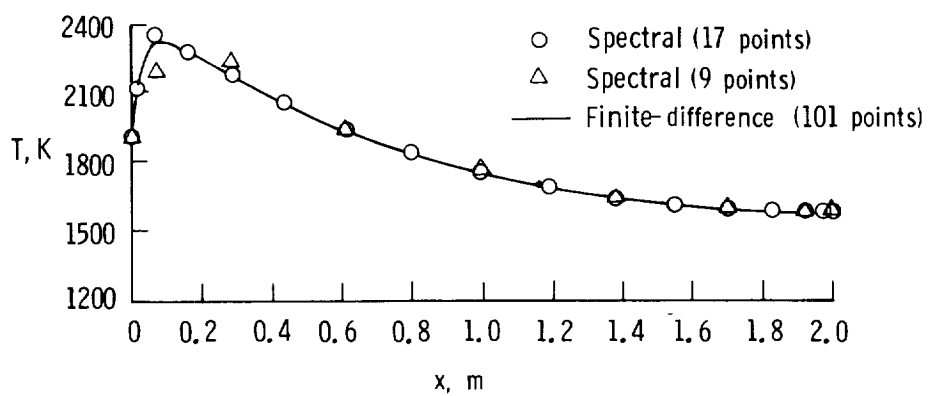
Figure 8. Axial temperature distributions.
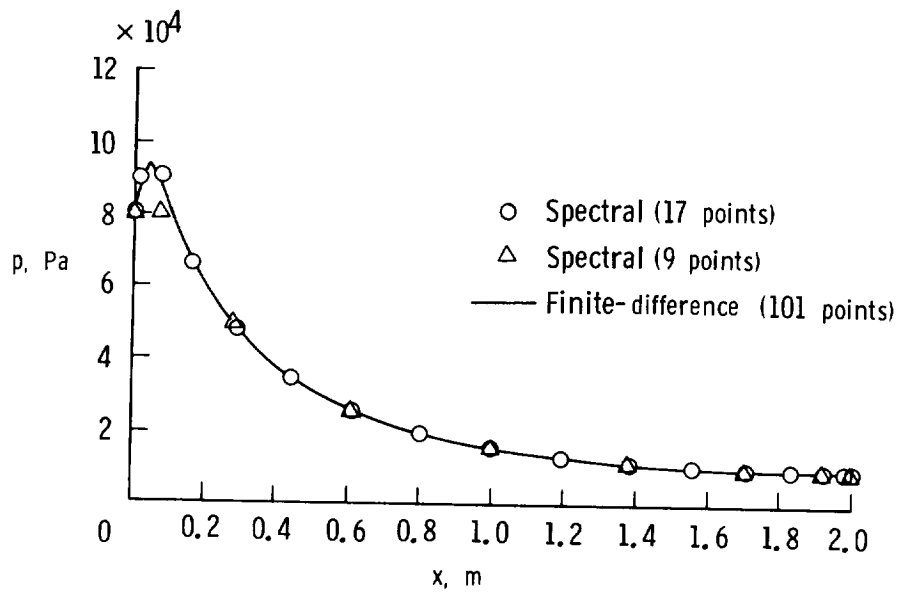
Figure 9. Axial pressure distributions.
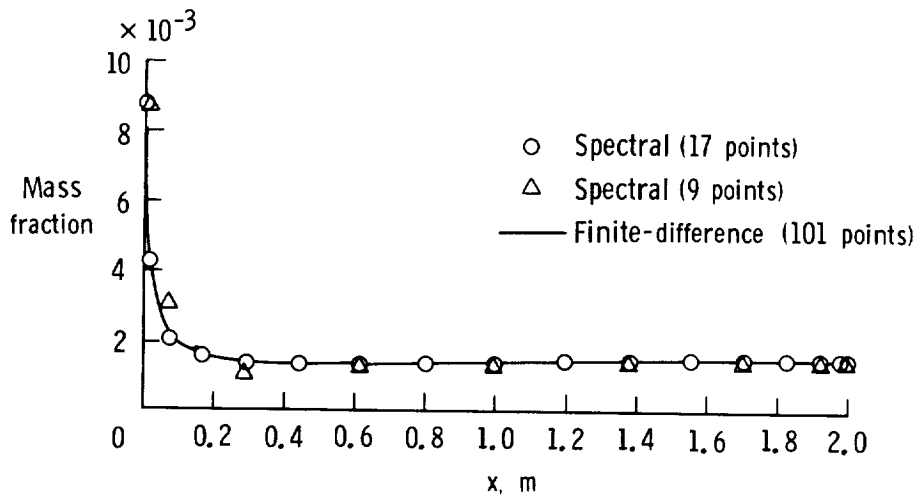
Figure 10. Axial hydrogen mass fraction distributions.
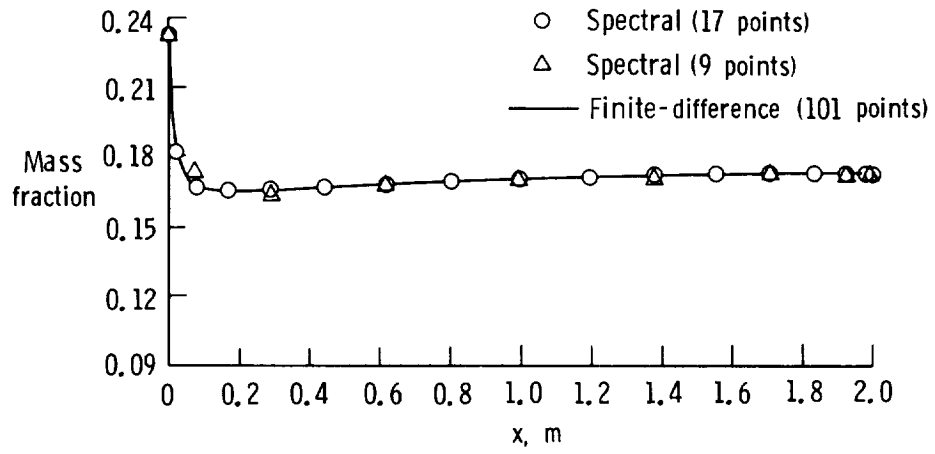
Figure 11. Axial oxygen mass fraction distributions.
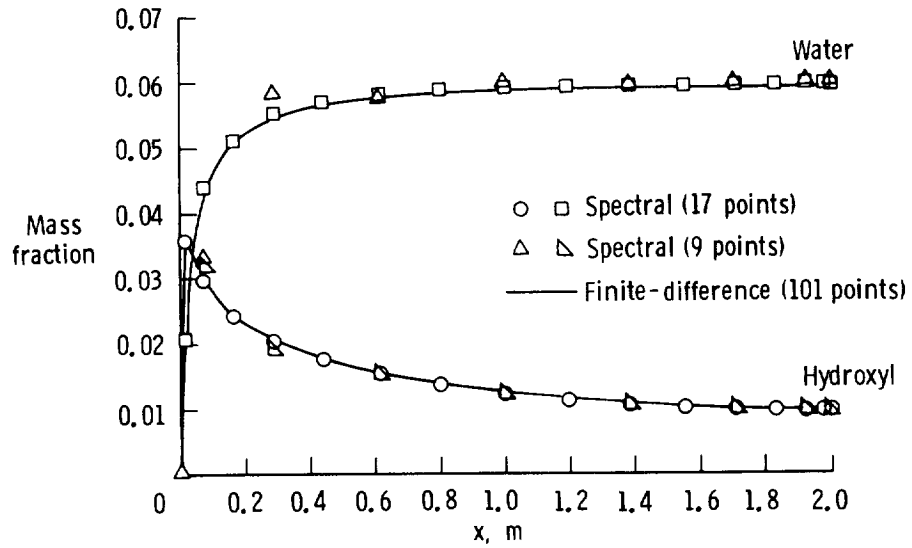
Figure 12. Axial hydroxyl and water mass fraction distributions.
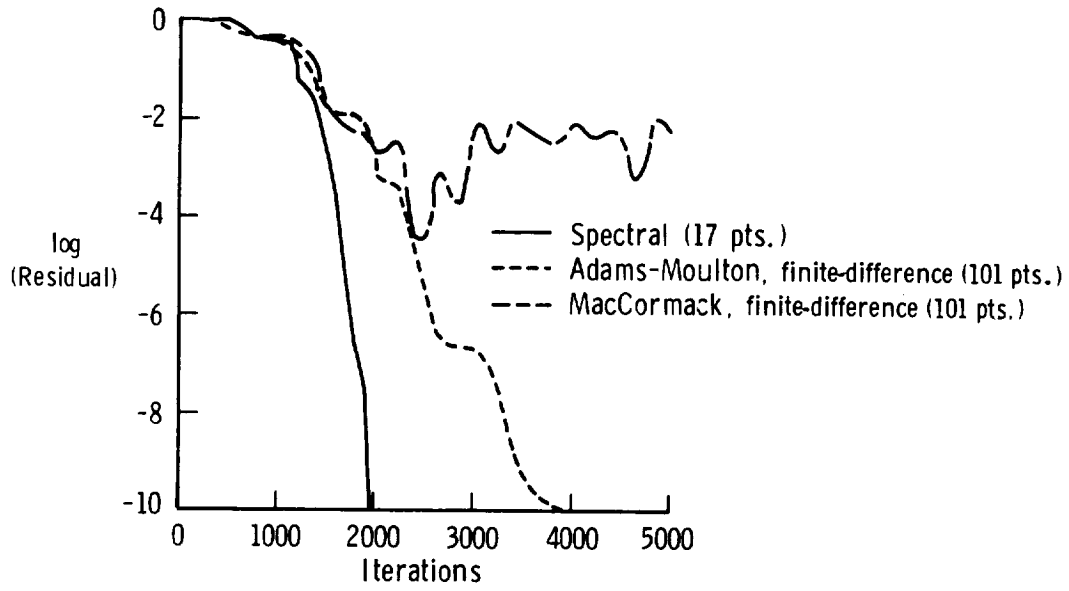
Figure 13. Steady-state residual reduction rates of the methods.
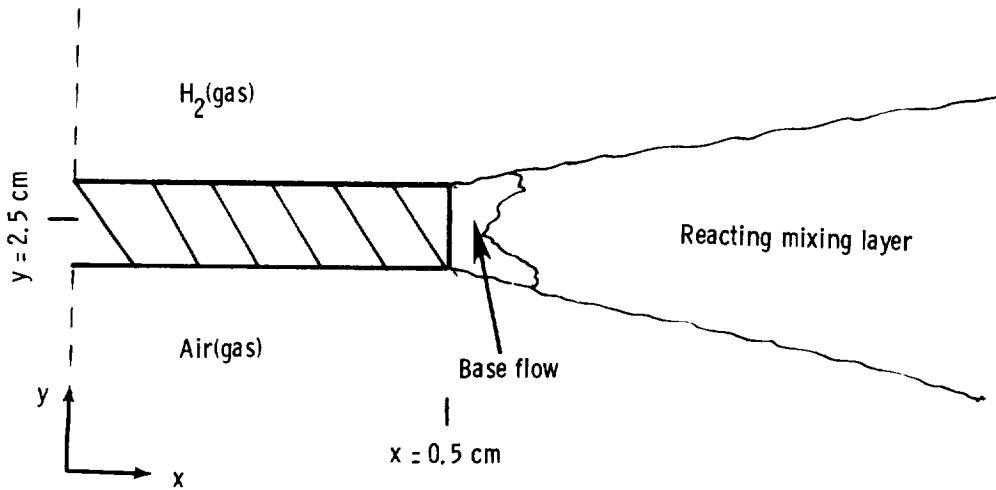
Figure 14. Reacting mixing layer schematic.
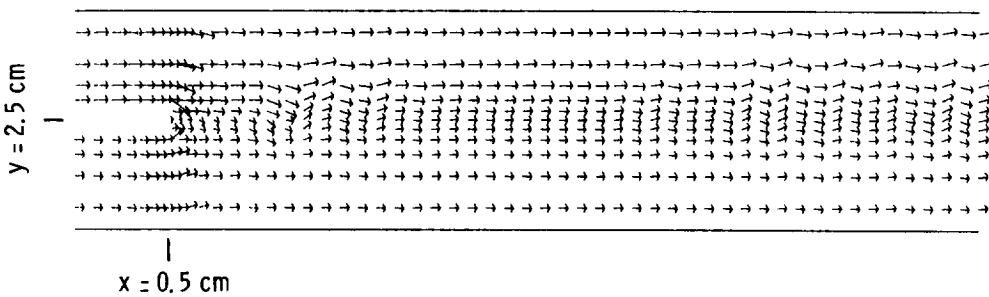
Figure 15. Mixing layer velocity vector field (every fourth vector plotted (0.1 ms)).
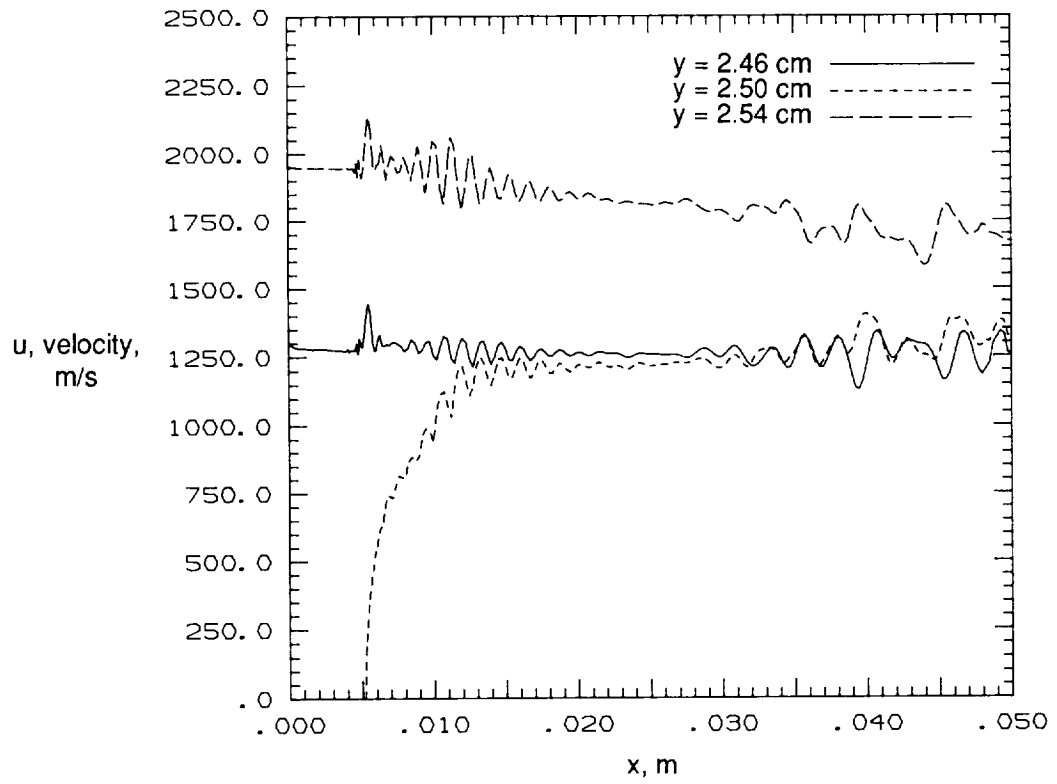
(a) 0.1 ms.

Figure 16. Streamwise velocity versus x at y locations.
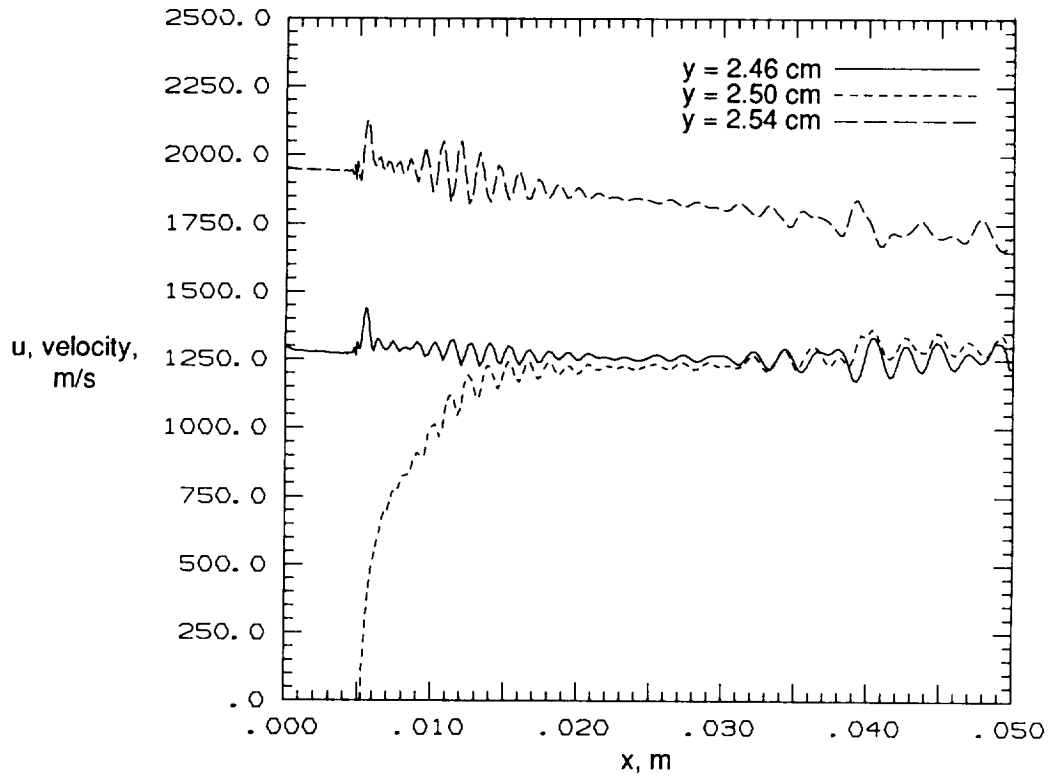
(b) 0.09 ms.

Figure 16. Continued.
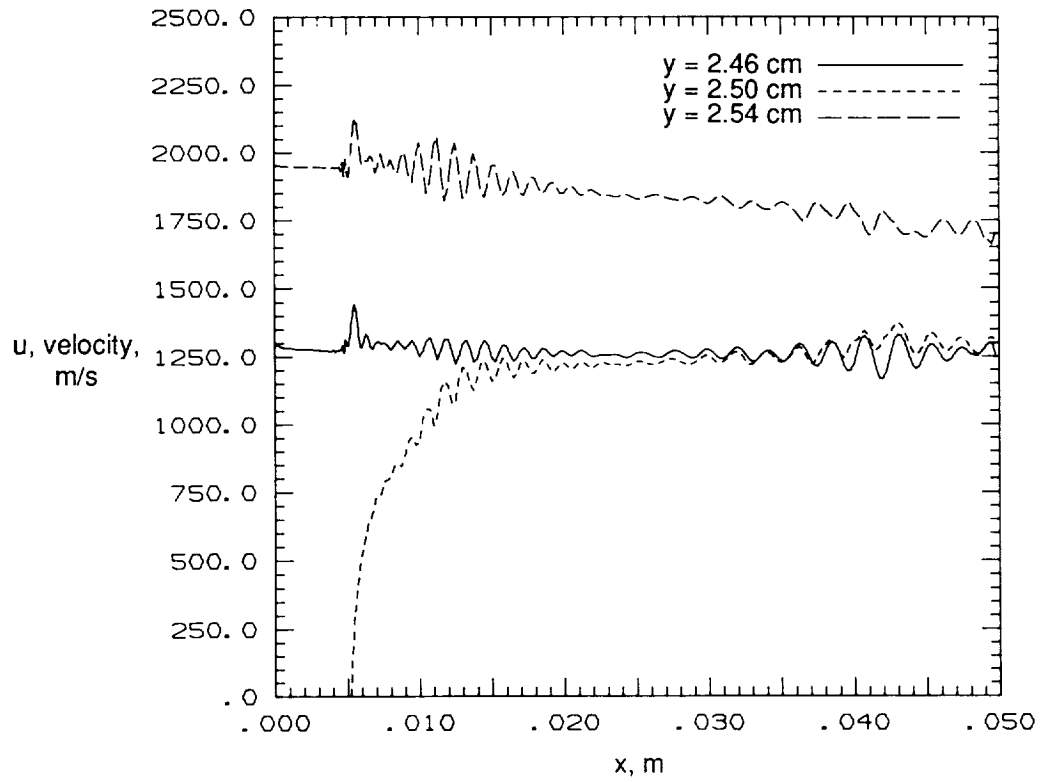
(c) 0.06 ms.

Figure 16. Continued.
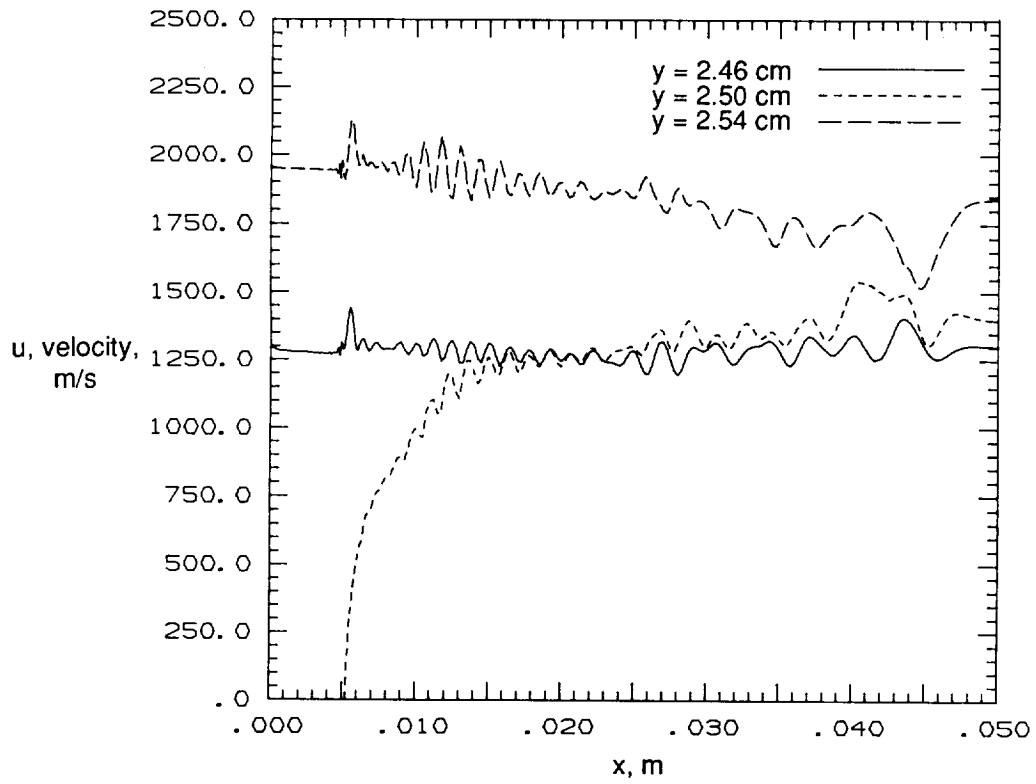
(d) 0.02 ms.

Figure 16. Continued.
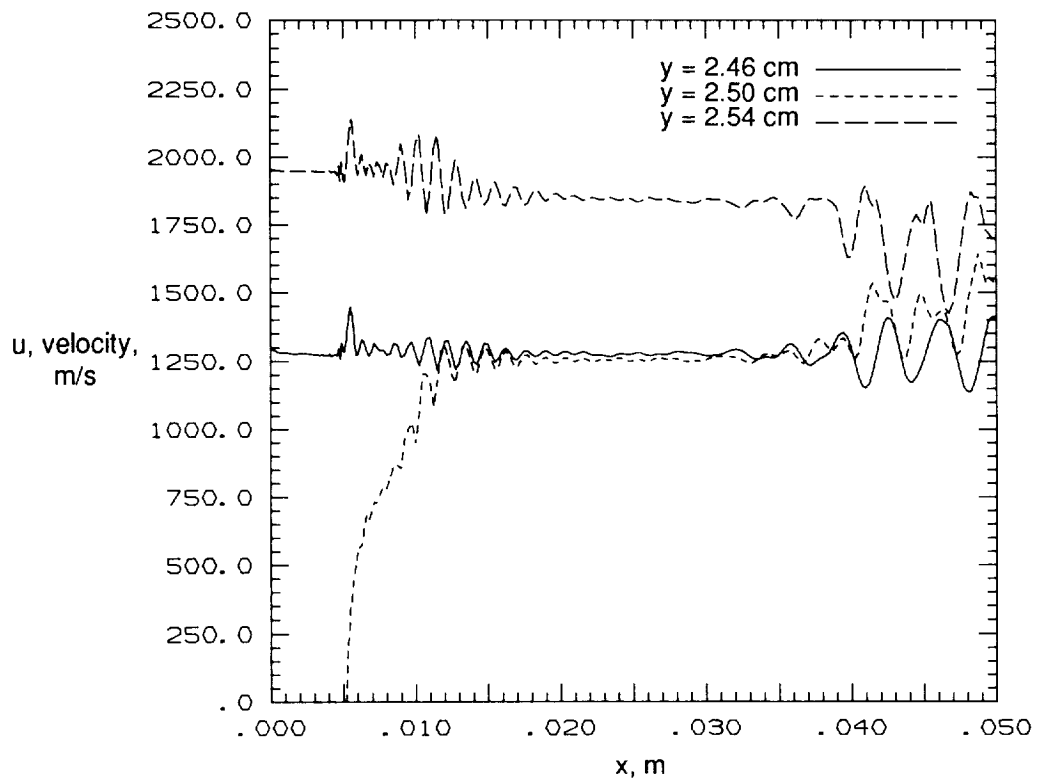
(e) Nonreacting flow (0.1 ms).

Figure 16. Continued.
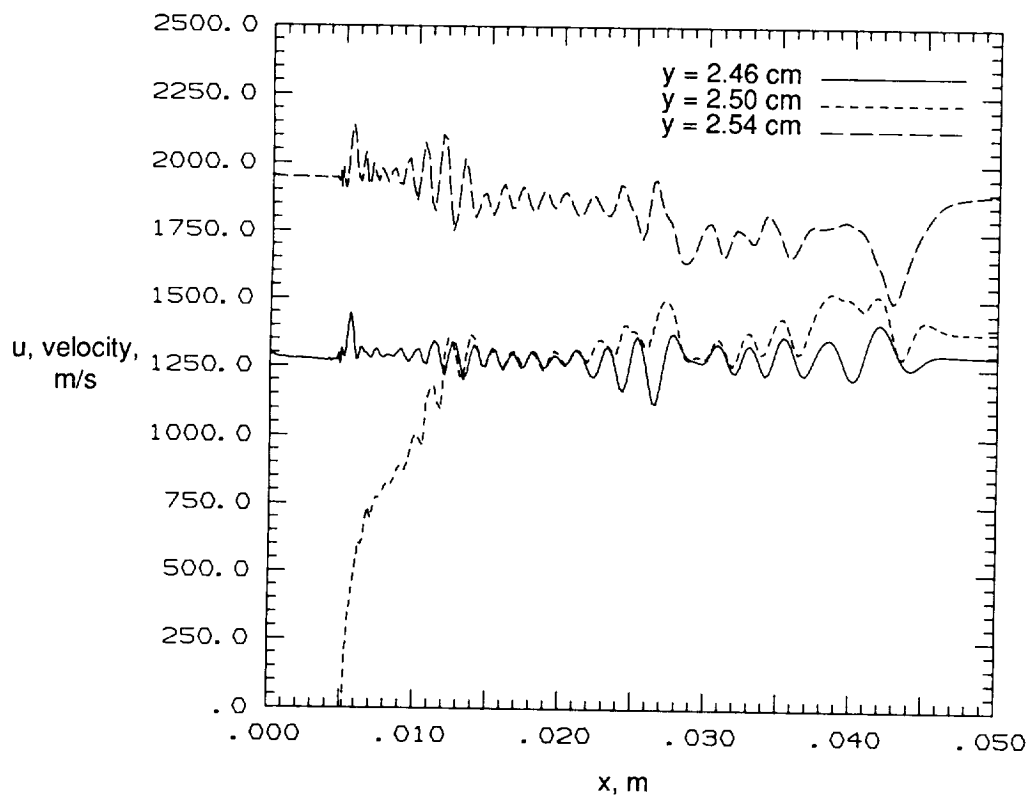
(f) Nonreacting flow (0.02 ms).

Figure 16. Concluded.
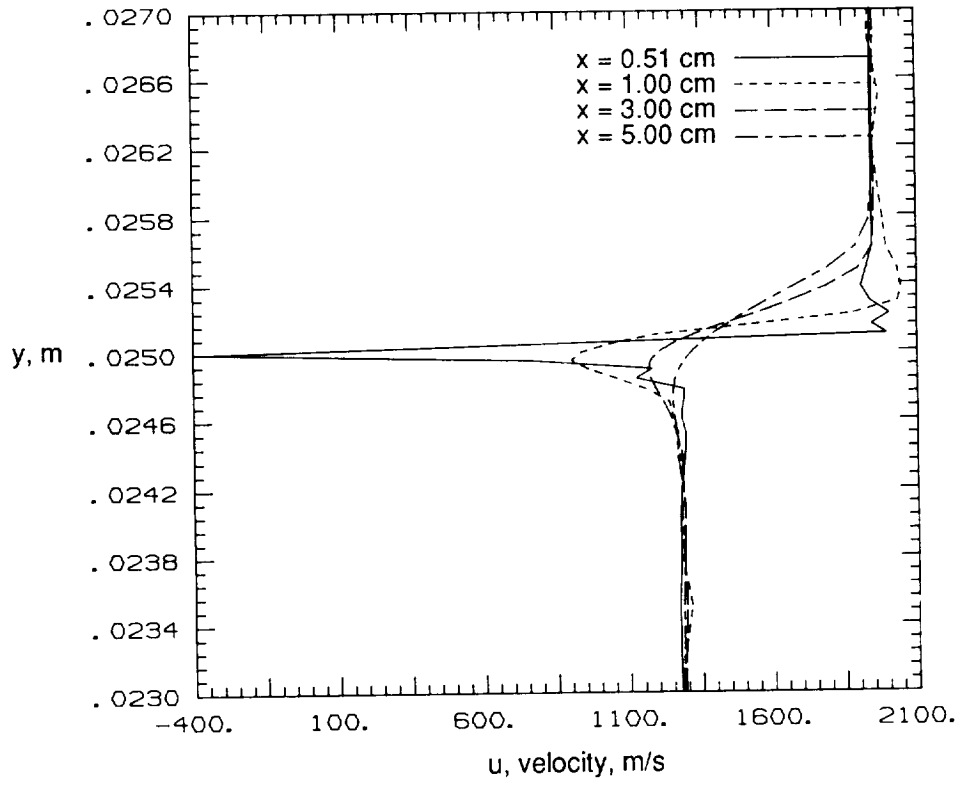
Figure 17. Streamwise velocity versus y at x locations.
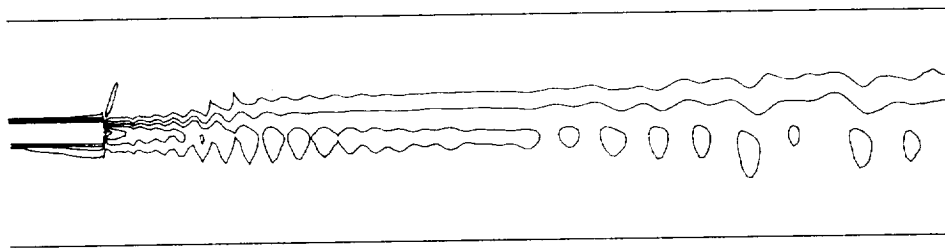
Figure 18. Streamwise velocity contours in mixing layer.
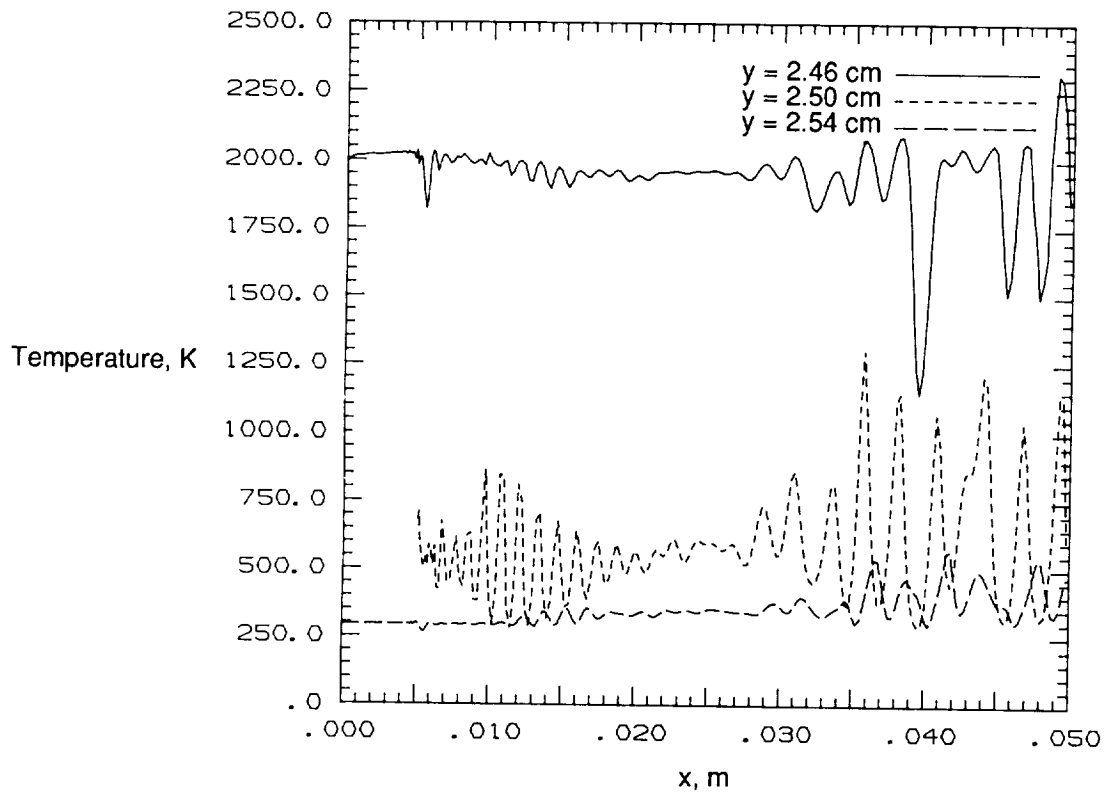
Figure 19. Temperature versus x at y locations.
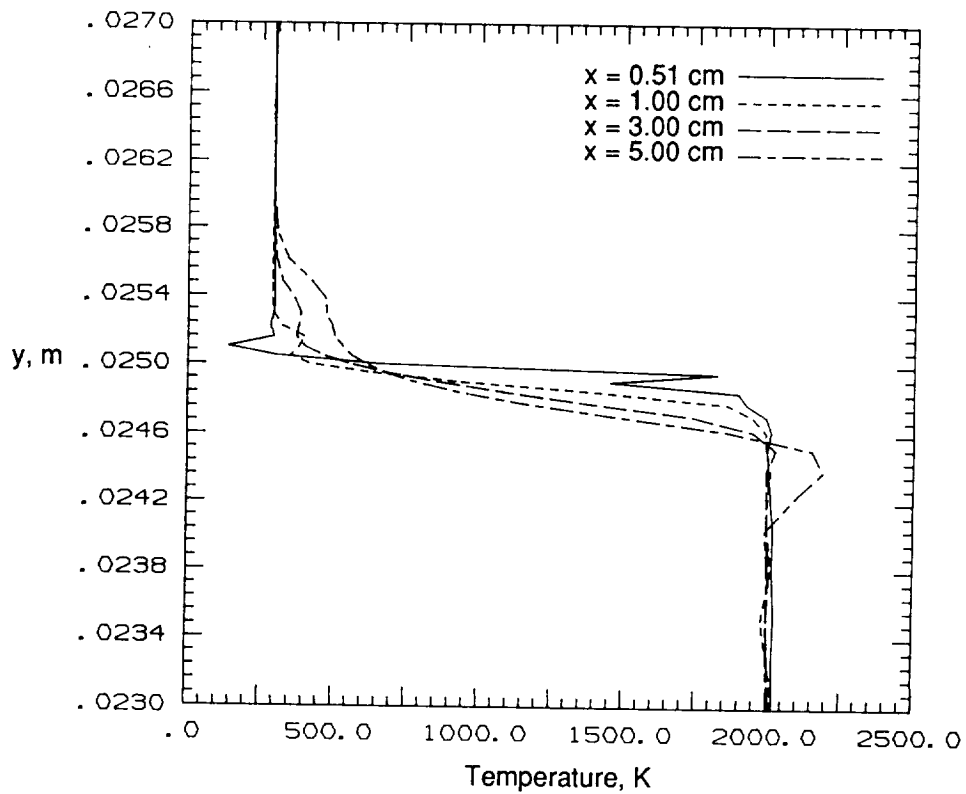
Figure 20. Temperature versus y at x locations.
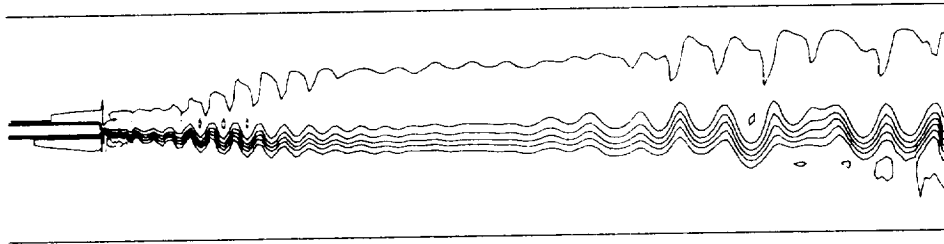
Figure 21. Temperature contours in mixing layer.
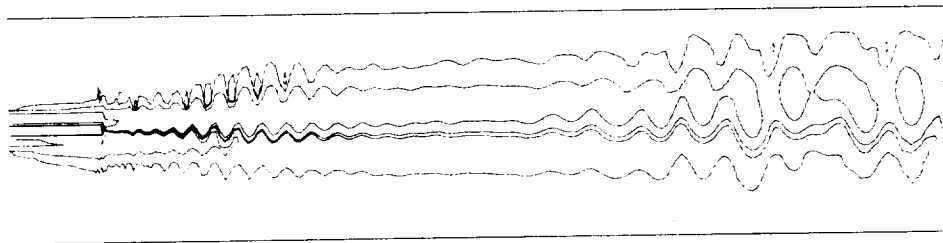
Figure 22. Vorticity contours in mixing layer.
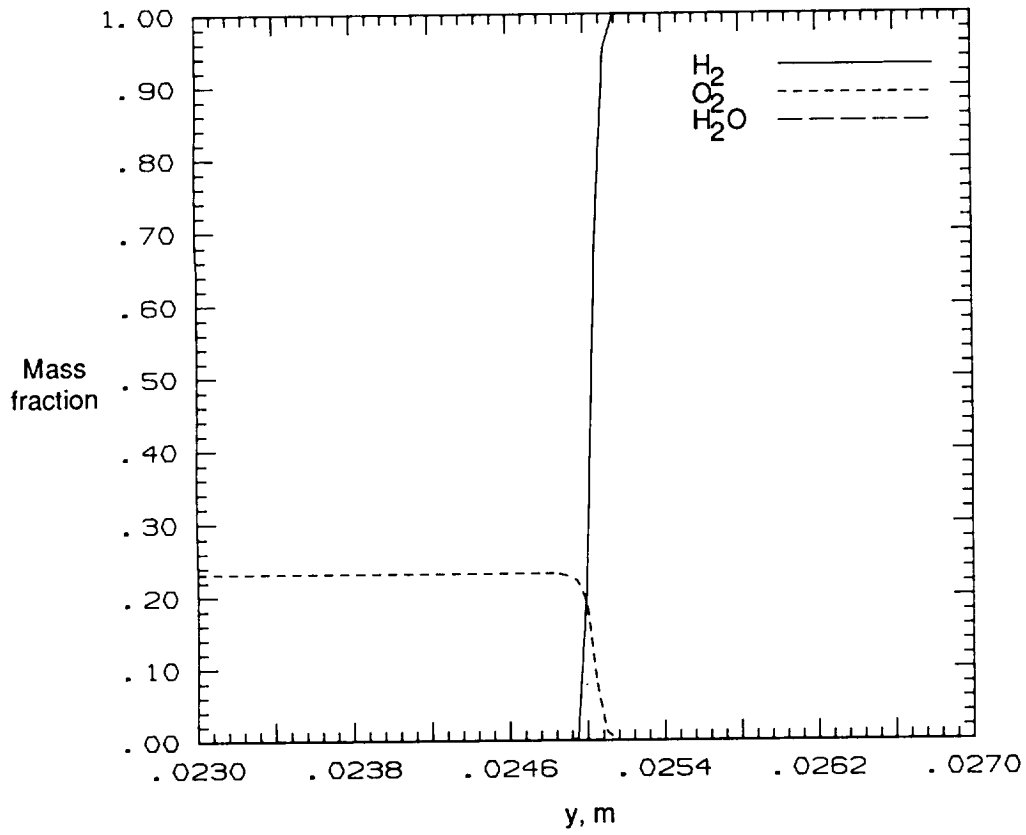
(a) Major species.

Figure 23. Mass fraction versus y at $x = 0.51$ cm.
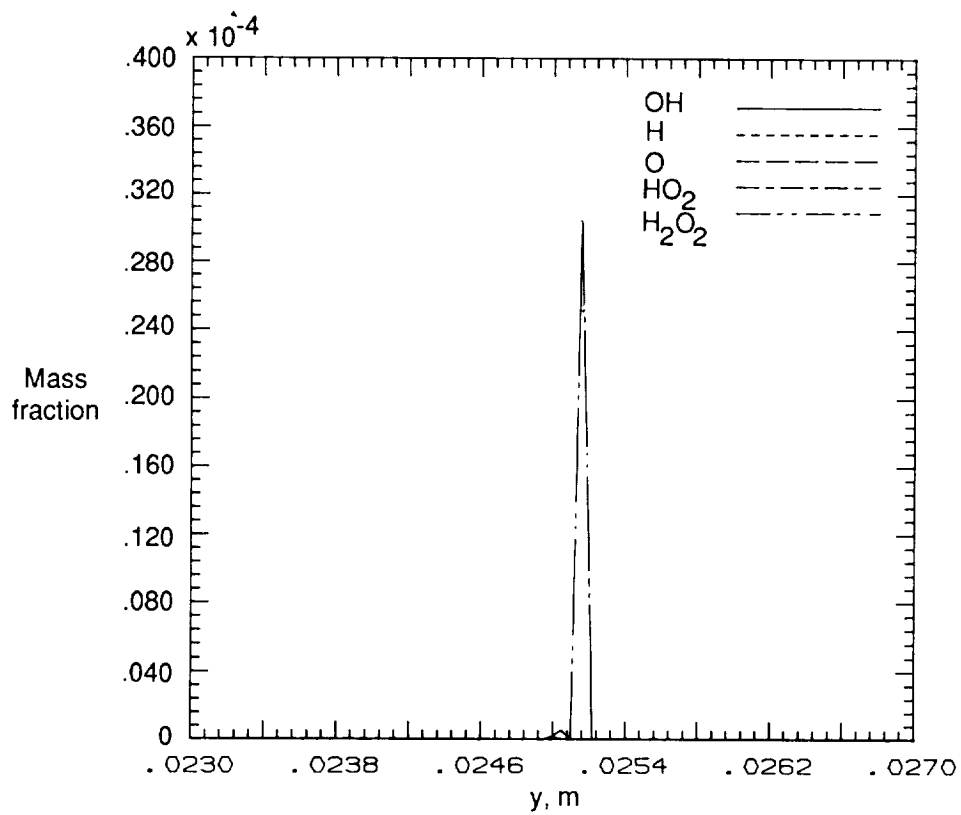
(b) Minor species.

Figure 23. Concluded.
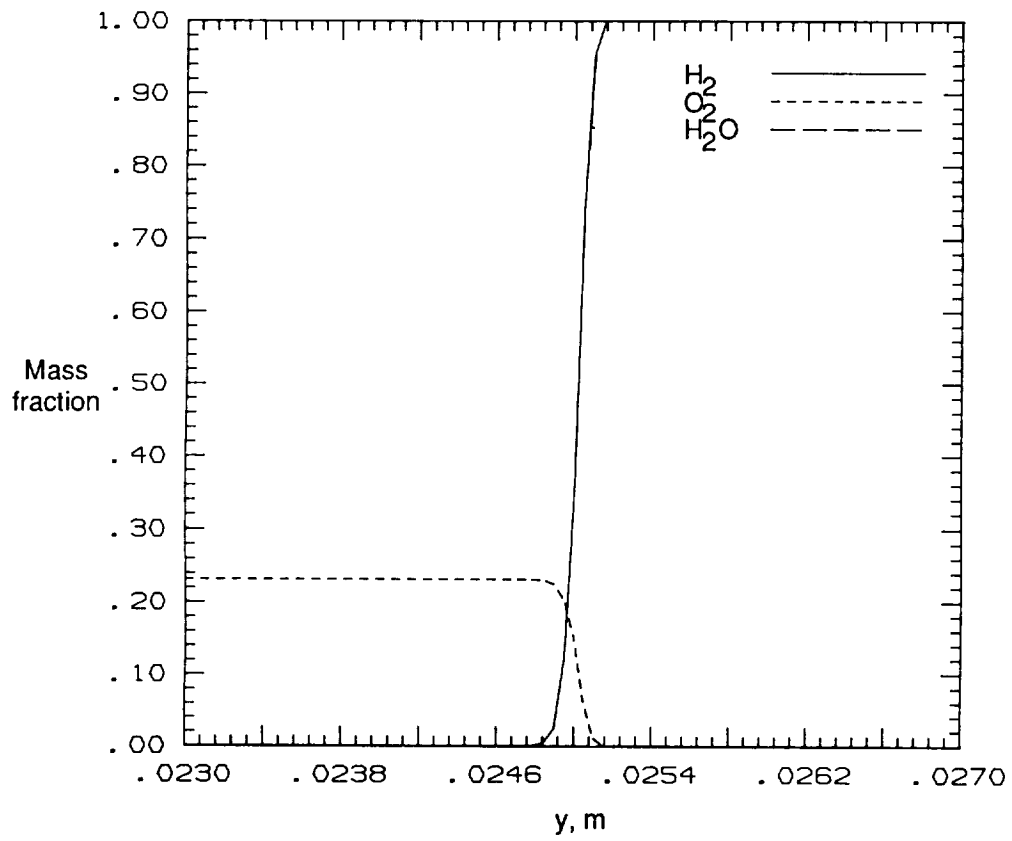
(a) Major species.

Figure 24. Mass fraction versus y at $x = 0.58$ cm.
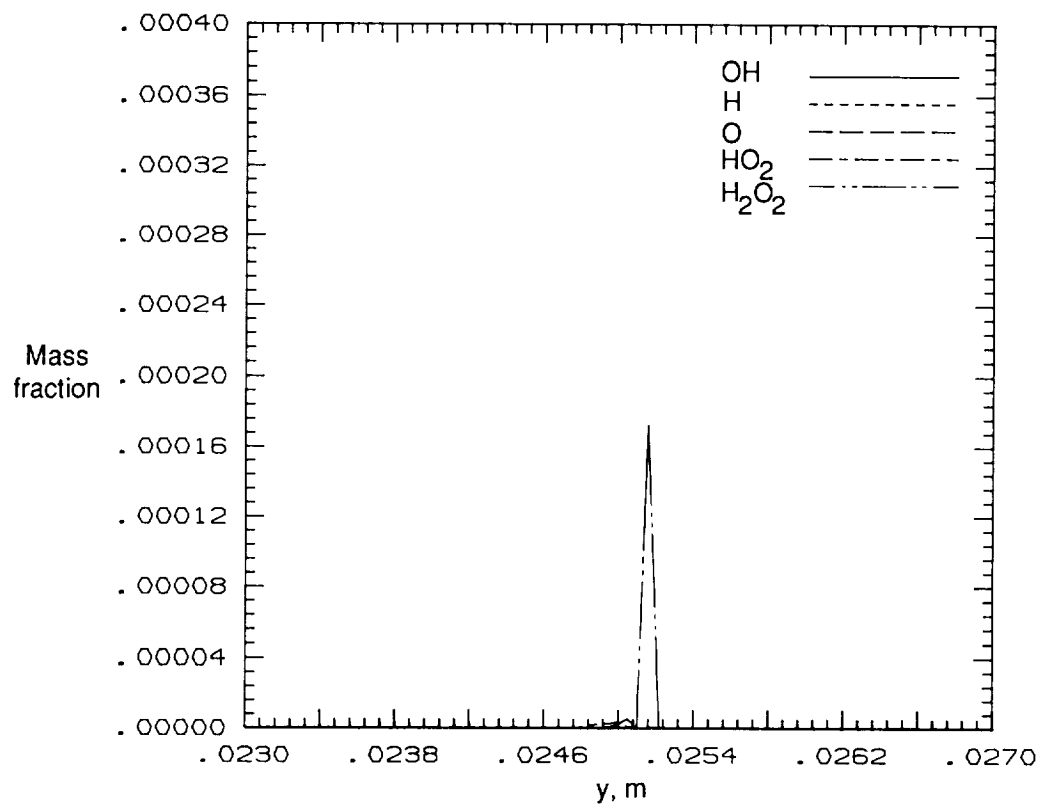
(b) Minor species.

Figure 24. Concluded.
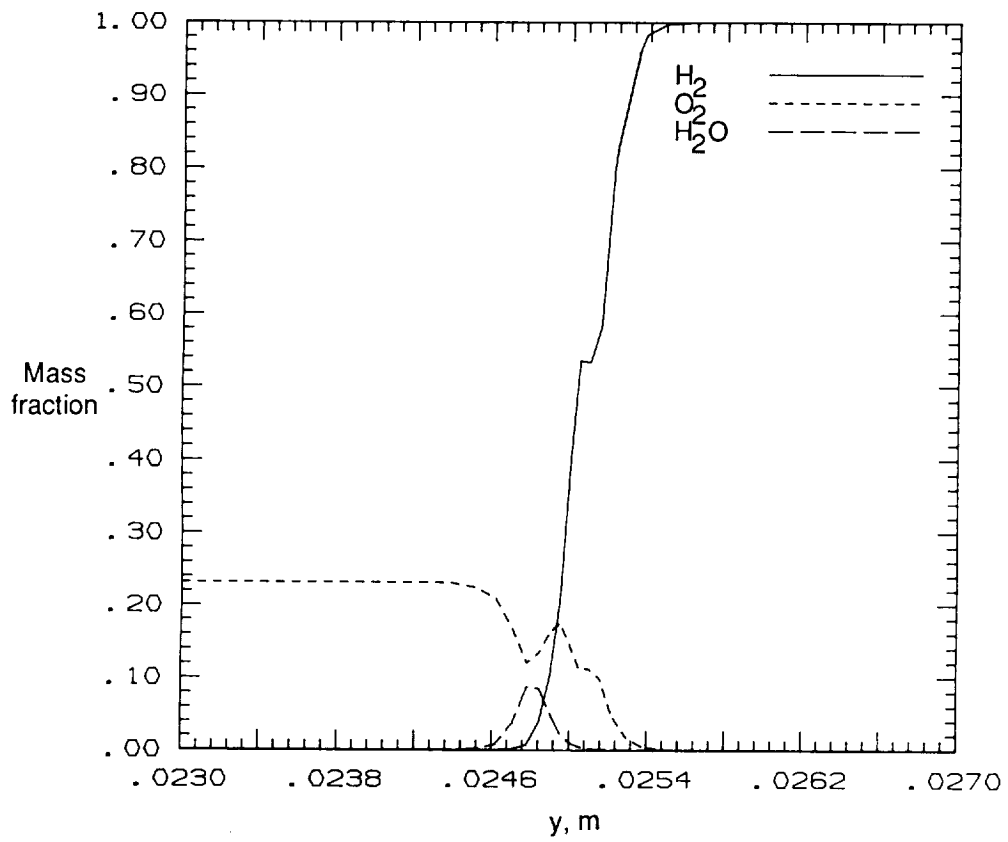
(a) Major species.

Figure 25. Mass fraction versus y at $x = 1.0$ cm.
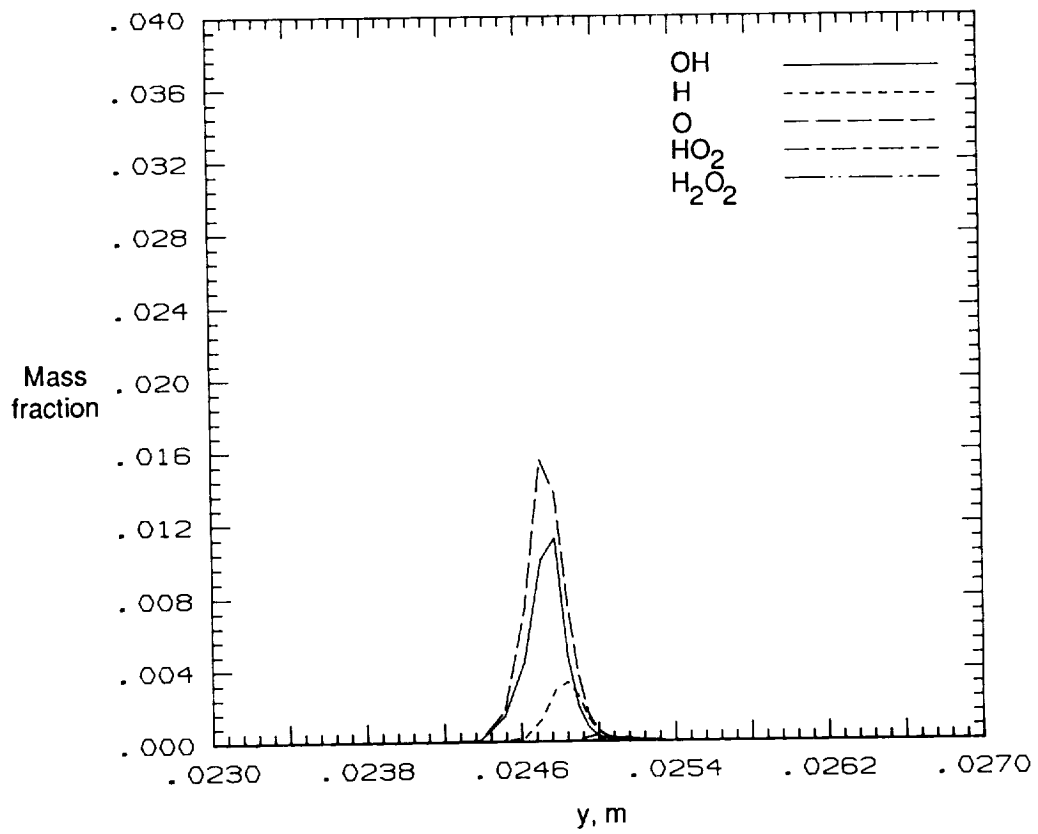
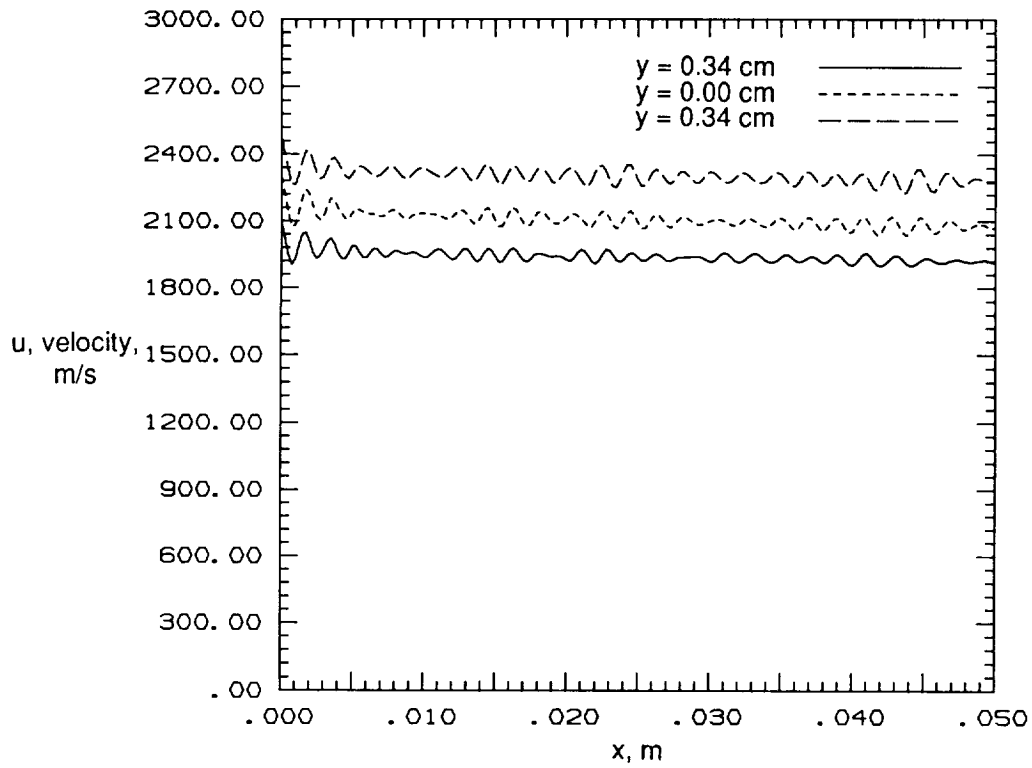(b) Minor species.

Figure 25. Concluded.
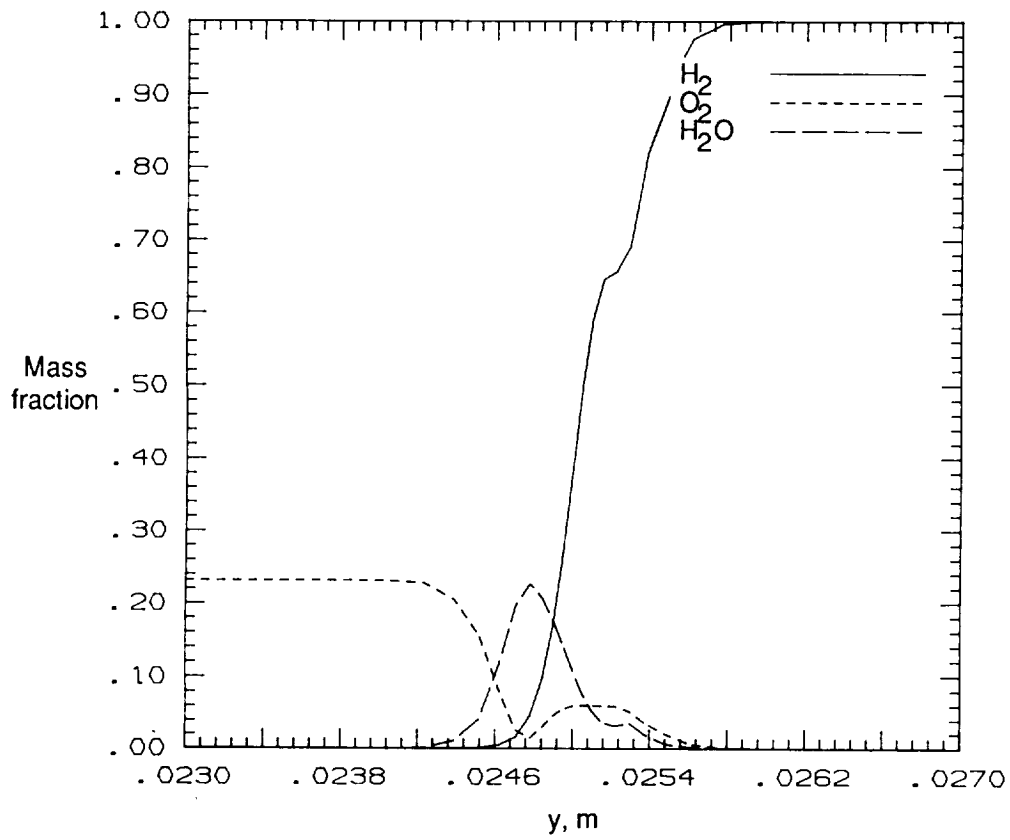
(a) Major species.

Figure 26. Mass fraction versus y at $x = 2.0$ cm.
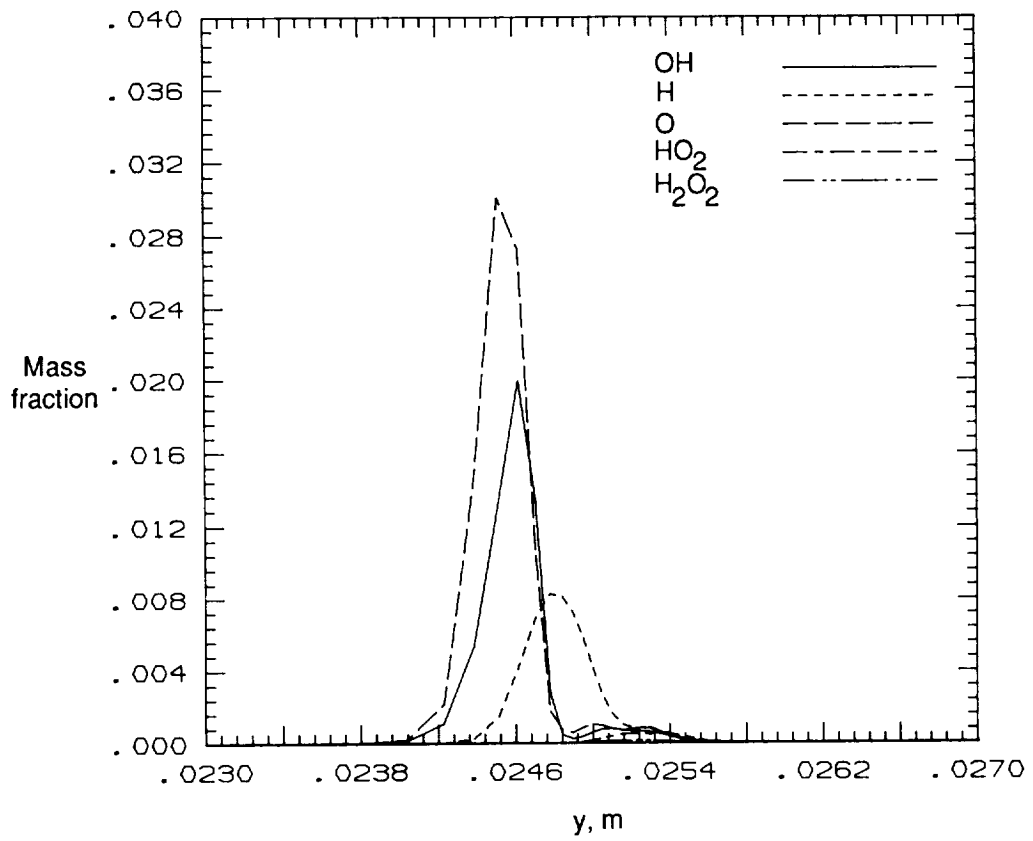
(b) Minor species.

Figure 26. Concluded.
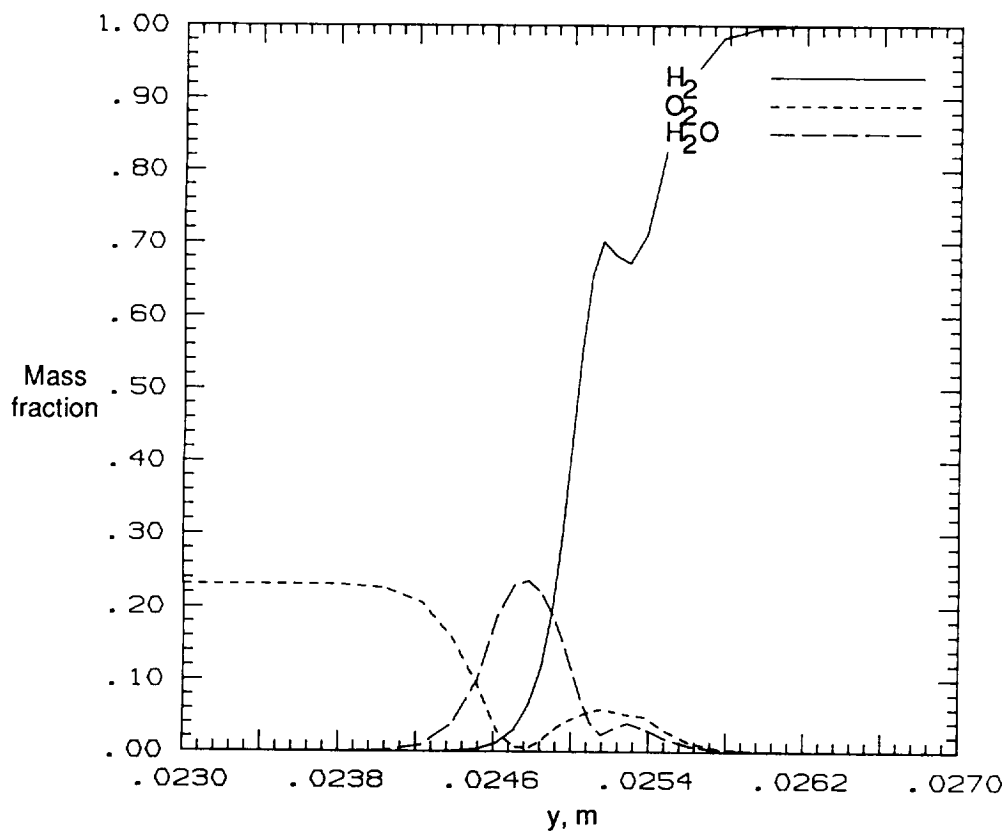
(a) Major species.

Figure 27. Mass fraction versus y at $x = 3.0$ cm.
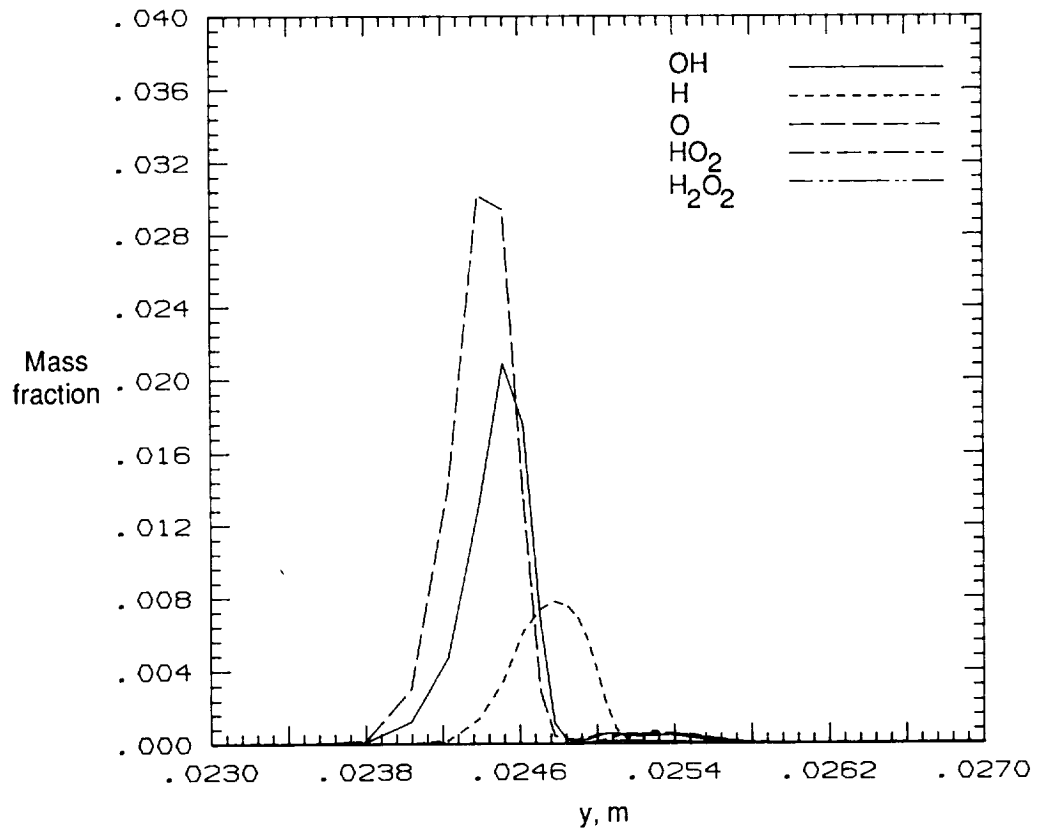
(b) Minor species.

Figure 27. Concluded.
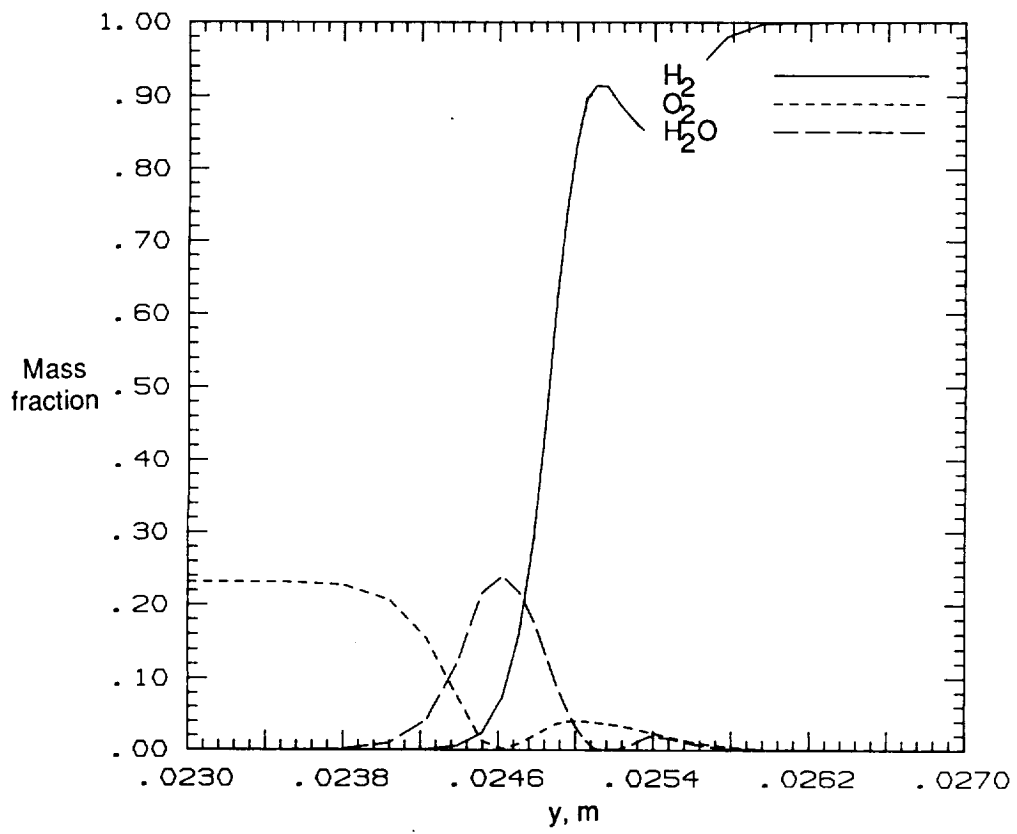
(a) Major species.

Figure 28. Mass fraction versus y at $x = 4.0$ cm.
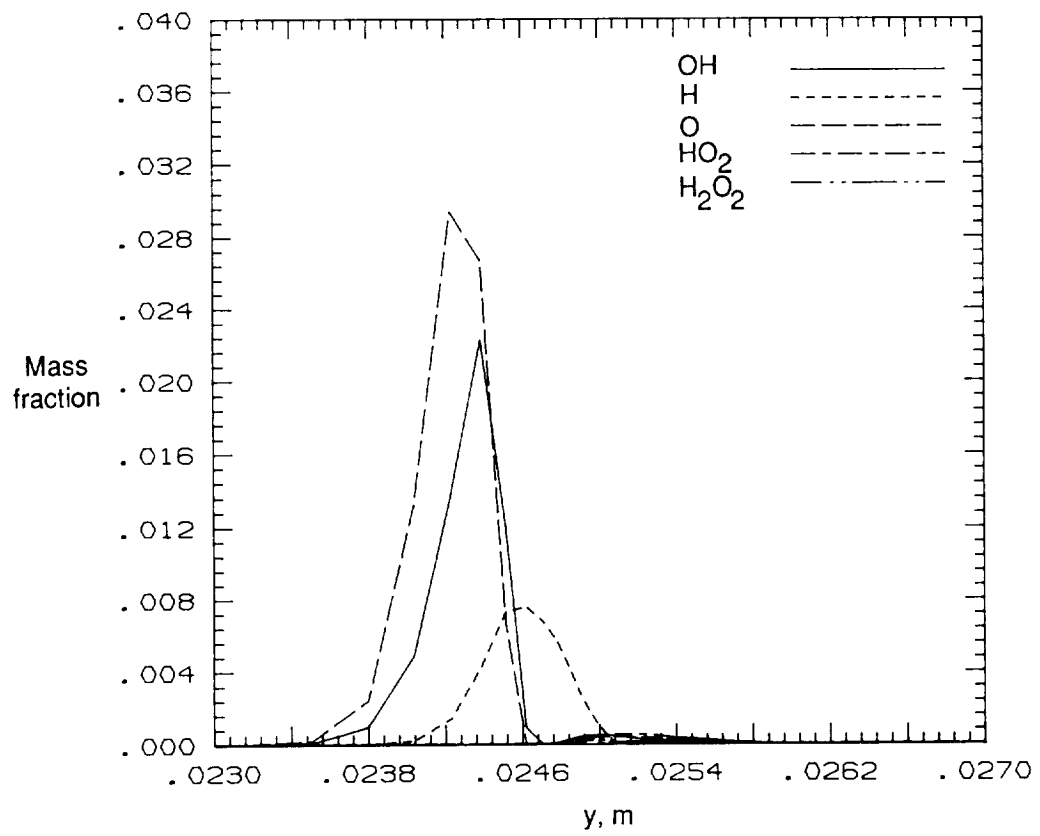
(b) Minor species.

Figure 28. Concluded.
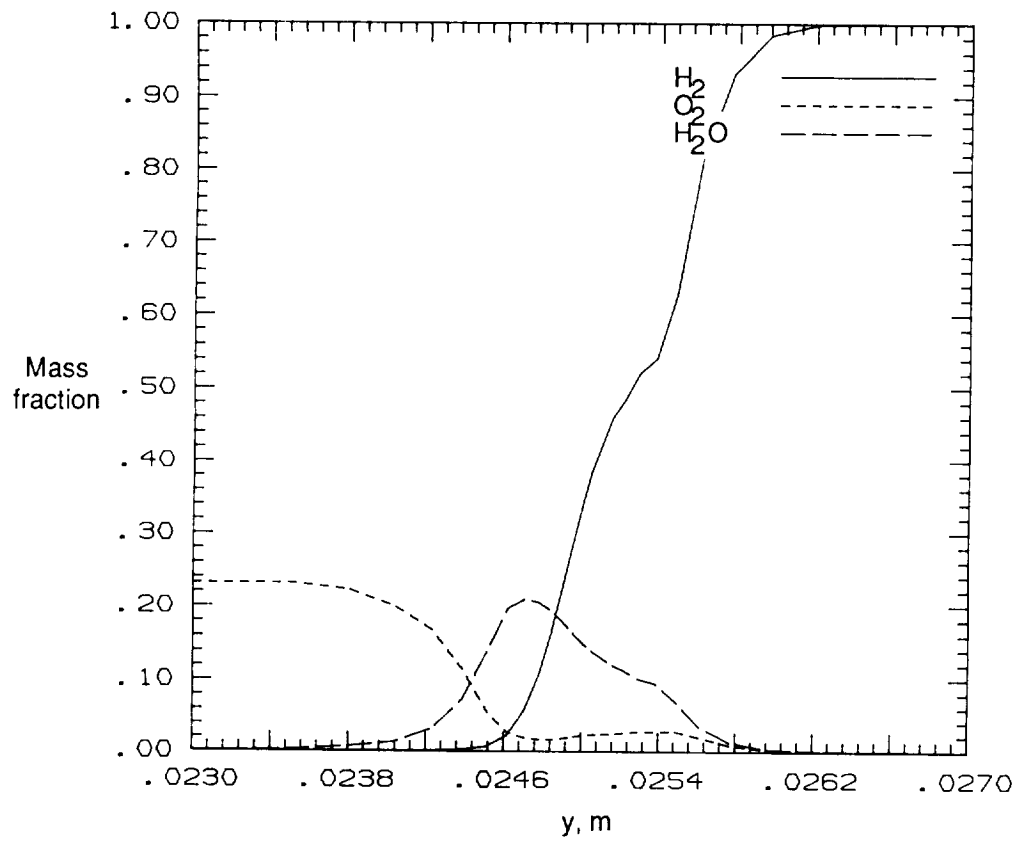
(a) Major species.

Figure 29. Mass fraction versus y at $x = 5.0$ cm.
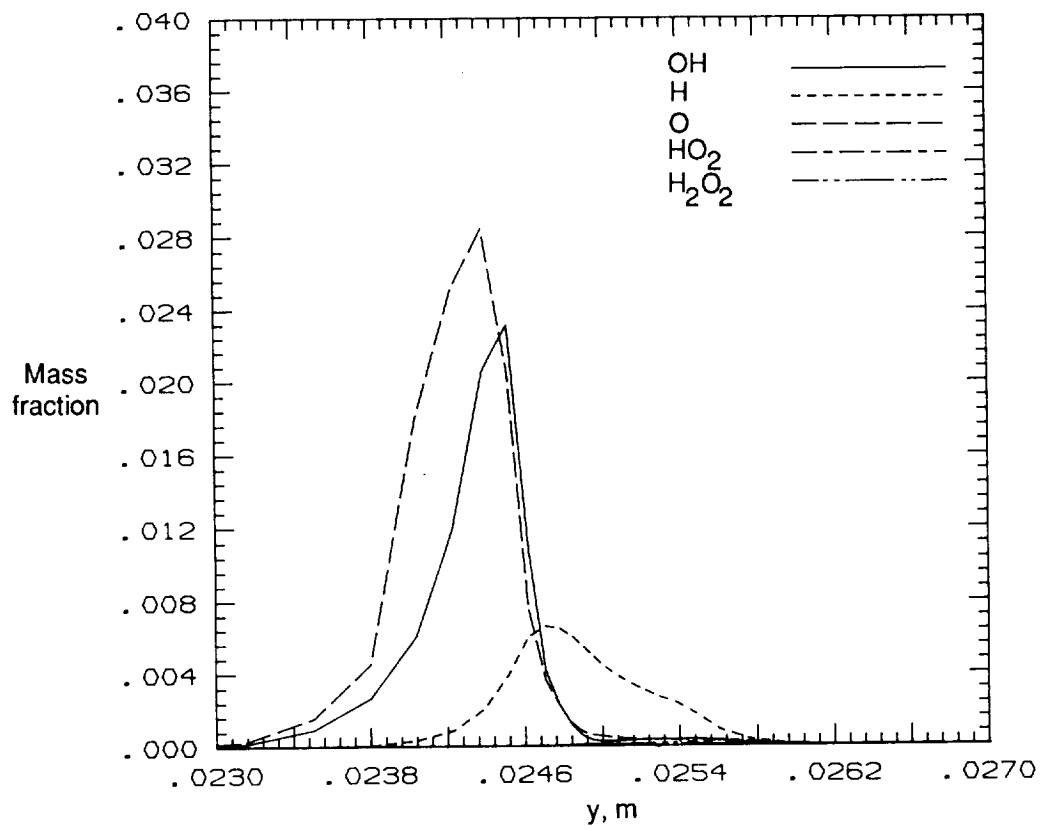
(b) Minor species.

Figure 29. Concluded.
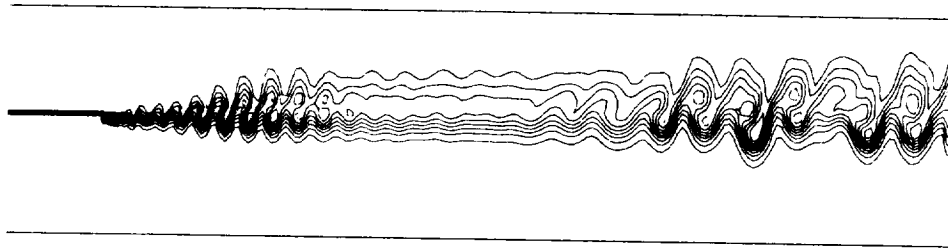
Figure 30. Hydrogen mass fraction contours in mixing layer.
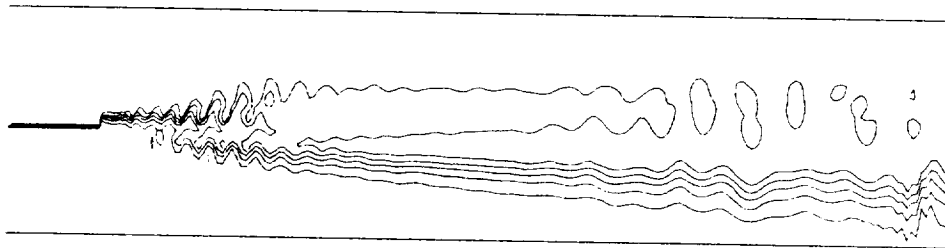
Figure 31. Oxygen mass fraction contours in mixing layer.
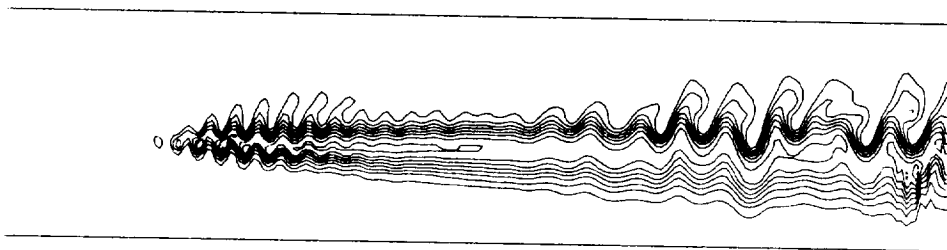
Figure 32. Atomic hydrogen (H) mass fraction contours in mixing layer.
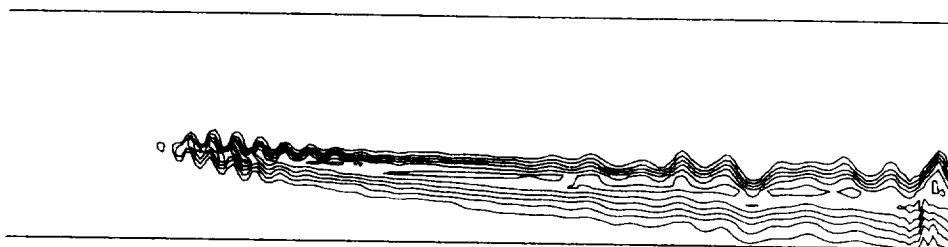
Figure 33. Atomic oxygen (O) mass fraction contours in mixing layer.
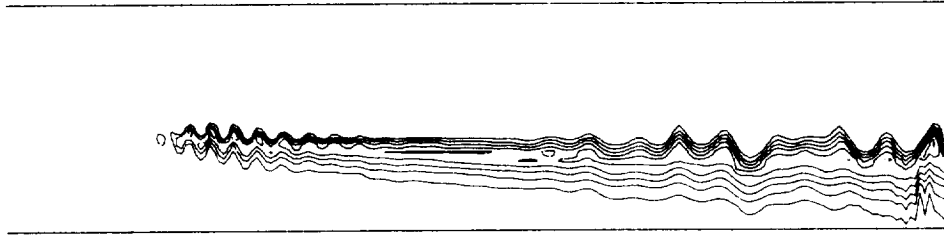
Figure 34. Hydroxyl (OH) mass fraction contours in mixing layer.
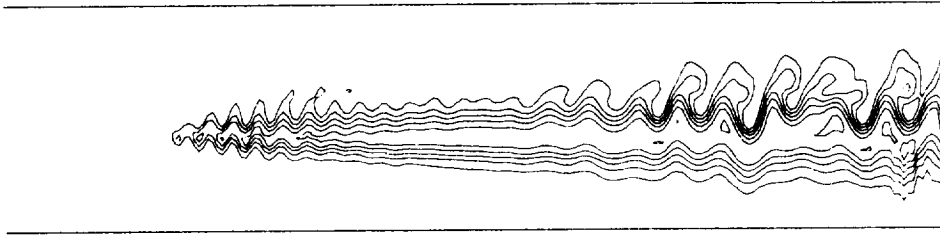
Figure 35. Water mass fraction contours in mixing layer.
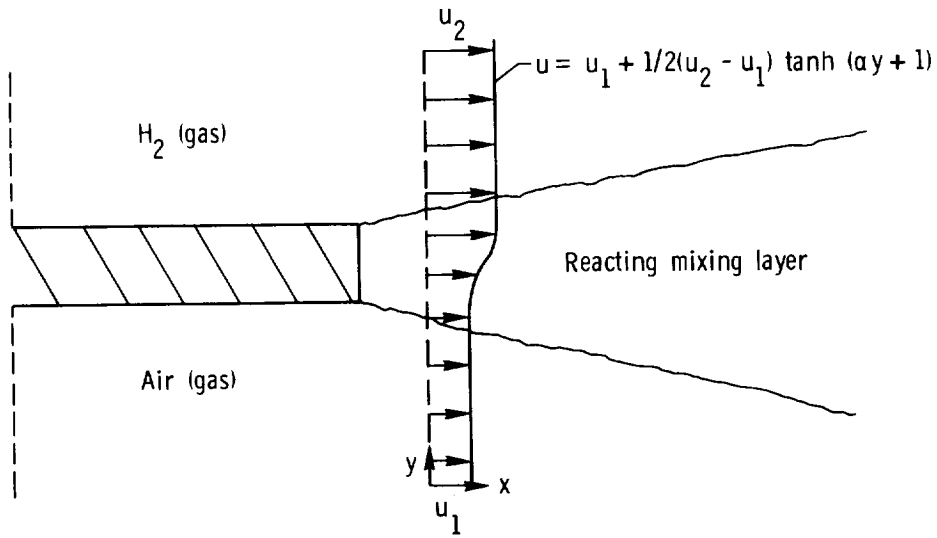
Figure 36. Reacting mixing layer schematic for spectral calculations.
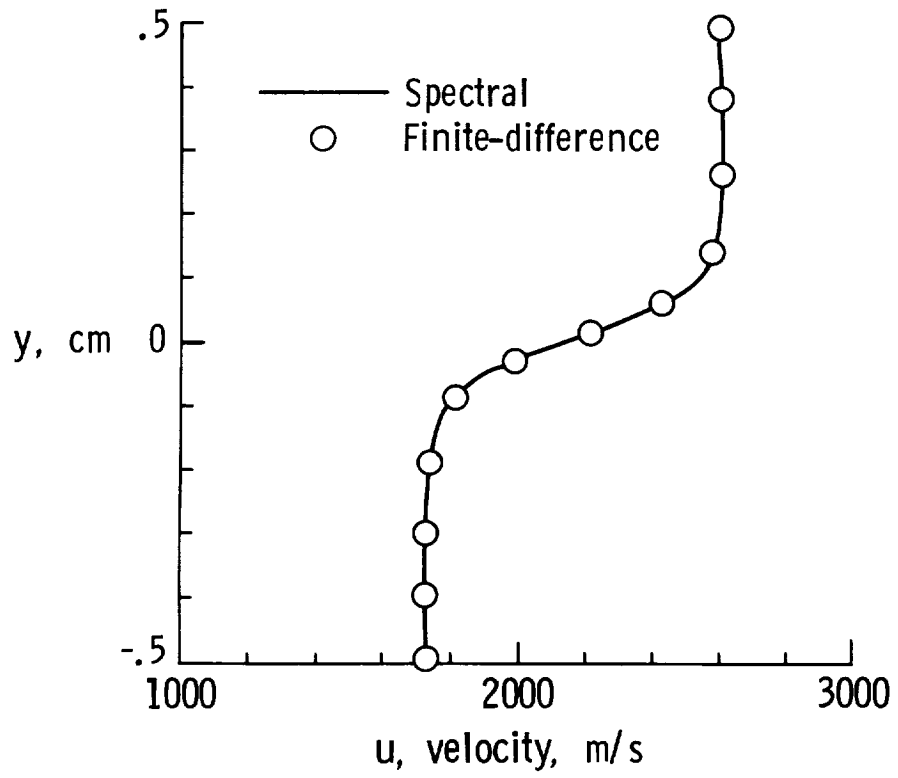
Figure 37. Streamwise velocity versus y.
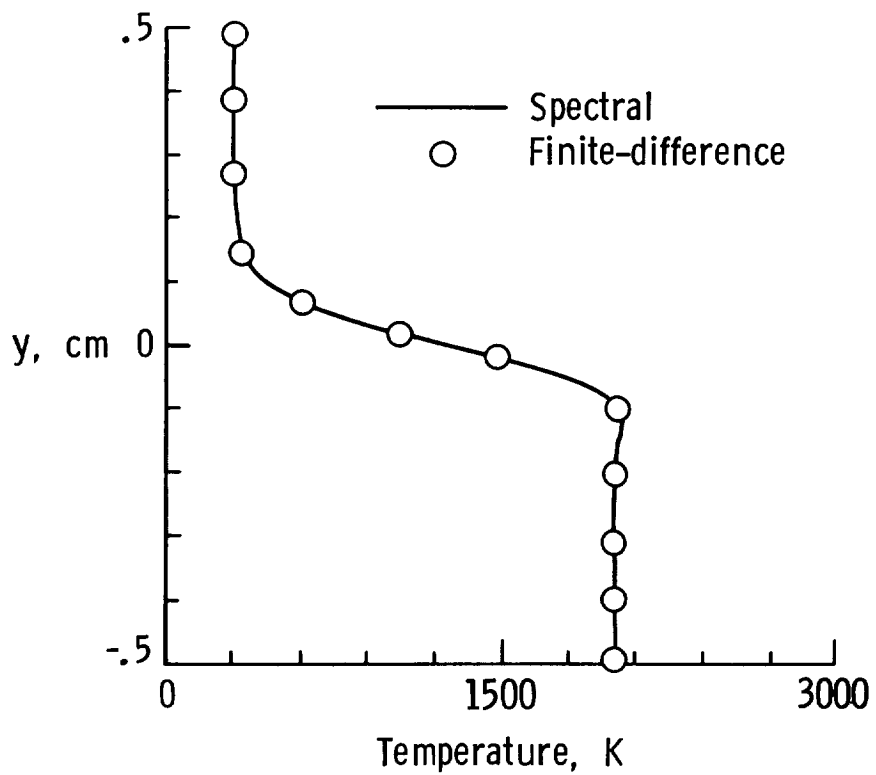

Figure 38. Temperature versus y.
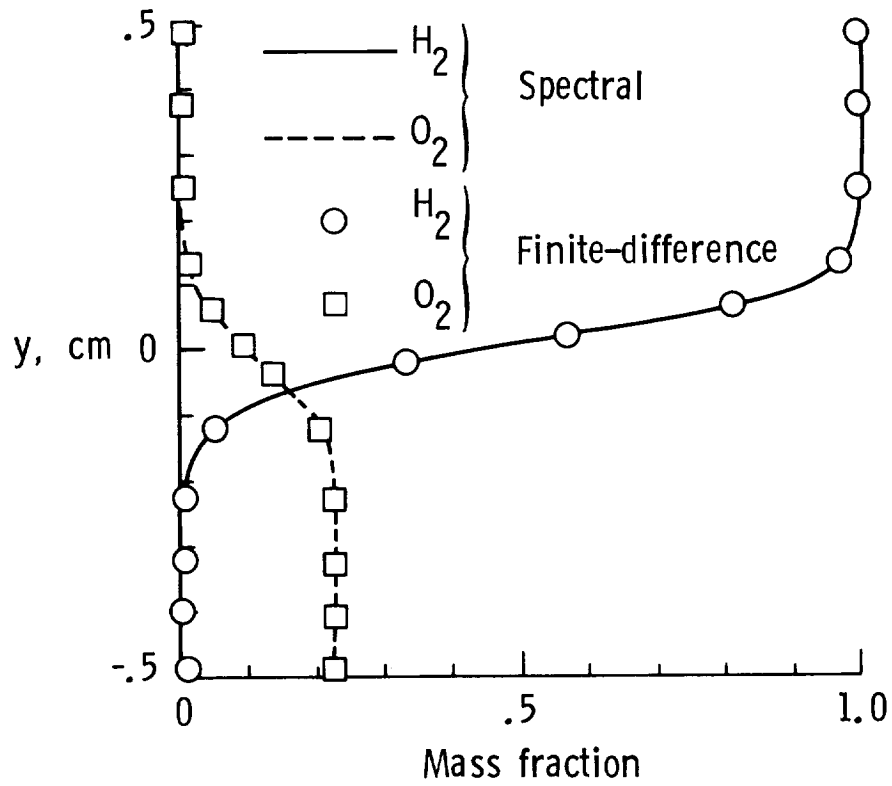
Figure 39. Hydrogen and oxygen mass fraction versus y.
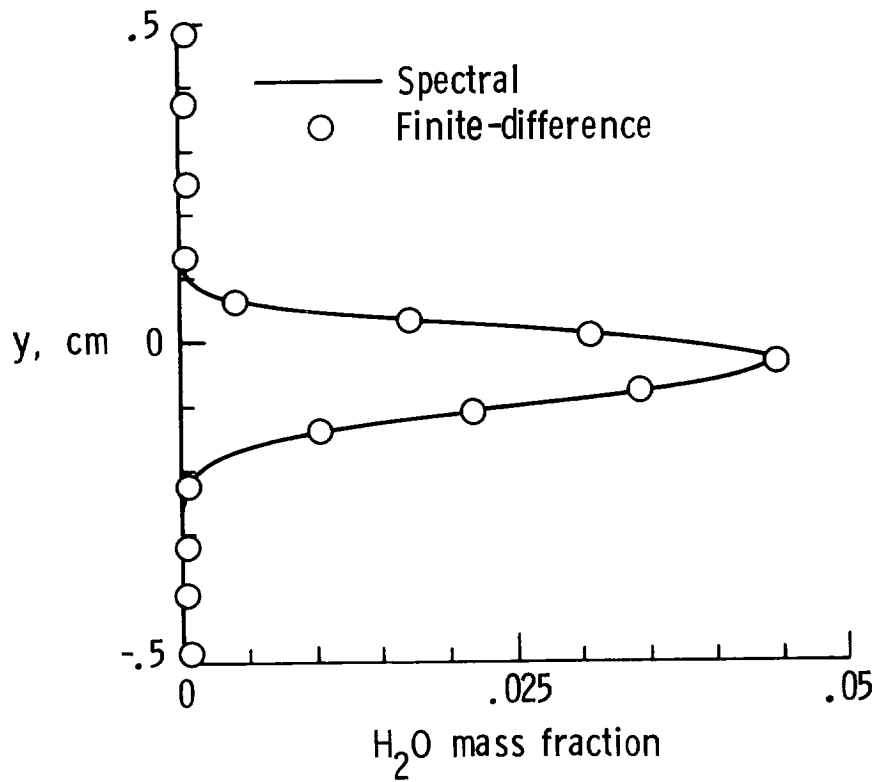
Figure 40. Water mass fraction versus y.
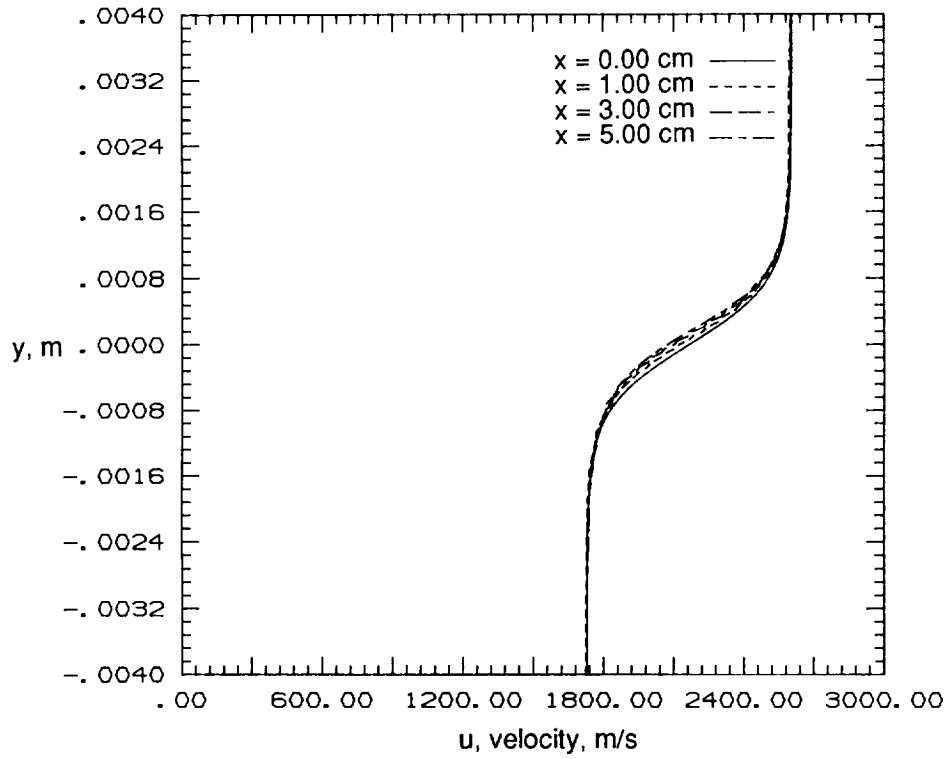
Figure 41. Streamwise velocity versus y at x locations from spectral program.
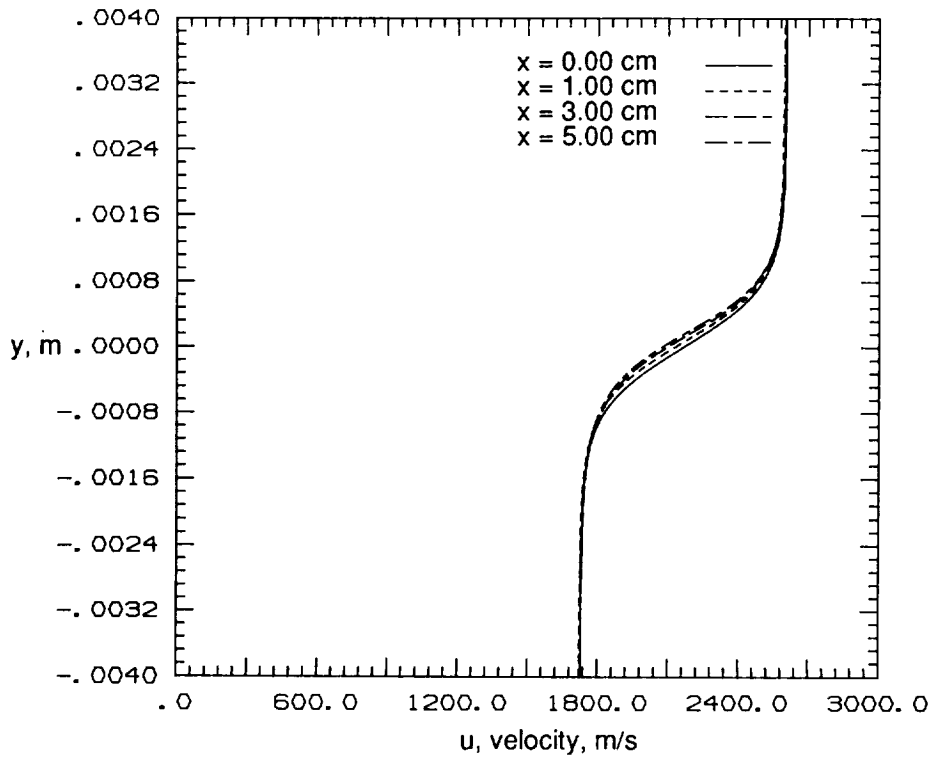
Figure 42. Streamwise velocity versus y at x locations from spectral program with Laplacian filtering.
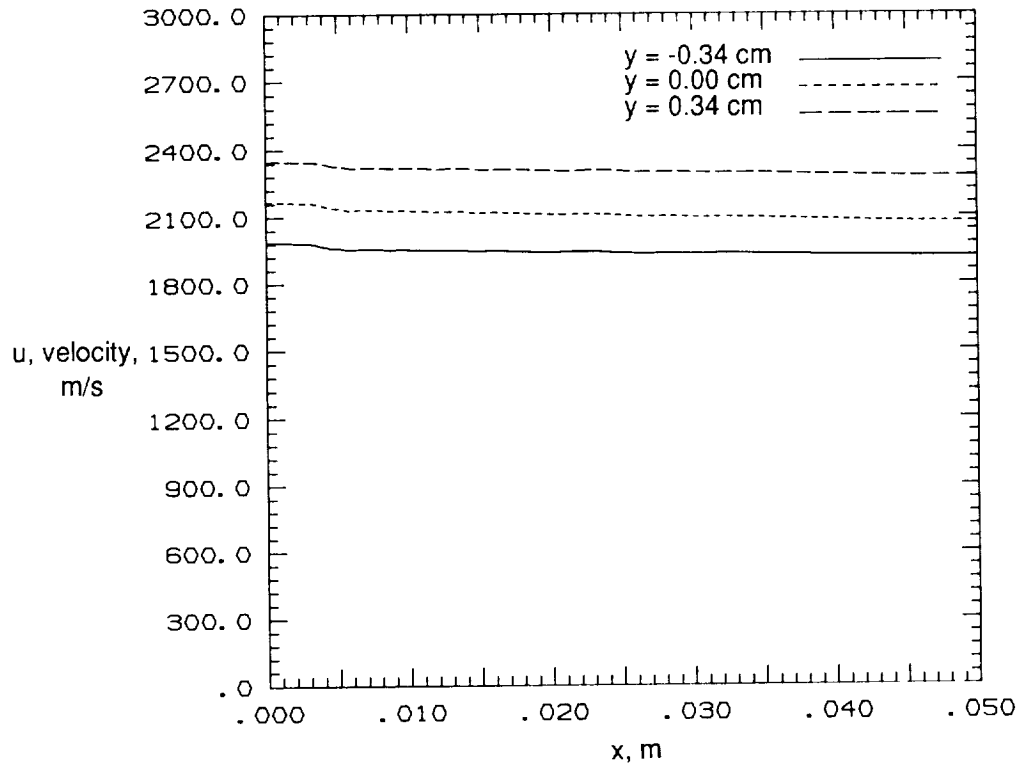
Figure 43. Streamwise velocity versus x at y locations from spectral program.
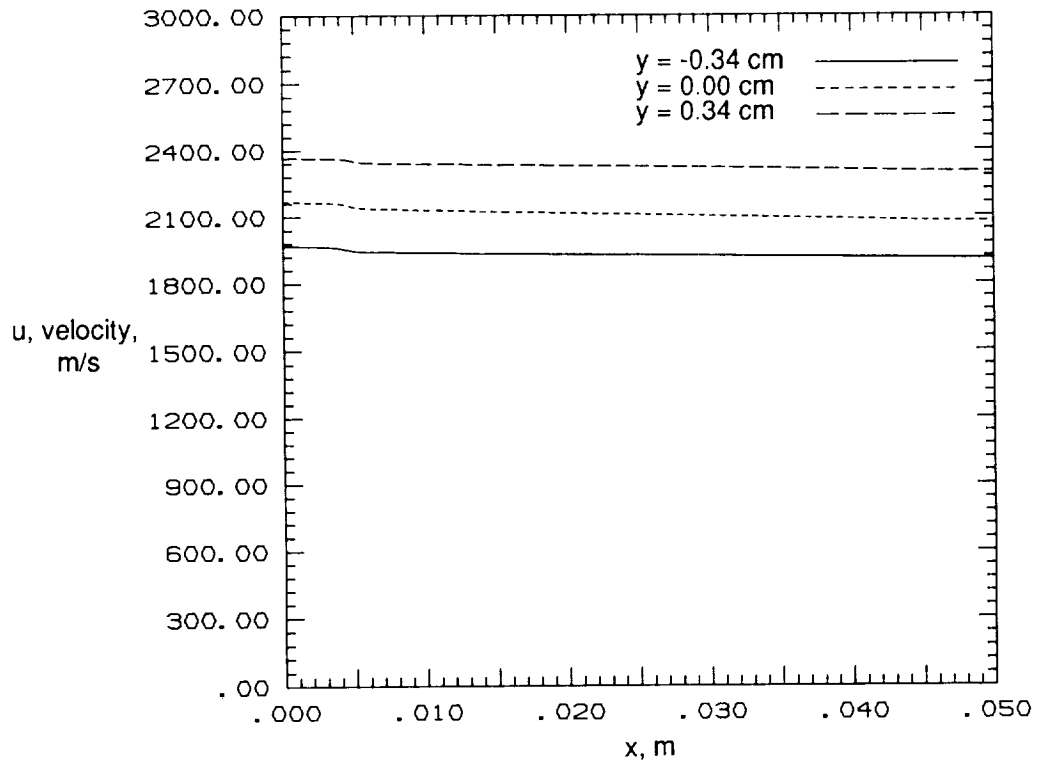
Figure 44. Streamwise velocity versus x at y locations from finite-difference program.
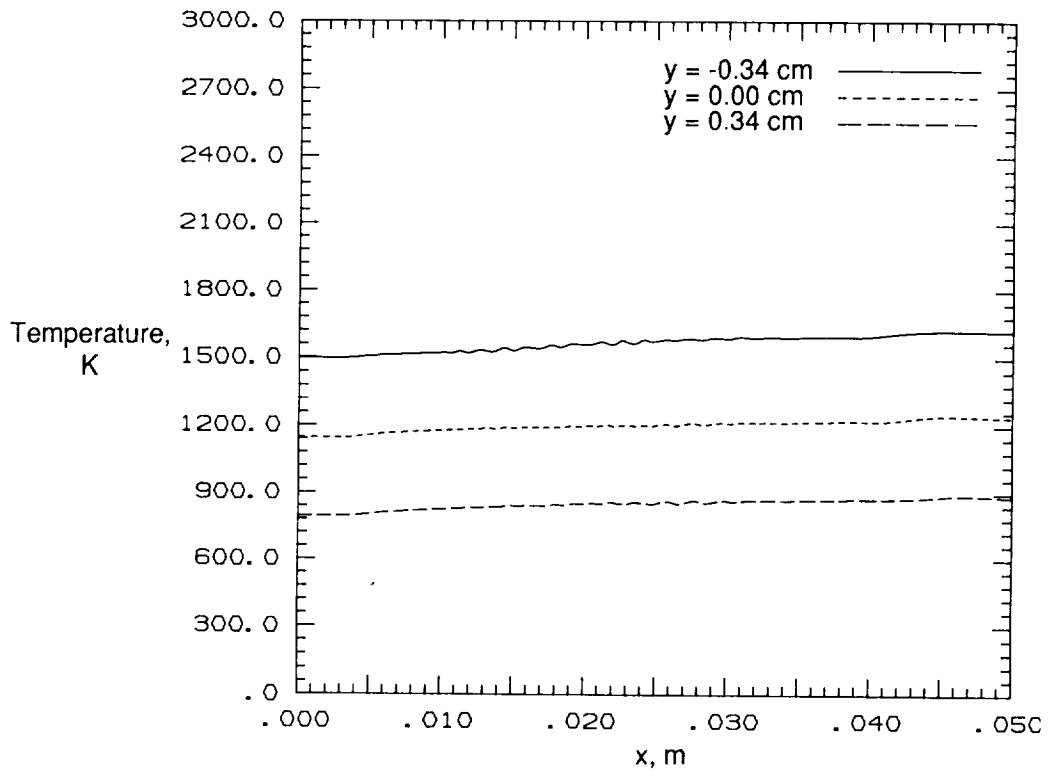
Figure 45. Temperature versus x at y locations.
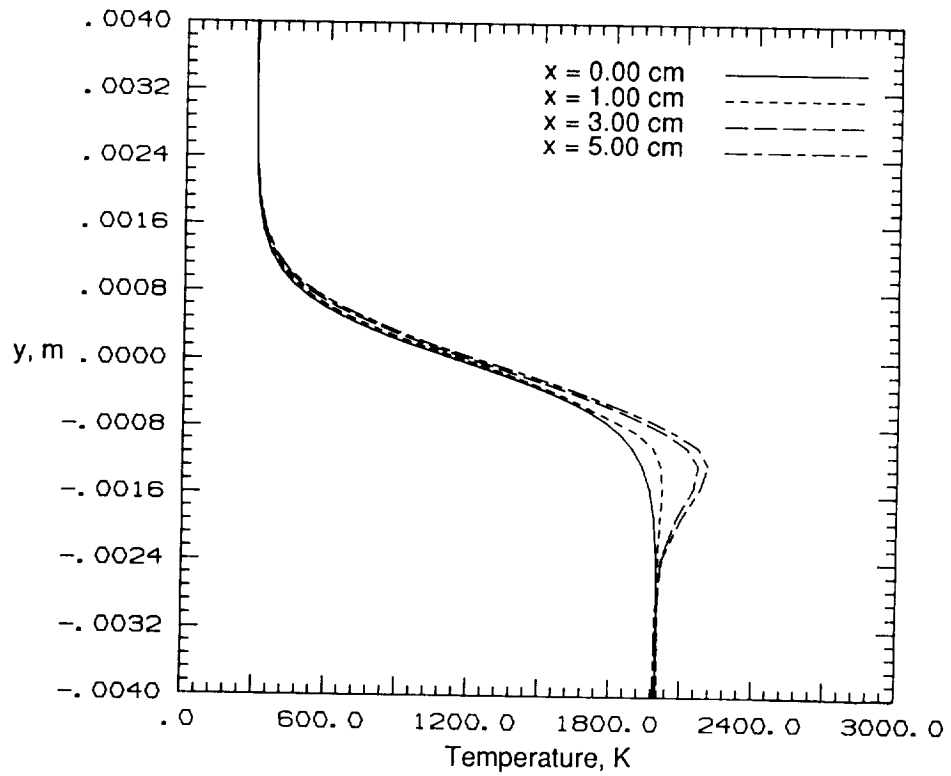
Figure 46. Temperature versus y at x locations.
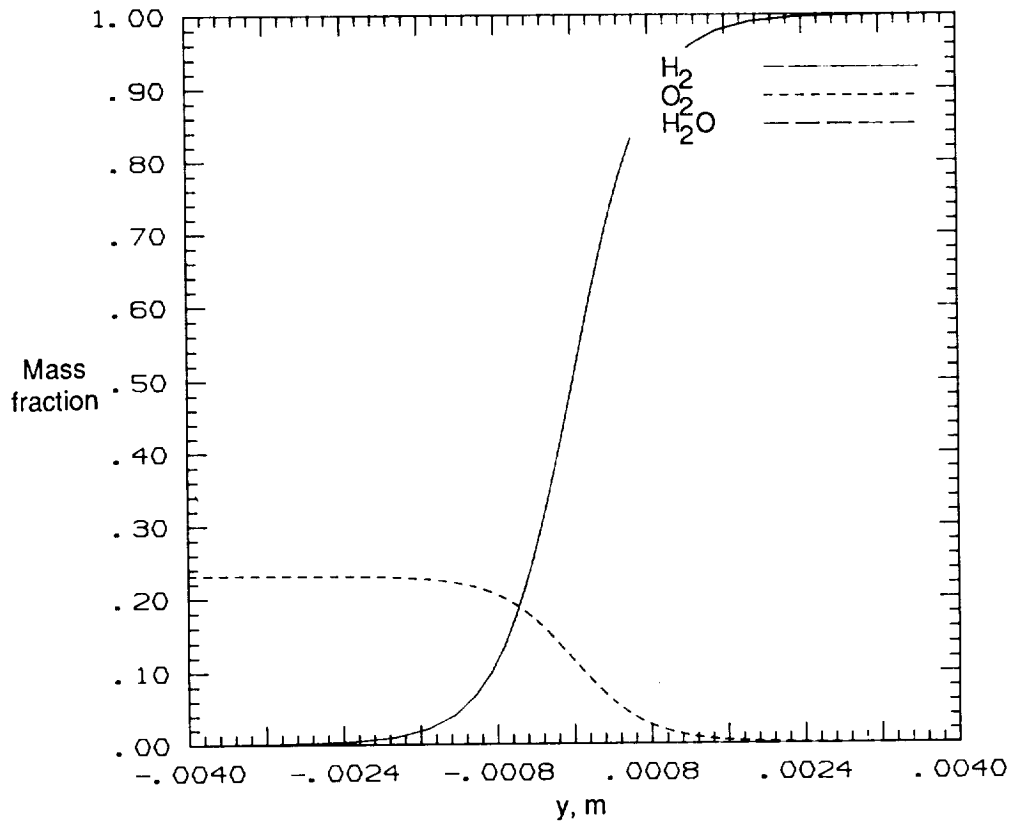
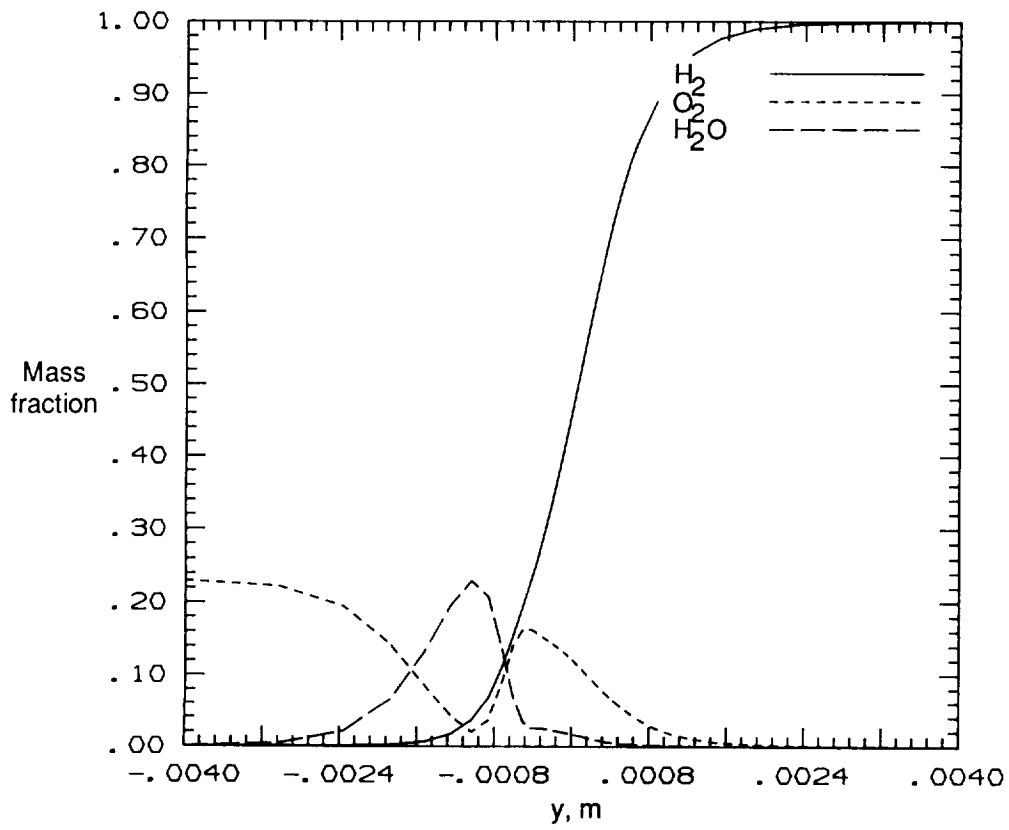Figure 47. Mass fraction versus y at $x = 0$ cm.
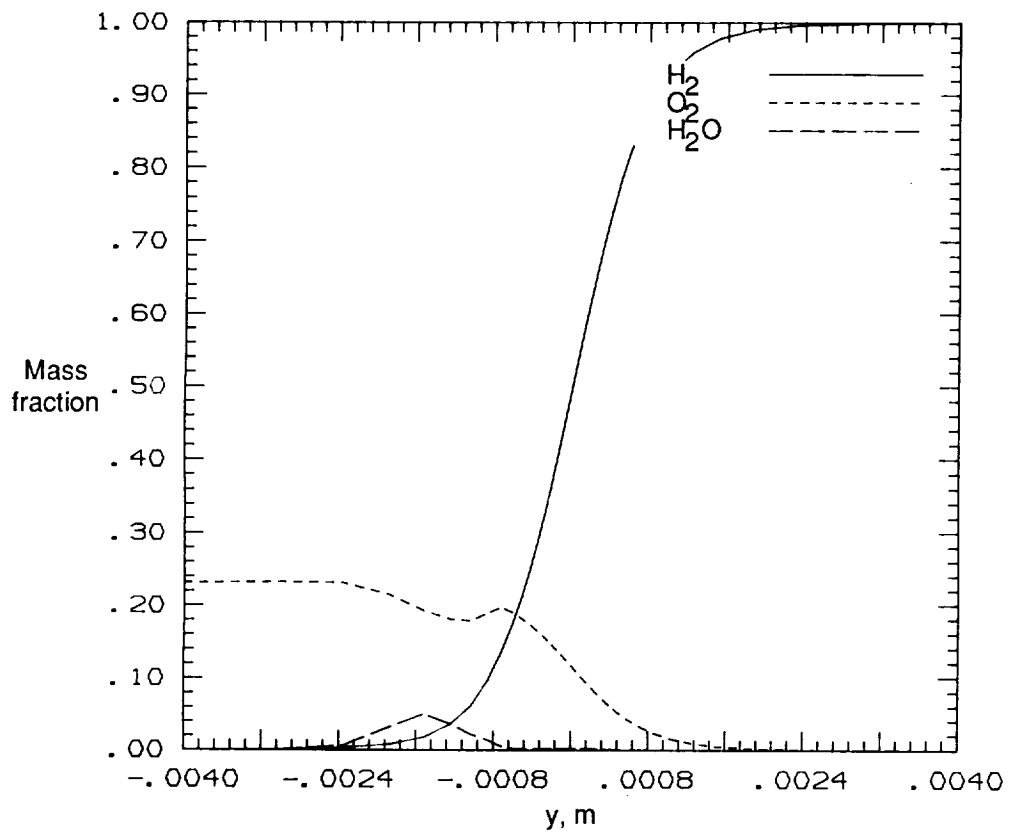
(a) Major species.

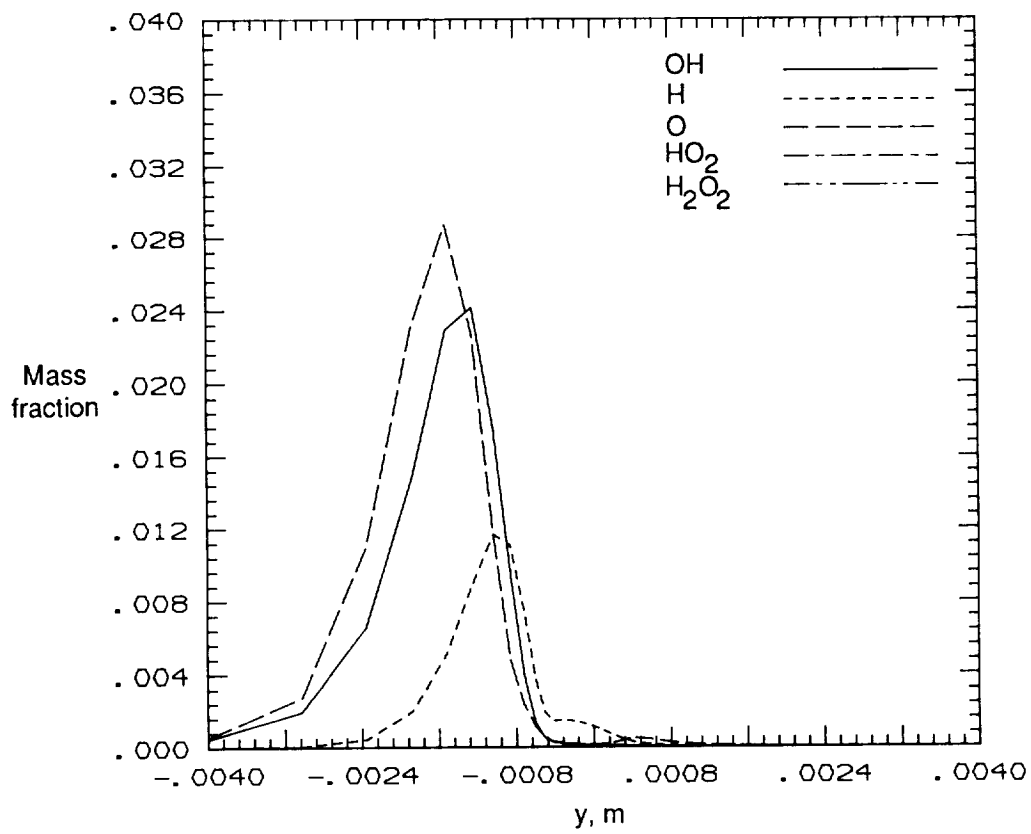Figure 48. Mass fraction versus y at $x = 0.4$ cm.
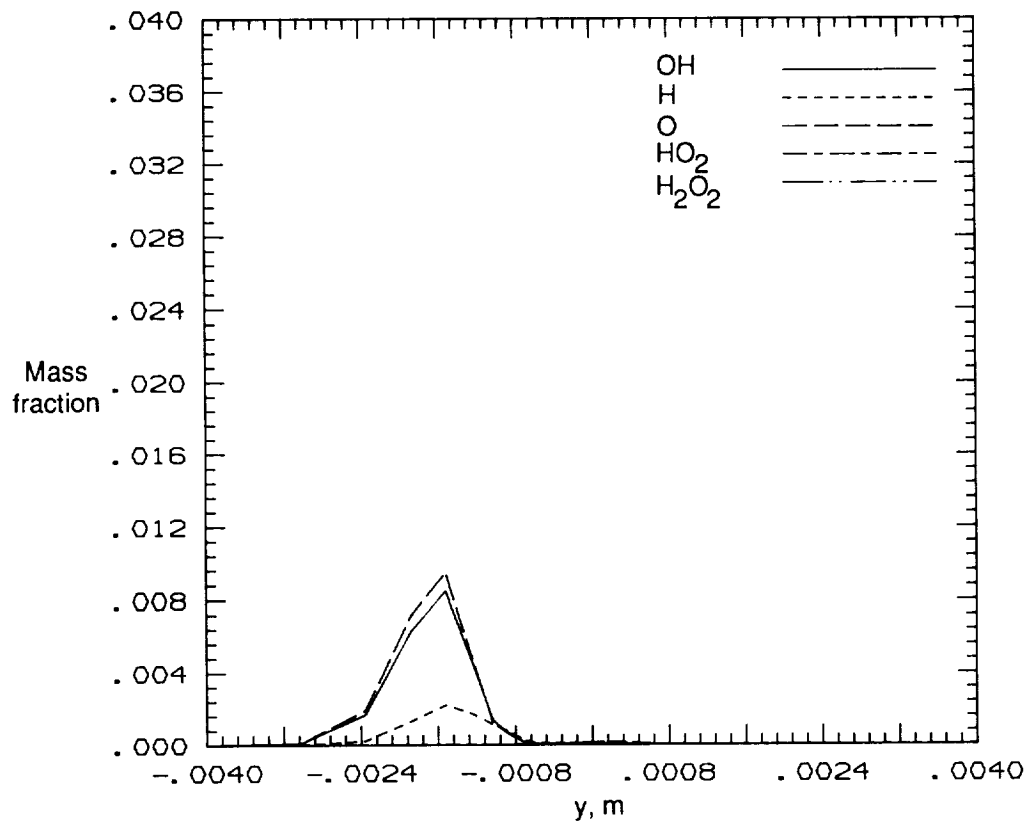
(b) Minor species.
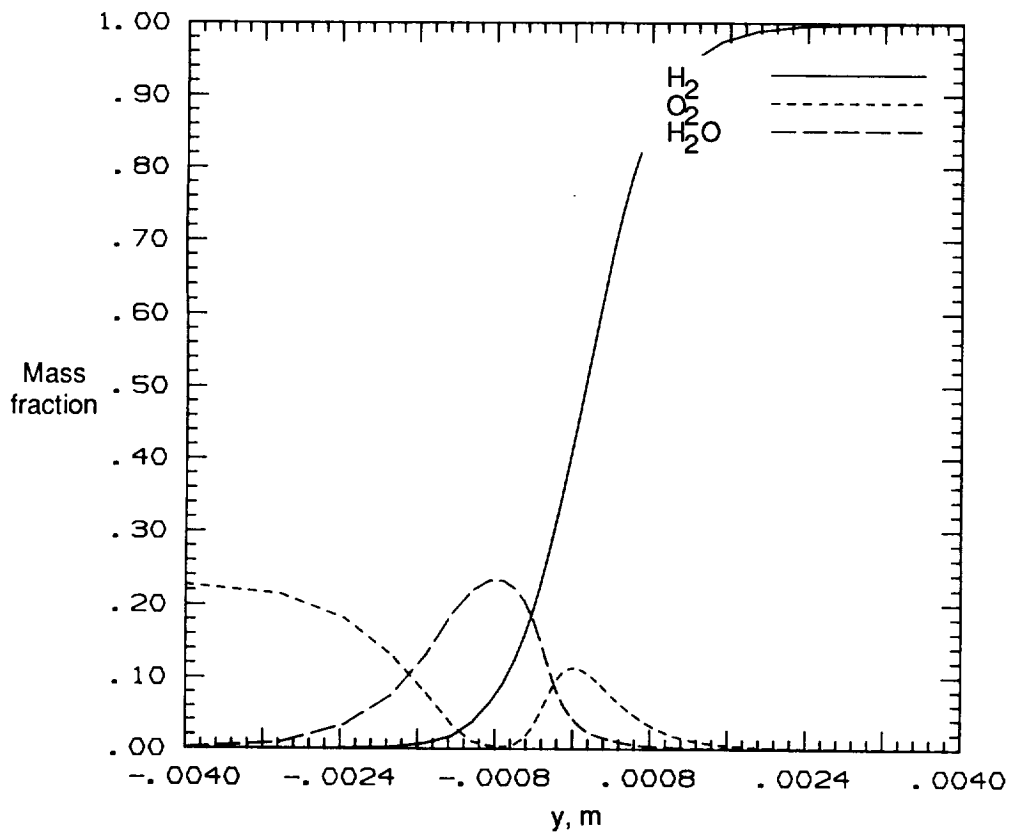
Figure 48. Concluded.
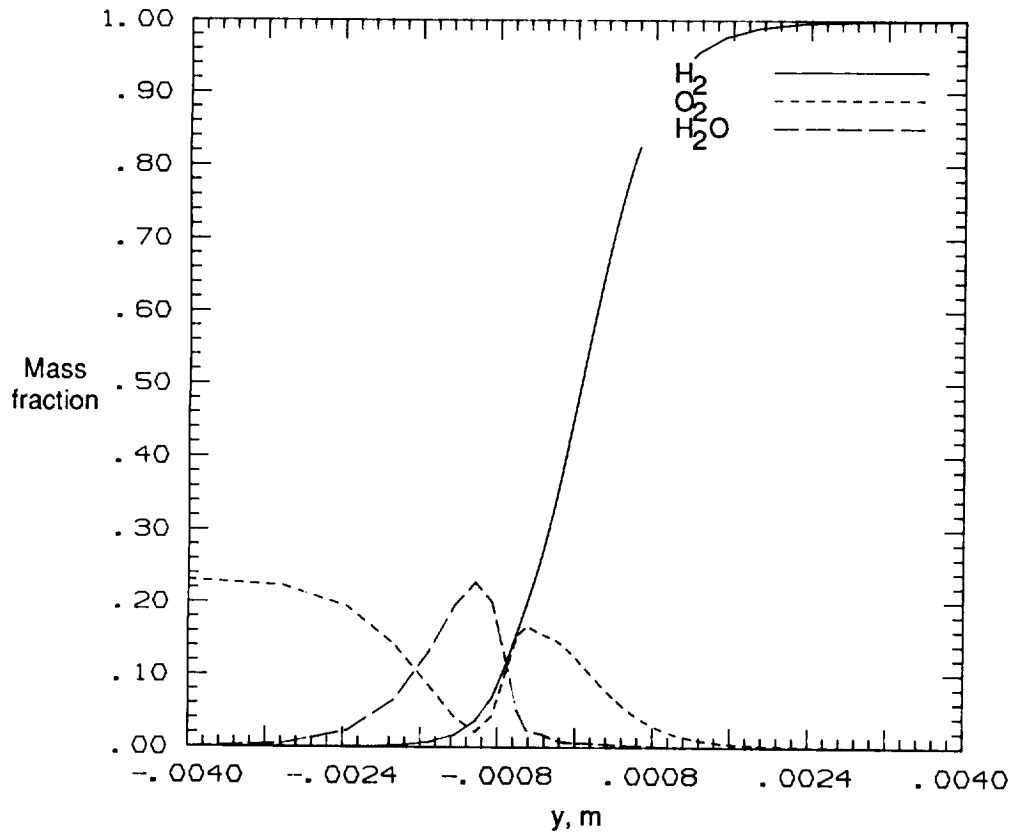
(a) Major species.

Figure 49. Mass fraction versus y at $x = 1.0$ cm.
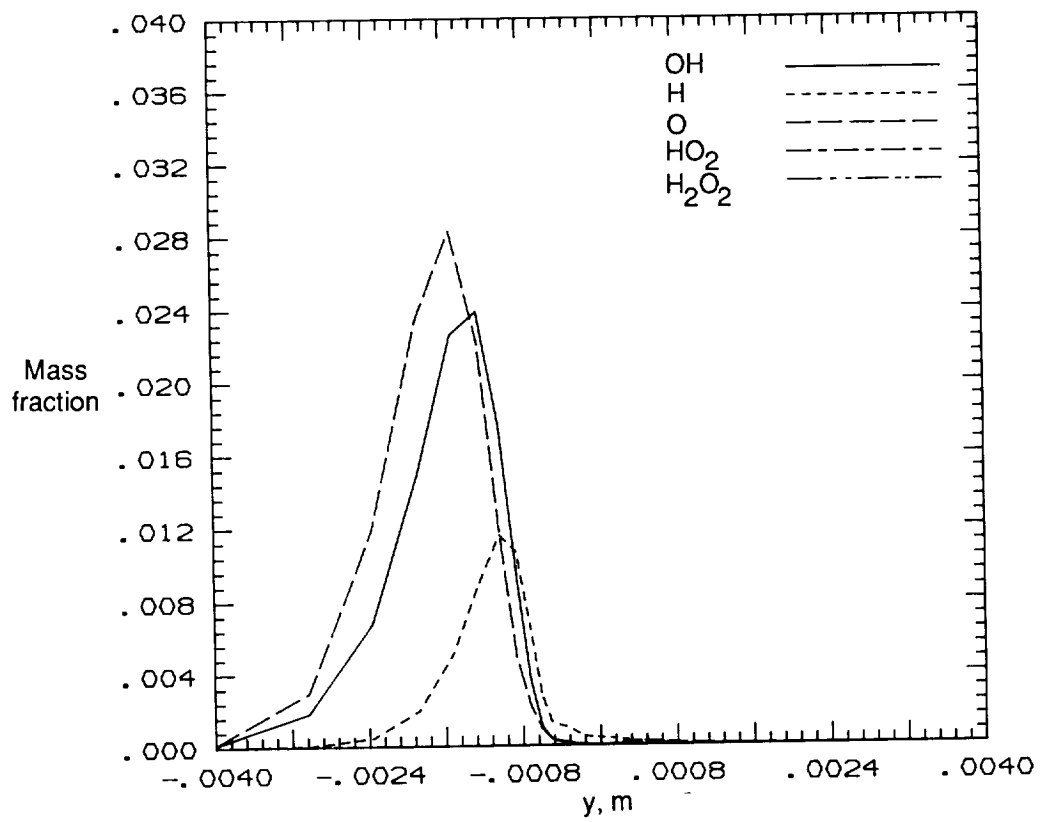
(b) Minor species.

Figure 49. Concluded.
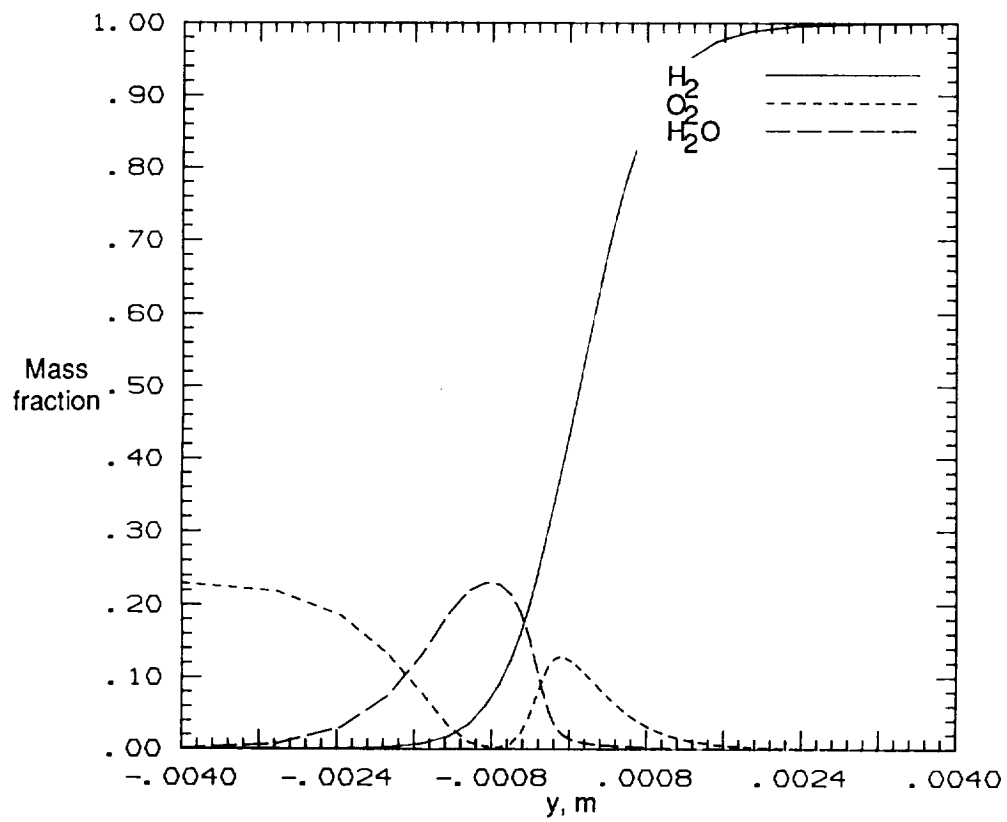
(a) Major species.

Figure 50. Mass fraction versus y at $x = 2.0$ cm.
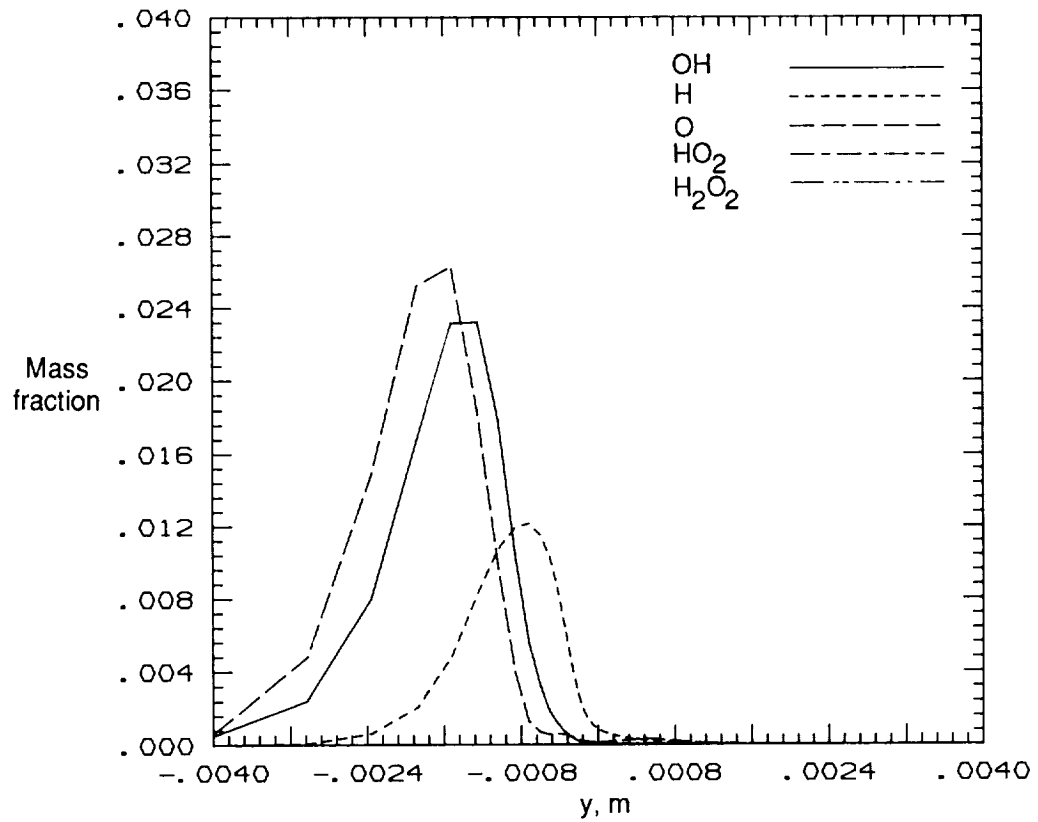
(b) Minor species.

Figure 50. Concluded.
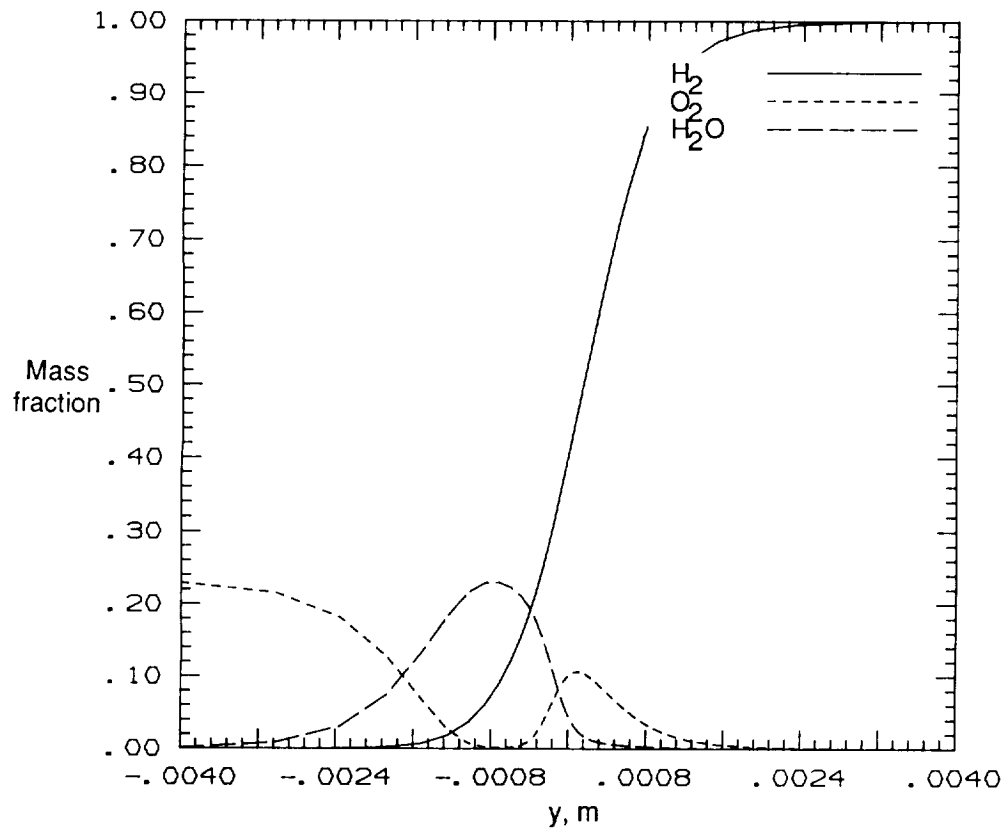
(a) Major species.

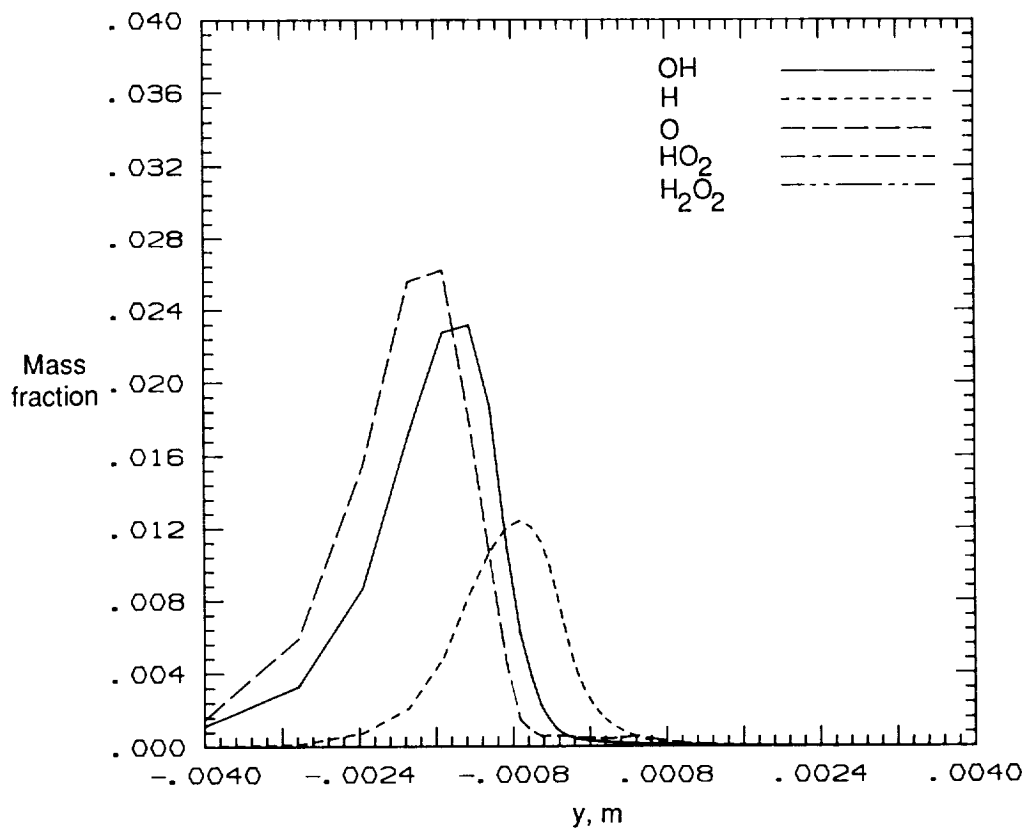Figure 51. Mass fraction versus y at $x = 3.0$ cm.
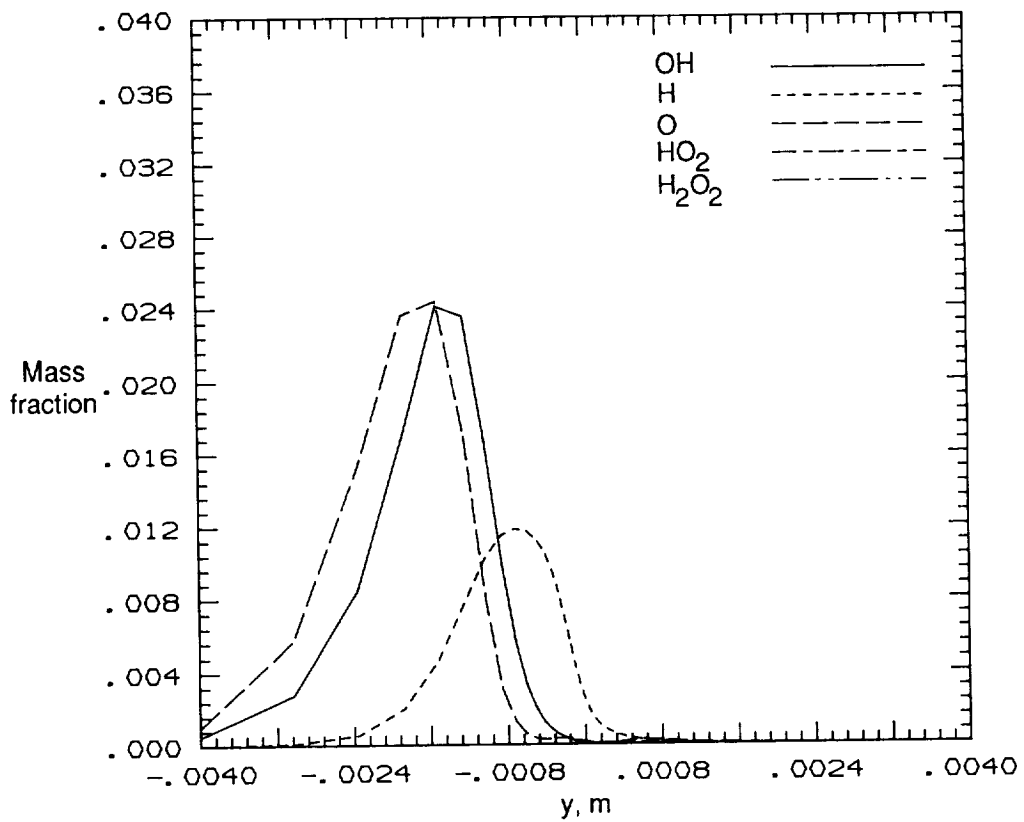
(b) Minor species.

Figure 51. Concluded.
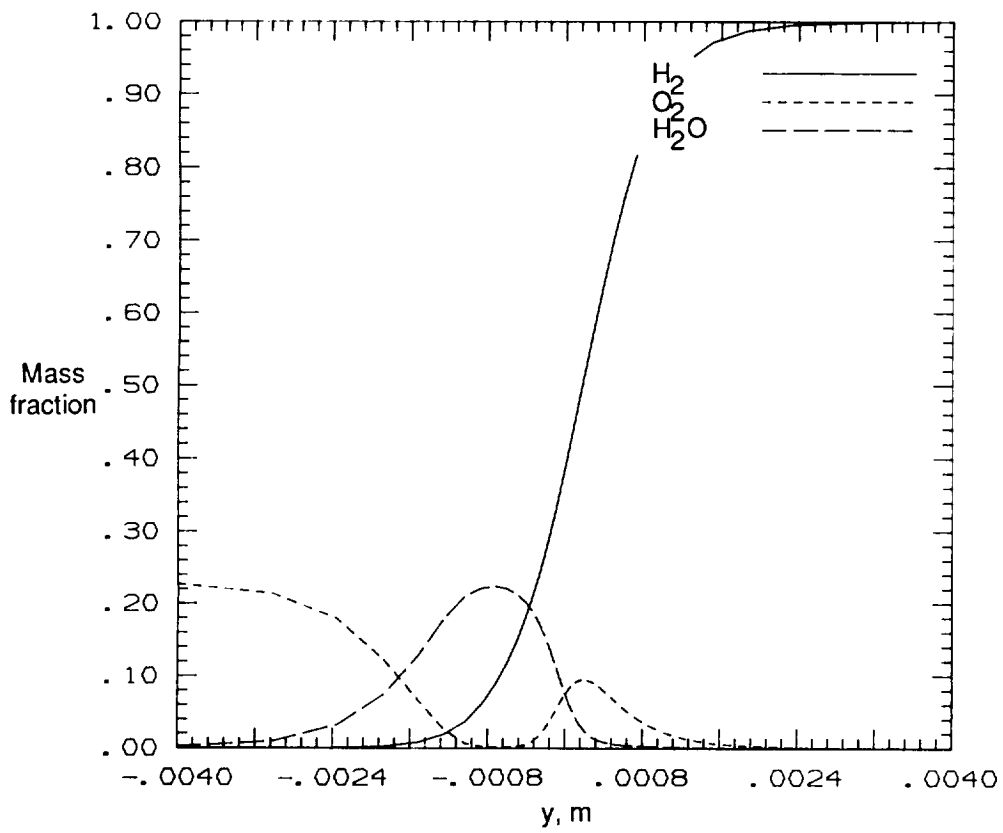
(a) Major species.

Figure 52. Mass fraction versus y at $x = 4.0$ cm.
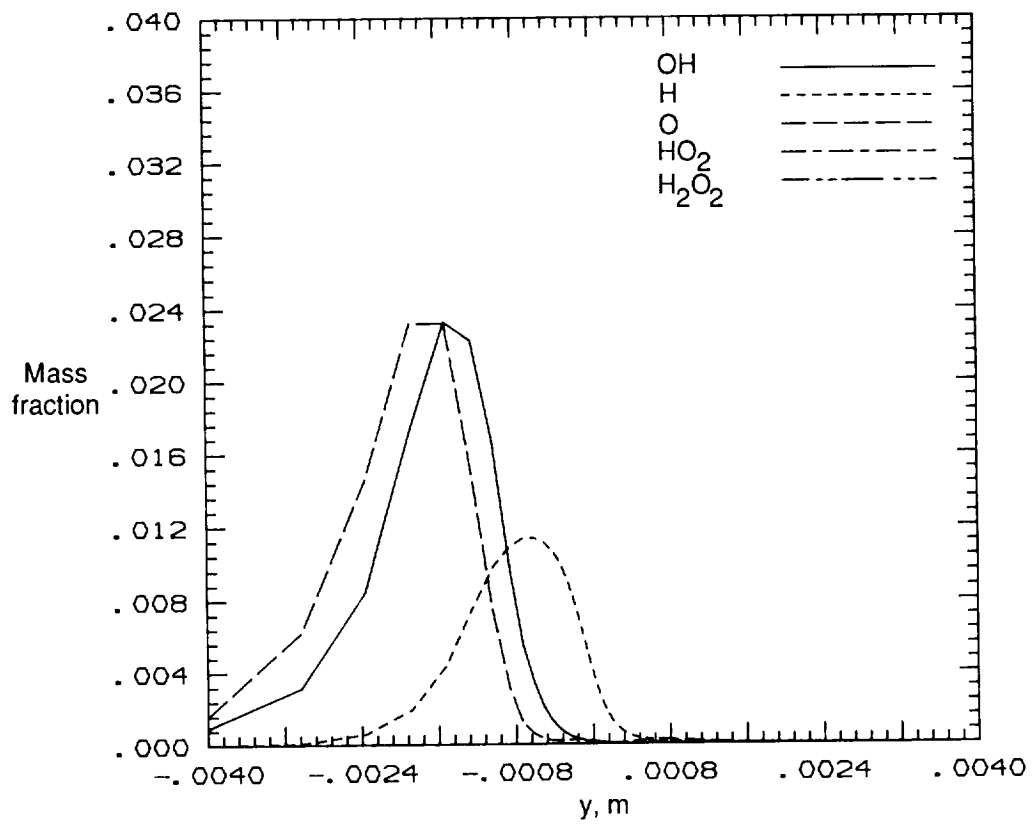
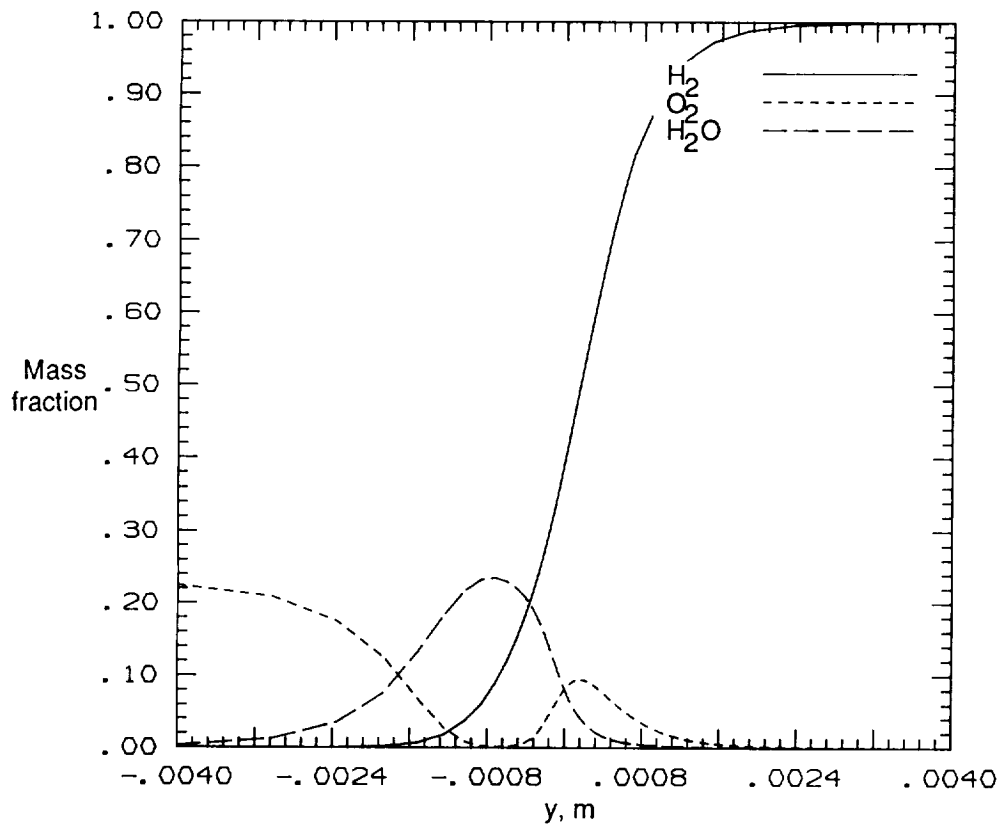(b) Minor species.

Figure 52. Concluded.

80
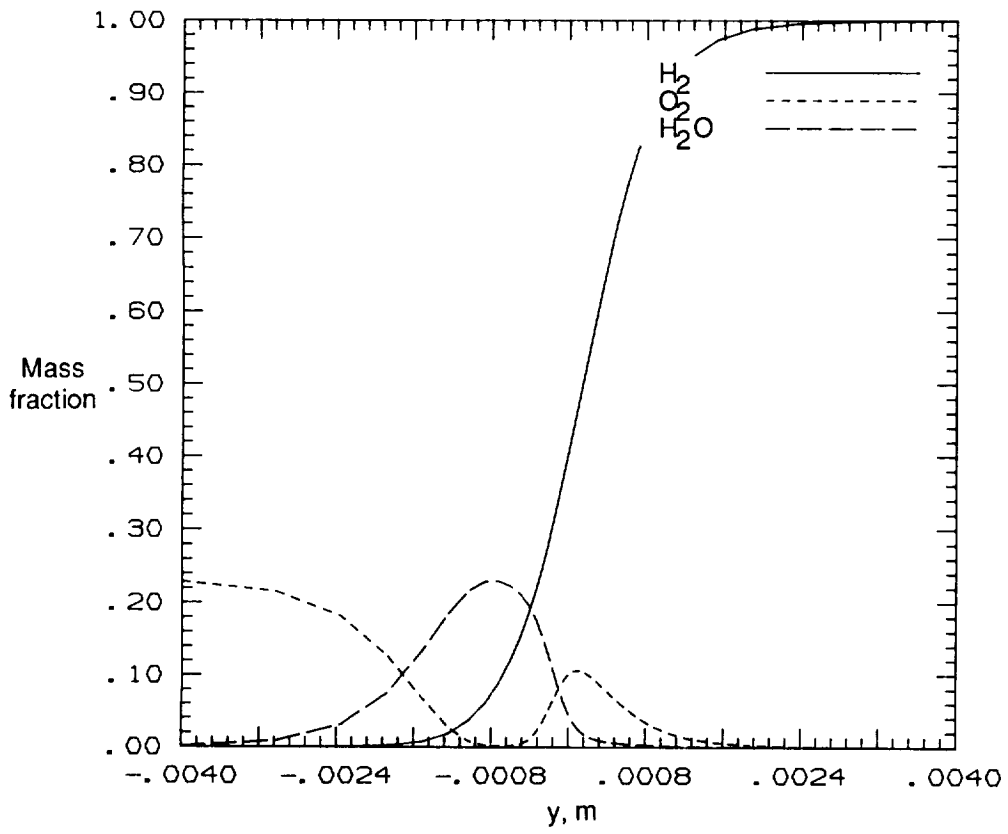
(a) Major species.

Figure 53. Mass fraction versus y at $x = 5.0$ cm.
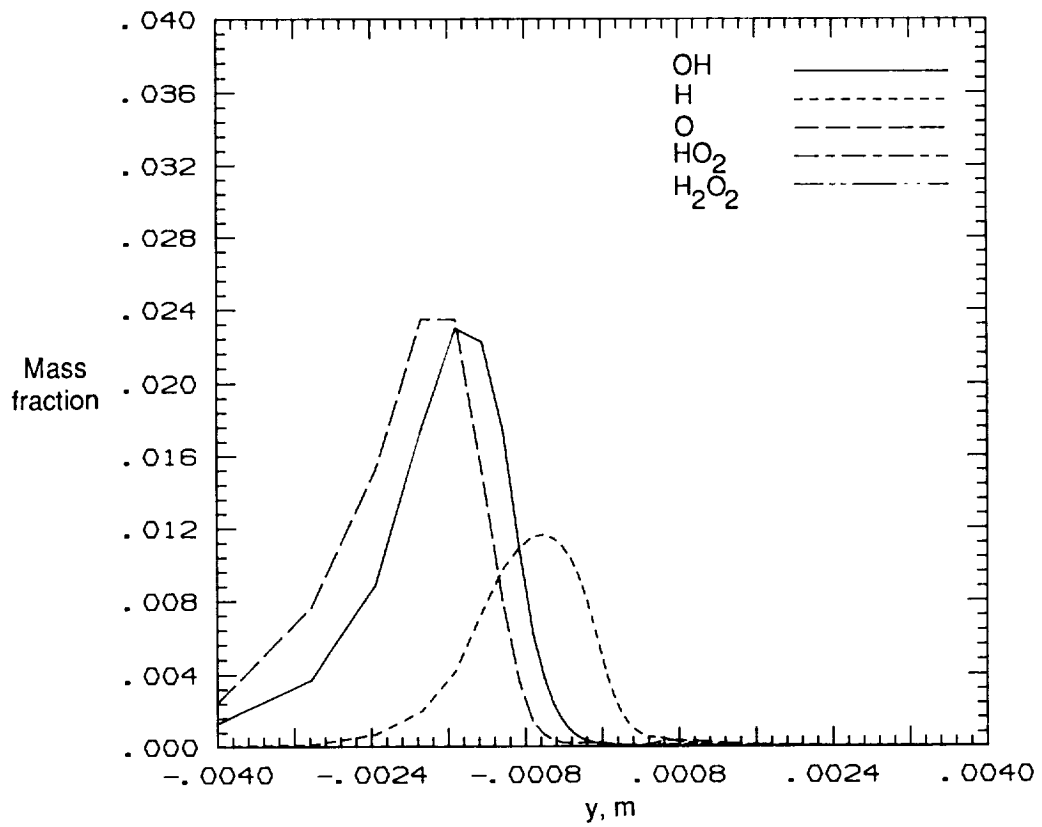
(b) Minor species.

Figure 53. Concluded.

Figure 54. Streamwise velocity versus x at y locations following inflow perturbation.
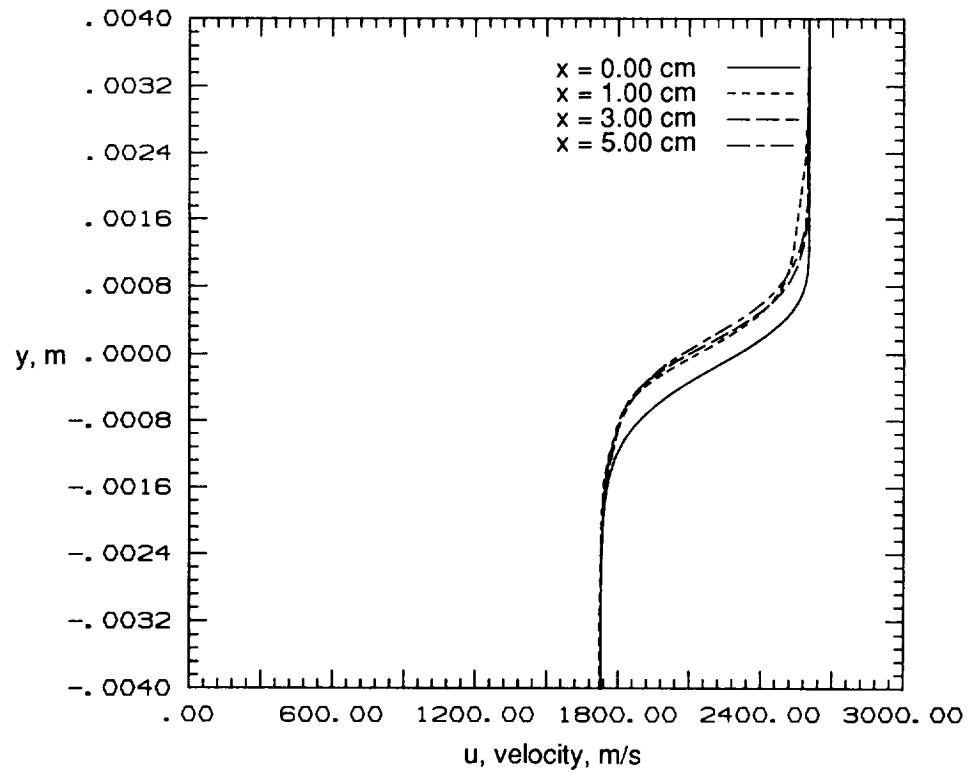
Figure 55. Streamwise velocity versus y at x locations.

83
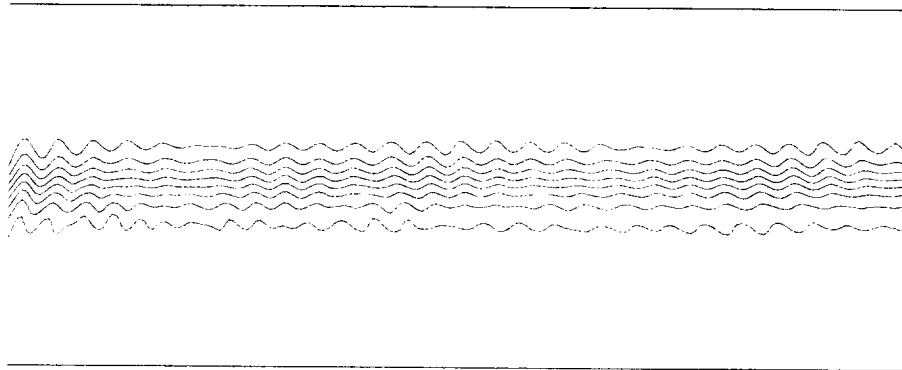
Figure 56. Streamwise velocity contours in mixing layer.
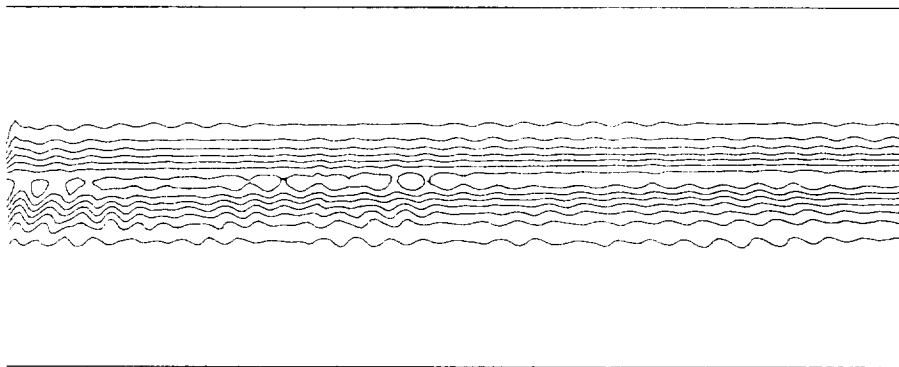
Figure 57. Vorticity contours in mixing layer.

84
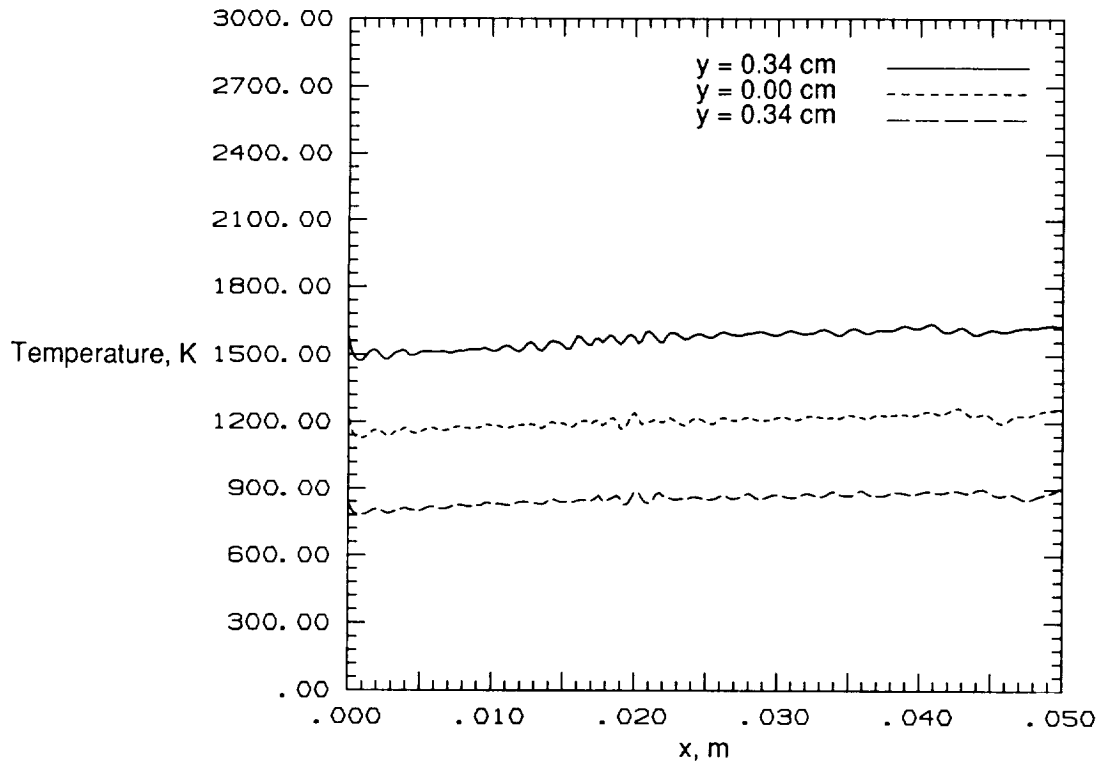
Figure 58. Temperature versus x at y locations.
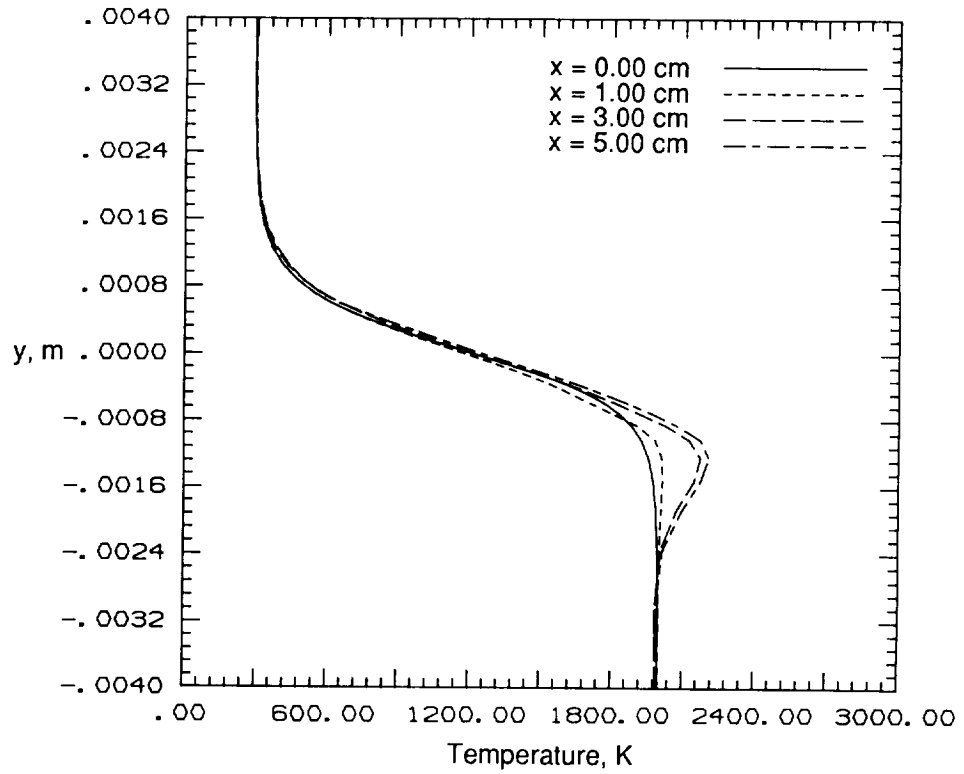
Figure 59. Temperature versus y at x locations.
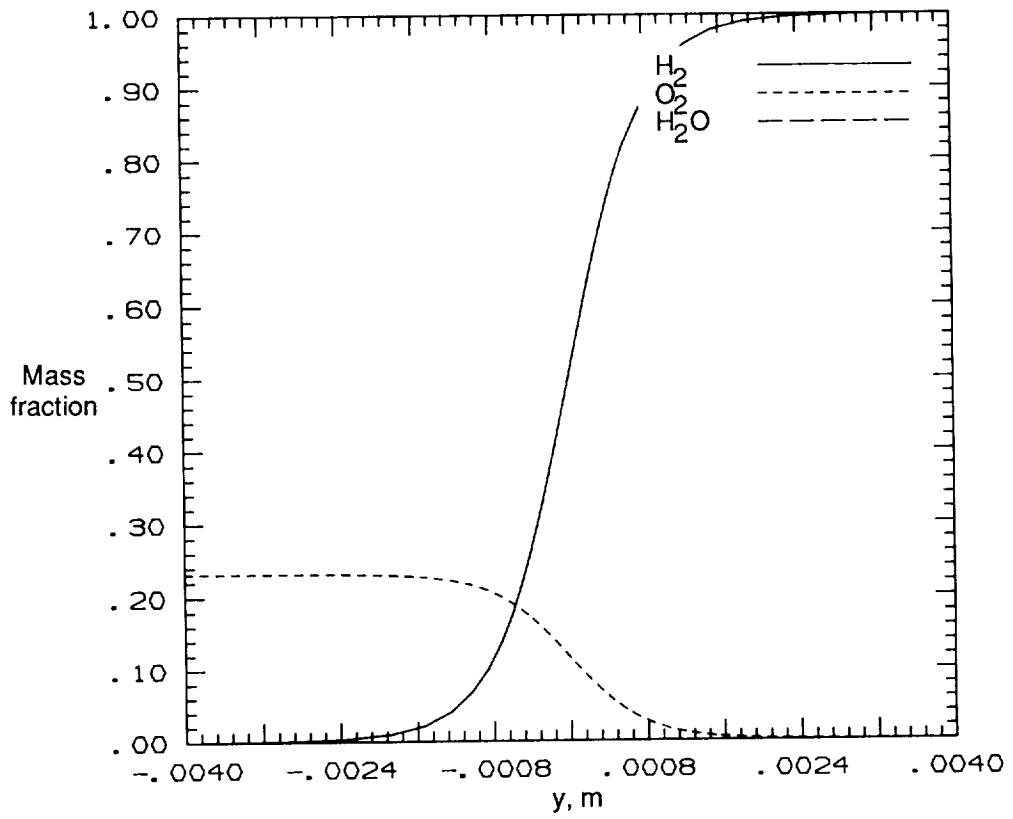
Figure 60. Mass fraction versus y at $x = 0$ cm.
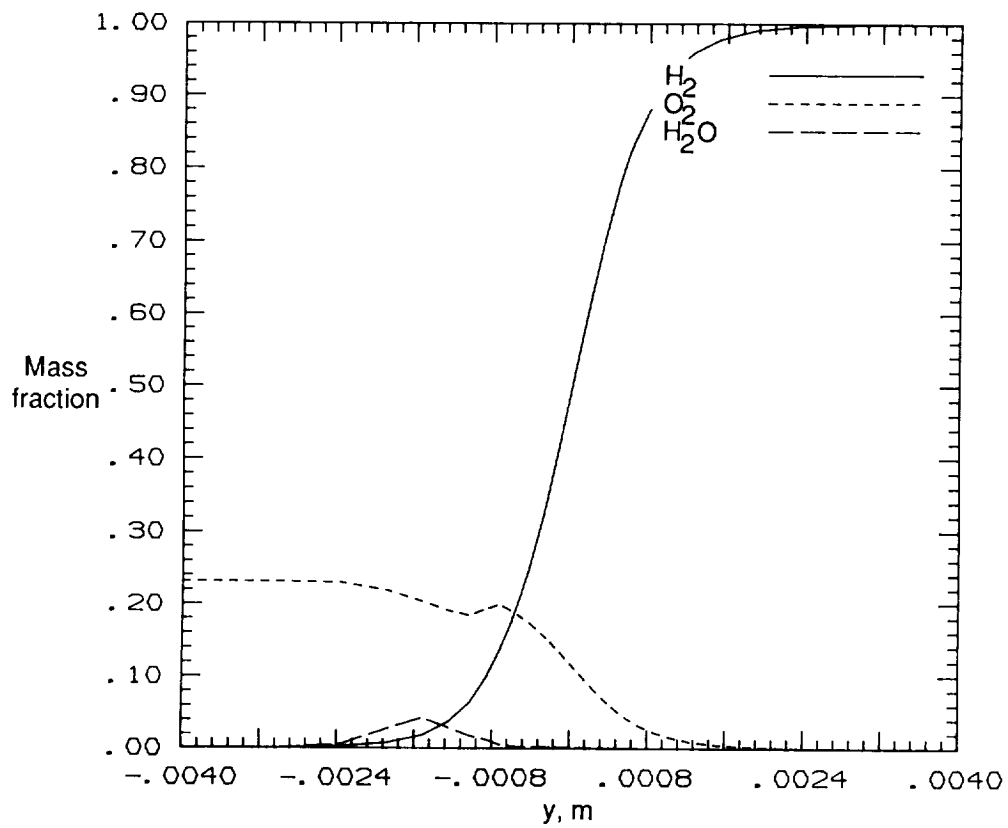
(a) Major species.

Figure 61. Mass fraction versus y at $x = 0.4$ cm.
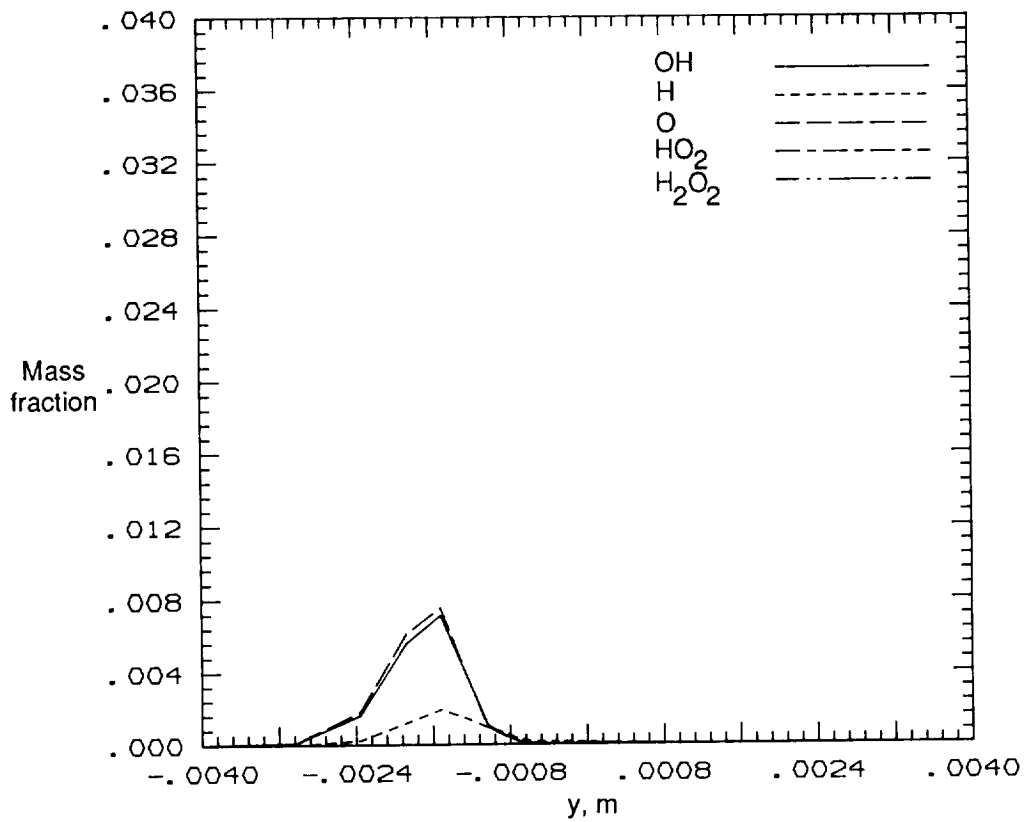
(b) Minor species.

Figure 61. Concluded.

(a) Major species.

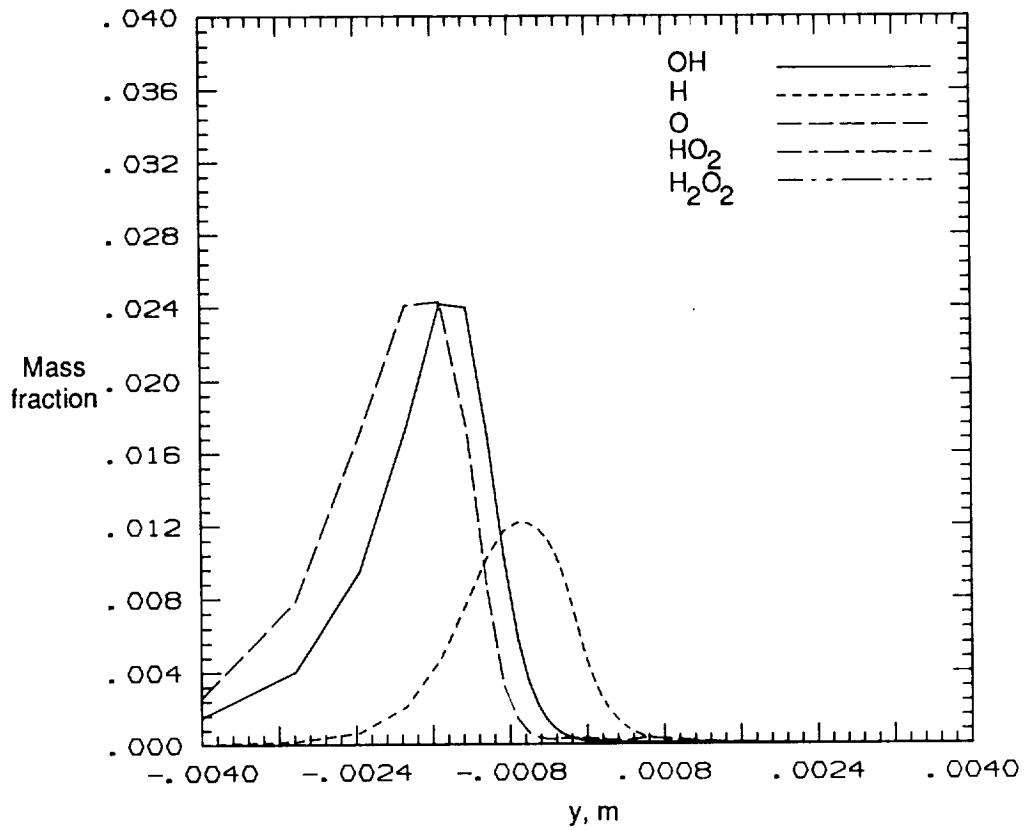Figure 62. Mass fraction versus y at $x = 1.0$ cm.

(b) Minor species.

Figure 62. Concluded.

(a) Major species.

Figure 63. Mass fraction versus y at $x = 2.0$ cm.

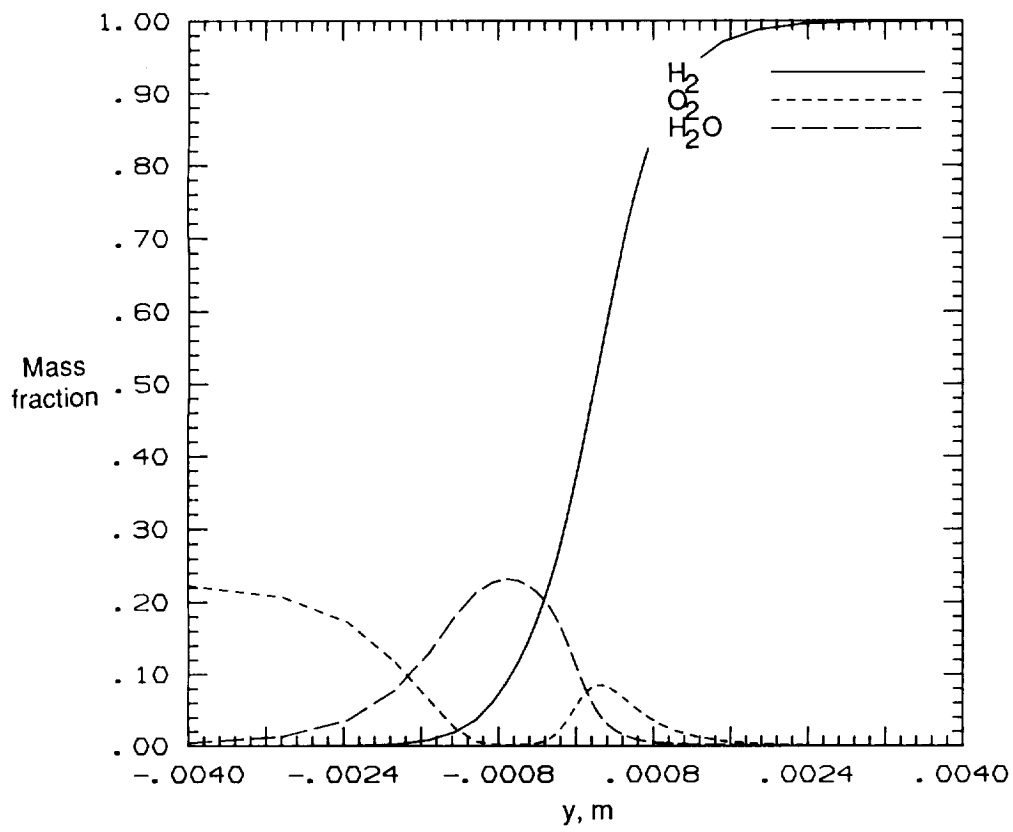(b) Minor species.

Figure 63. Concluded.

(a) Major species.

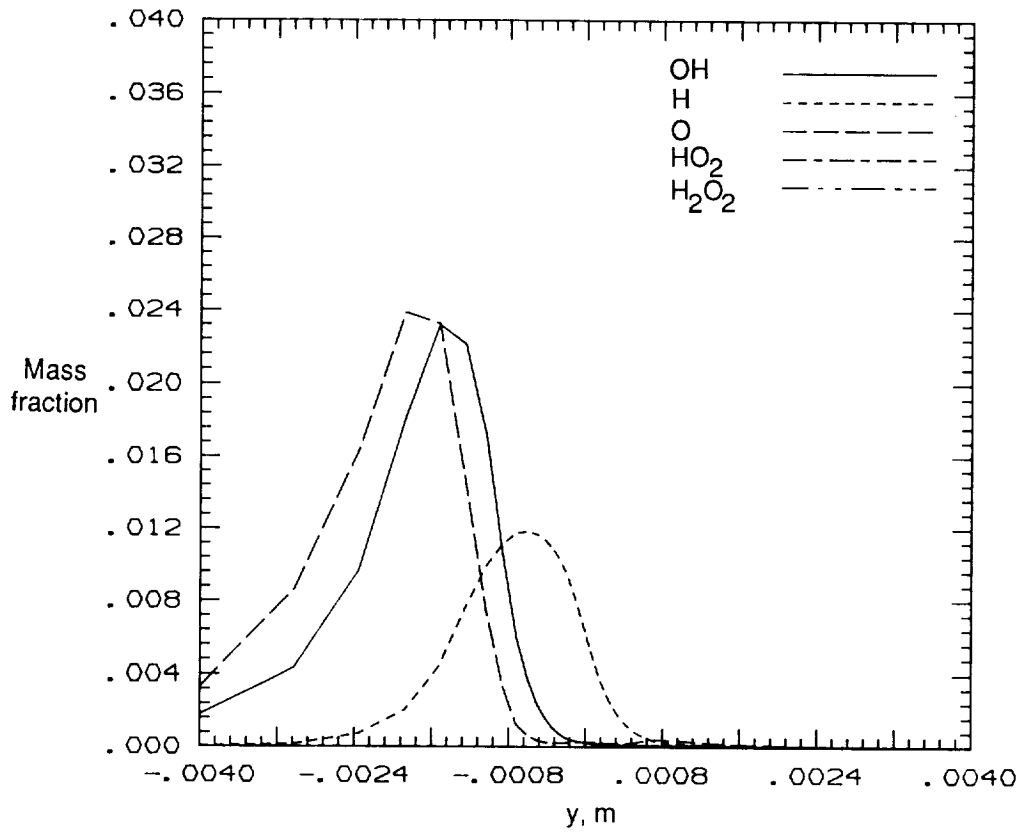Figure 64. Mass fraction versus y at $x = 3.0$ cm.

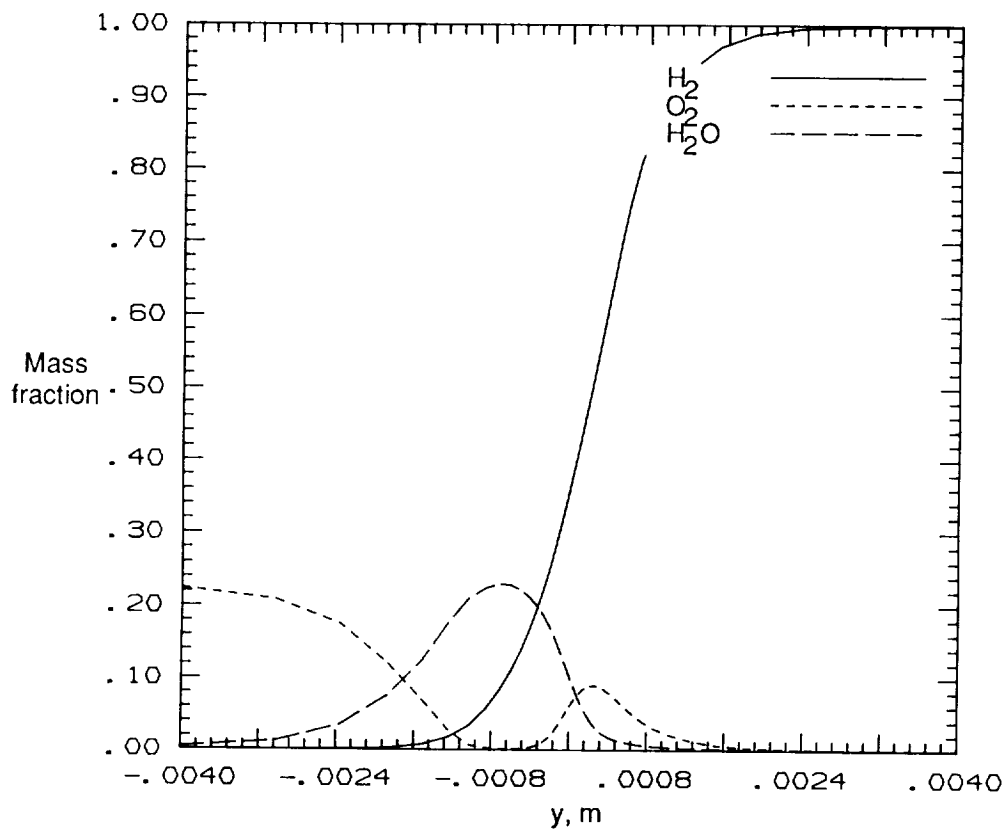(b) Minor species.

Figure 64. Concluded.

(a) Major species.

Figure 65. Mass fraction versus y at $x = 4.0$ cm.

(b) Minor species.

Figure 65. Concluded.

(a) Major species.

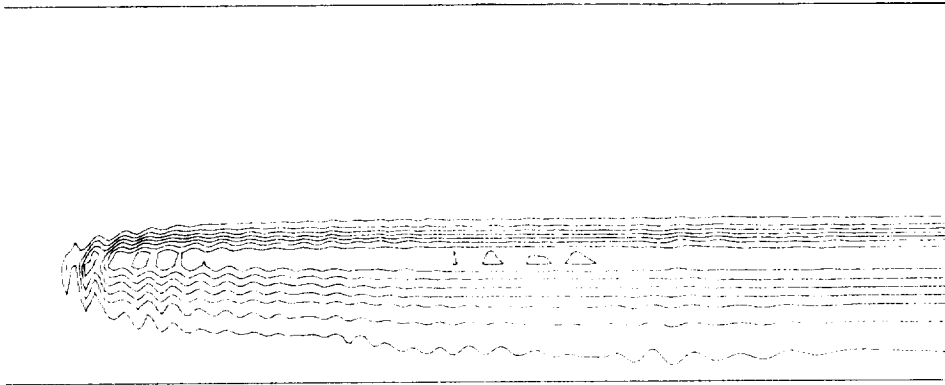Figure 66. Mass fraction versus y at $x = 5.0$ cm.

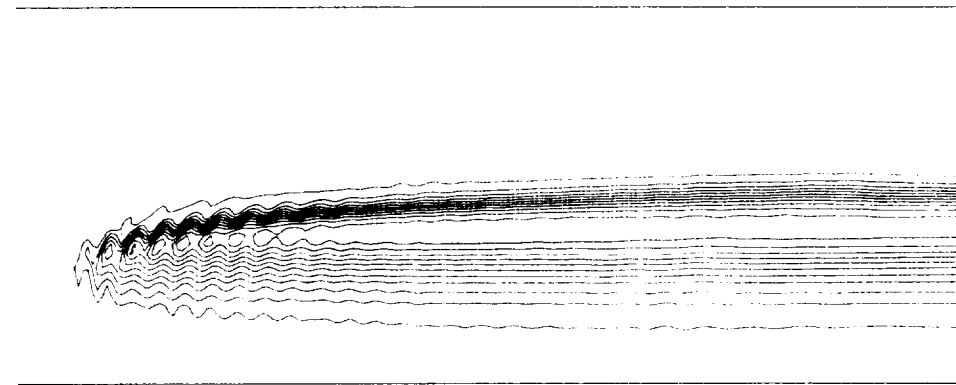Figure 69. Hydroxyl mass fraction contours in mixing layer.

Figure 70. Water mass fraction contours in mixing layer.

Report Documentation Page

1. Report No. NASA TM-4055	2. Government Accession No.	3. Recipient's Catalog No.
4. Title and Subtitle A Two-Dimensional Numerical Simulation of a Supersonic, Chemically Reacting Mixing Layer		5. Report Date December 1988
		6. Performing Organization Code
7. Author(s) J. Philip Drummond		8. Performing Organization Report No. L-16415
9. Performing Organization Name and Address NASA Langley Research Center Hampton, VA 23665-5225		10. Work Unit No. 505-60-01-02
		11. Contract or Grant No.
12. Sponsoring Agency Name and Address National Aeronautics and Space Administration Washington, DC 20546-0001		13. Type of Report and Period Covered Technical Memorandum
		14. Sponsoring Agency Code

15. Supplementary Notes

16. Abstract

Research has been undertaken to achieve an improved understanding of physical phenomena present when a supersonic flow undergoes chemical reaction. A detailed understanding of supersonic reacting flows is necessary to successfully develop advanced propulsion systems now planned for use late in this century and beyond. In order to explore such flows, a study was begun to create appropriate physical models for describing supersonic combustion and to develop accurate and efficient numerical techniques for solving the governing equations that result from these models. From this work, two computer programs were written to study reacting flows. Both programs were constructed to consider the multicomponent diffusion and convection of important chemical species, the finite-rate reaction of these species, and the resulting interaction of the fluid mechanics and the chemistry. The first program employed a finite-difference scheme for integrating the governing equations, whereas the second used a hybrid Chebyshev pseudospectral technique for improved accuracy.

17. Key Words (Suggested by Authors(s)) Fluid mechanics Reacting flows Mixing layers Stability Hypersonic vehicle Scramjet engine Supersonic flow	18. Distribution Statement Unclassified—Unlimited Subject Category 02	
19. Security Classif.(of this report) Unclassified	20. Security Classif.(of this page) Unclassified	21. No. of Pages 105	22. Price A06